Development of a Multi-Point Temperature Fibre Sensor based on a Serial Array of Optical Fibre Interferometers

By Michelin DELLA TAMIN

DISSERTATION

Submitted for partial fulfilment of the requirements for the degree MASTER OF INGENERIAE in

ELECTRICAL AND ELECTRONIC ENGINEERING SCIENCE in the

FACULTY OF ENGINEERING at the

UNIVERSITY OF JOHANNESBURG

STUDY LEADER: Dr Rodolfo Martinez Manuel

November 2014

ABSTRACT

An experimental study of a multi-point optic fibre sensor for monitoring temperature changes is presented. The multi-point optic fibre sensor is made of a serial array of weak-reflectivity identical gratings. The weak-reflectivity identical gratings form the interferometric cavities UV printed on the single mode fibre. The ability to measure temperatures changes at different cavities along the serial array is particularly interesting for the monitoring of power transformers, high temperature furnaces and jet engines.

Changes in temperature in each respective cavity is measured based on the spectral shift in the phase of the light from each respective cavity. The performance of the multi-point fibre sensor system is evaluated. Further, a theoretical and experimental investigation of a serial array composed of two cavities of different lengths is conducted. This investigation is aimed at measuring the impact of the overlap of the two distinct cavities in their respective frequency domain and determining the accuracy of the measurement. The result found shows that the sensor phase response is no more linear to temperature changes. It is also found that the nonlinear response of the sensor to temperature changes increases with the magnitude of the overlap.

The multiplexing capability of the sensor system is practically enhanced by the use of a combination of frequency division multiplexing (FDM) and a wavelength division multiplexing (WDM) implemented on a SMF-28. This multi-point sensor system is appropriate for applications where monitoring of distinct structures has to be implemented for the detection of temperature changes. In this sense, 9 local sensors formed by Fabry-Perot interferometers are designed and printed on a serial array and then experimentally tested for temperature changes. A temperature sensitivity of 10 $\frac{pm}{°C}$ and a resolution of 0.125°C are evaluated.

Keywords: quasi-distributed, SMF-28, resolution and sensitivity.

DEDICATION

To my wife, Leigh Anne Colombick, who has practiced tremendous patience and provided incredible encouragement and support for my Masters study; and my children, Michael Lawrence Della Ngatchou and Daniel Gaetan Della Ngoumafo, who have given me so much happiness in my daily life.

ACKNOWLEDGEMENTS

The last few years of being a Masters student in the Photonic Research Group at the University of Johannesburg have been full of challenges in my academic and family life. Irrespective of all the challenges, I would like to express my sincere gratitude to my study leader, Dr Rodolfo Martinez Manuel, for his endless advice, guidance, support, supervision, and encouragement throughout my Masters study at University of Johannesburg.

I would like to thank Prof Johan Meyer for providing financial support, for being like a father to me and for grooming me as a researcher. In this same regard a special thanks to all the lecturers of the department of Electrical and Electronic Engineering Sciences especially to Prof Bheki Twala, Prof Jan Harm C. Pretorius and to all the friends in the Photonic Research Group.

Finally, I would like to thank my family members and especially to Nza Andre Ngatchou, Nzam Jeannette Ngassam epouse Tchagna, Nza Emilie Wankeu and Yveline Mbianda for everything they have done in my life.

DECLARATION

I hereby declare that this dissertation for the Master of Ingeneriae in Electrical and Electronic Engineering Science degree is my own work and has not previously been submitted to another university or institution of higher education for a degree.

MICHELIN DELLA TAMIN

LIST OF ACRONYMS

EFPI	Extrinsic Fabry-Perot Interferometer
EMI	Electro Magnetic Interference
FP	Fabry-Perot
FPI	Fabry-Perot Interferometer
FDM	Frequency Division Multiplexing
FBG	Fibre Bragg Grating
GIF	Grade Index Fibres
HBF	High Birefringent Fibres
HOF	Hollow Optic Fibre
HF	Hydro-Fluorine
IFPI	Intrinsic Fabry-Perot Interferometer
LED	Light Emitting Diode
LPG	Long Period Grating
MI	Michelson Interferometer
MZI	Mach-Zehnder Interferometer
OFS	Optical Fibre Sensor
OSA	Optical Spectrum Analyzer
OTDR	Optical Time Domain Reflectometry
PCF	Photonic Crystal Fibre
PMF	Polarization Maintaining Fibre
RI	Refractive Index

RMSD	Root Mean Square deviation
SMF	Single Mode Fibre
SNR	Signal to Noise Ratio
TDM	Time Division Multiplexing
UV	Ultra Violet
WDM	Wavelength Division Multiplexing

Contents

Table of figures

1. Introduction

1.1. Motivation

Temperature measurements are of great importance to smart structures, system control and manufacturing process monitoring. Accurate monitoring of temperature supports maintenance programs, allowing identification of problems at an early stage, thus ensuring that proper actions can be implemented to assure safe and efficient operation. This enables maintenance cost reduction, thereby increasing the operative life of the structures. Temperature sensors have been used in a wide range of industrial applications including aircraft jet engines, nuclear plant boilers and tunnels, et cetera. Most of these sensor are electronic based.

Over the past few decades, optic fibre sensors (OFSs) have attracted considerable attention for temperature, stress monitoring, et cetera. (K. T. V. Grattan and B. T. Meggitt, 1995). Compared to traditional electronic sensors, OFSs offer numerous intrinsic advantages which include:

- Immunity to electromagnetic interference (EMI);
- Higher sensitivity, higher accuracy and dynamic range;
- Small size, light weight;
- Ability of remote operation;
- Survivability in harsh environment where electronic sensors cannot work; and
- Potential capability of multiplexing many sensors along single optical fibre cable.

In many applications, temperature needs to be monitored at multiple locations simultaneously. Using electronic sensors in such circumstances makes the multiplexing system overly complex to install and to maintain. By using a multiplexed system, many OFSs can be implemented on the single length of the optic fibre cable. By sharing the same interrogation system for all the multiplexed sensors, the cost per sensing point is significantly reduced. The need for multiple-point temperature monitoring is increasingly in demand (W. Ha *et al.*, 2008). The motivation of this project is to address these increasing demand for a multi-point temperature sensor with a high spatial resolution, easy to fabricate, robust and a large number of sensors, which could be operated reliably in harsh environment to monitor high power transformers, high temperature furnaces, et cetera.

1.2. Background

OFS systems are based on the interaction of the physical parameters with the transducer, which changes the intensity, phase, wavelength or polarisation of the light propagating at the transducer. Basically, OFSs consist of four major components: optical source, signal waveguide (e.g., optical fibre), transducer, and detection system. The incident light wave propagates along an optical fibre passing through the transducer, where certain properties of the light wave are modulated when the transducer is influenced by the physical parameters which need to be monitored. The modulated light wave that contains the information is then captured by the detector system. The response to the external perturbations is enhanced so that the resulting changes in the characteristics of light is used to measure the magnitude of the perturbation (B. Gholamzadeh, and H. Nabovati, 2008). A basic configuration of an OFS is presented in Figure 1-1.

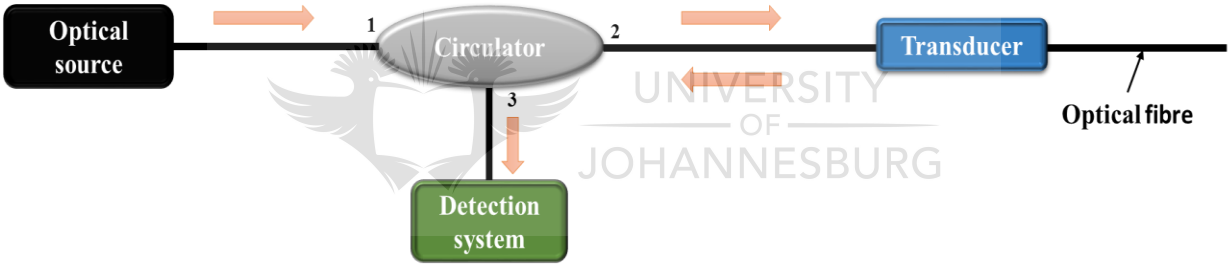

Figure 1-1. Layout of a Simple OFS System composed of an optical source, a transducer and the detection system.

1.2.1. Optical fibre sensor classification

Historically a number of different approaches have been used to classify optical fibre sensors. Several schemes of classifying optical fibre sensors have been established with respect to:

- The sensor location (extrinsic and intrinsic),
- The modulation principles (wavelength, frequency, amplitude and polarization) and
- The spatial distribution (point, distributed and quasi-distributed).

For some sensor applications, the optic fibre is only used to guide light to the sensing point, whereby the optical signal merges into an optical device within which modulations take place. This optical signal modulated by the physical parameter is collected by the same or different

fibres and then returned to a remote location for detection and signal processing. This sensor is known as an extrinsic fibre sensor.

For some other applications, the sensors are imprinted on the fibre and the modulations induced by the physical parameters thus occur within the optical fibre. This class is known as an intrinsic OFS. In this case, the optical fibre functions as both a transmission medium and sensing element. Such OFS systems have been reported for temperature monitoring (B. H. Lee *et al*., 2012; W. H Tsai and C. J. Lin, 2001; P. D. Allen and N. J. Hargrave, 1992). B. H. Lee *et al*., have reported a review on extrinsic and intrinsic interferometric fibre sensors for temperature, refractive index measurements. W. H. Tsai presented a Fabry-Perot sensor utilizing a cavity formed between two cleaved ends of two optical fibres fixed in a capillary for temperature monitoring while P. D. Allen presented an interferometric fibre sensor for temperature monitoring in absorbed dose calorimetry using phase modulation.

With respect to the spatial distributions, optical fibre sensors comprise a point, distributed and quasi-distributed fibre sensors (K. Fidanboylu, and H. S. Efendioglu, 2009).

A point sensor is an optical device that monitors the physical parameters at one specific location at a time. Many optical fibre components could serve as point sensing heads, such as fibre Bragg gratings (FBGs) (A. D. Kersey *et al.*, 1997), optical fibre Fabry-Perot interferometers (C. E. Lee *et al.*, 1989), multimode fibre interferometers (B. Dong *et al.*, 2009), et cetera.

For the health monitoring of some massive structures, the locations that need to be monitored are usually not known. The point fibre sensor is not applicable and the distributed fibre sensor (DFS) is preferred. DFSs are intrinsic fibre sensors. The low-attenuation inside the optical fibre has favoured their development. In this regard, the monitoring of physical parameters over extremely long distances of up to 40 kilometres has been reported (A. Signorini *et al*., 2010), which represents a remarkable number of point sensors in a configuration having a spatial distribution of 50 cm or less. This makes distributed sensors a very attractive solution when the continuous monitoring of a large number of locations is required.

When the physical parameters to be monitored are at different fixed locations along the optical fibre, the distributed fibre sensor is also no longer suitable in such a situation, making the quasi-distributed sensor more appropriate. The quasi-distributed fibre sensor is made of point sensors that are spaced along the optical fibre at designed positions. They are able to measure the physical parameters of many separate points in the space simultaneously, by multiplexing the point sensors to form a sensing mesh. In this configuration, a common interrogation system is

used to monitor the physical parameter at each respective point sensor. Different quasi-distributed sensor applications with FBG arrays have already been reported, using Fabry-Perot filters (M. A. Davis *et al.*, 1995; A. D. Kersey, *et al.*, 1995), acousto-optic filters (M. G. Xu *et al.*, 1993), FBG-based filters (M. A. Davis and A. D. Kersey, 1995), et cetera. The optical setup with respect to spatial distribution is presented in Figure 1-2.

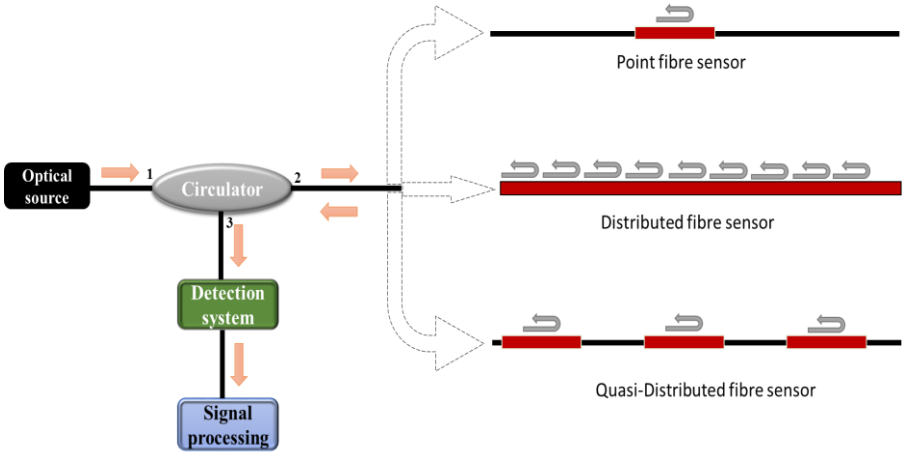

Figure 1-2. OFS Spatial Distribution Layout.

The spatial distribution that we are interested in this project is the quasi-distributed configuration, made of interferometric point sensors. Interferometric fibre sensors are based on interferometers, designed and implemented inside optical fibres and classified as:

- Michelson,
- Mach Zehnder,
- Sagnac and
- Fabry-Perot (F-P).

A Michelson fibre interferometer is composed of the reference arm and the sensing arm, whereby each is attached to a reflective mirror operating in reflection mode. The optical setup of the Michelson interferometer is presented in Figure 1-3.

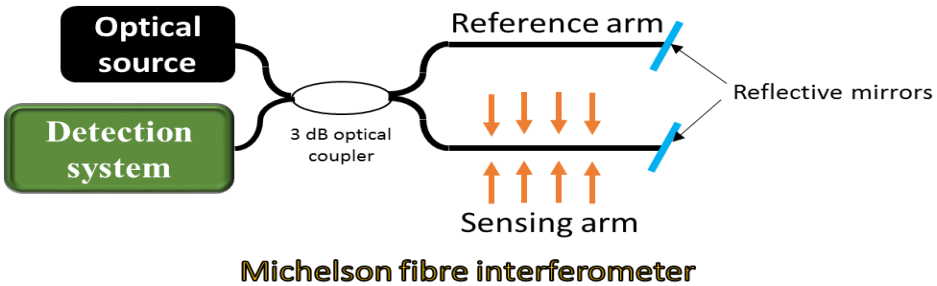

Figure 1-3. Michelson fibre interferometer optical setup.

The Mach-Zehnder fibre interferometer is an extended version of the Michelson interferometer, also having a reference and a sensing arm. In this configuration, the detection system operates in transmission mode. The Mach-Zehnder optical setup is presented in Figure 1-4.

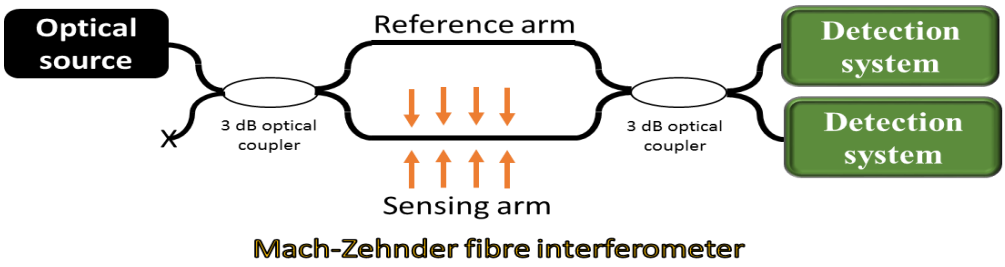

Figure 1-4. The Mach-Zehnder fibre interferometer optical setup.

The Sagnac fibre interferometer is a ring interferometer, based on counter-propagating beams in an optical ring as presented in Figure 1-5.

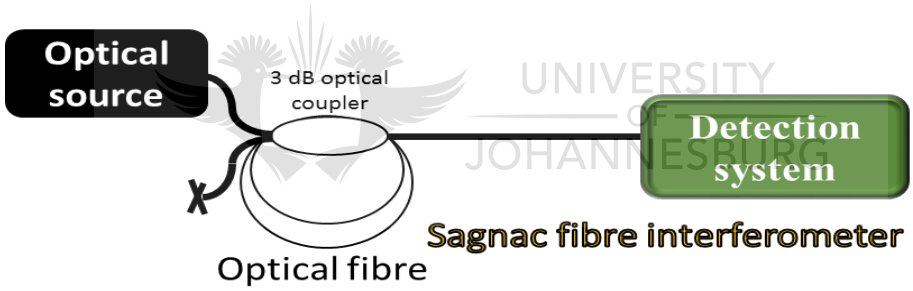

Figure 1-5. The Sagnac fibre interferometer optical setup.

Generally, Michelson, Mach-Zehnder and Sagnac are known as two beam interferometers. When light is introduced to the fibre interferometers, it is split at the 3 dB coupler and propagates down the two arms. The sensing arm is exposed to external perturbations while the reference arm is not. As the split incident light is reflected or transmitted, it recombines at the 3 dB coupler. As a result of the recombination of the light from the two arms, an interference is formed. Since the interfering spectra are usually directly related to the length of the optical path, these sensors have high sensitivity to many external perturbations, such as temperature.

The interferometric configuration we are interested in this project is the Fabry-Perot (F-P) interferometer to form the point sensors along the quasi-distributed system. F-P interferometric sensor, is made of two reflective mirrors separated by a cavity. This is known as a multiple

beam interferometer. When the mirrors are of low-reflectivity, only the first two emerging light beams have a significant intensity. In this case, the F-P fibre sensor is approximated to a two beam interference. Compared to other interferometric fibre sensors, the F-P interferometric sensor shows a great potential for quasi-distributed temperature measurement in smart structure monitoring due to its simple structure, small size, high stability and ease of being embedded into structure materials. The optical setup of the F-P interferometer is presented in Figure 1-6.

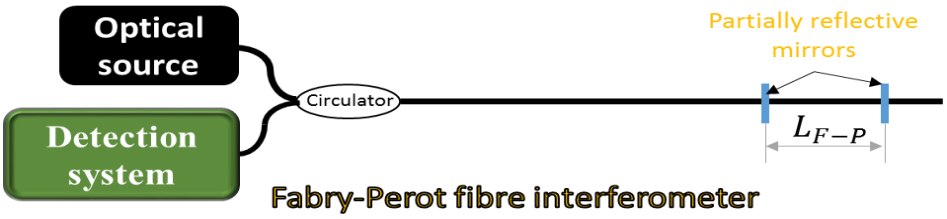

Figure 1-6. F-P fibre interferometer optical setup.

F-P interferometric sensors for temperature and strain measurements have been implemented using fibre Bragg gratings (FBGs) as reflective mirrors (M. G. Shlyagin *et al.*, 2001; S. C. Kaddu *et al.*, 1997).

FBG is a Bragg reflector which reflects particular wavelengths of light and transmits all others when illuminated by a broadband source. The advantage of using FBG as reflectors in a F-P fibre sensor configuration is that they can be tuned to a designed wavelength and designed reflectivity. Furthermore in a quasi-distributed system, they are easily implemented in an array of point sensors whereby each point sensor is made of two FBGs separated by a cavity.

In order to monitor the physical parameters in interferometric sensor configurations, appropriate demodulation algorithms are applied to the interference that is detected. This is aimed at measuring the magnitude of the perturbations. In this project, we are interested in a FBG base F-P multiplexed fibre sensor to monitor temperature changes at different fixed points along the length of the fibre.

1.3. Problem Statement

In 1997, a twin-grating interferometric fibre sensor was presented (M. G. Shlyagin *et al.*, 1997) and aimed to monitor temperature and strain changes. The proposed setup of the twin-grating and its reflected spectra are presented in Figure 1-7.

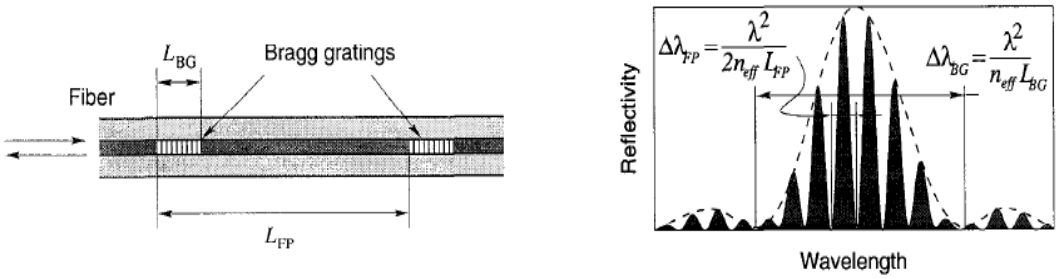

Figure 1-7. FBG Based F-P Layout (Left) and it's Reflection Spectrum (Right).

The FBGs that form the cavity have identical characteristics (wavelength and weak reflectivity) and are therefore twins. M. G. Shlyagin *et al.* clearly state that the sensor is the space between the twin-grating. Using FBGs of identical wavelength, M. G. Shlyagin *et al.*, 1997 also show theoretically that the sensor system can be implemented on a serial array in frequency division multiplexing. In such a case, the identification of one sensor to another in the network relies on their respective cavity length. When the sensor system is implemented in a wavelength division multiplexed system, the twin-gratings are identical in each respective local sensor and differ from one another in their respective wavelength and cavity length. Hence, equal low-reflectivity for all. The reflection spectra of the composite signal for the sensor system is presented in Figure 1-8.

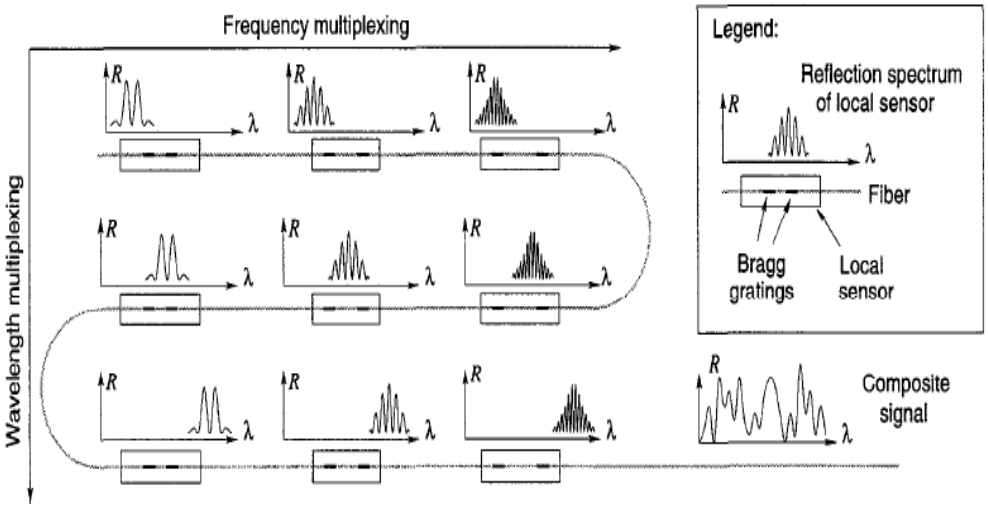

Figure 1-8. Composite Reflection Spectra of F-P Sensor as well as the WDM Spectra.

M. G. Shlyagin *et al.*, 1997 theoretically describe the proper working principles of such a fibre sensor, supported by equations. These equations include the minimal separation between two consecutive local sensors, the minimal separation between two consecutive cavities and the minimum and maximum cavity length. In their demodulation system, it was also predicted that in a multiplexed system, each local sensor can be interrogated individually. Therefore, M. G. Shlyagin *et al.*, 1997 completely laid down the foundation of the F-P based twin-grating fibre sensor.

Based on the work presented by M. G. Shlyagin *et al.*, 1997, a theoretical demodulation of the F-P based twin-grating fibre sensor applied to temperature and strain was developed (S. V. Miridonov *et al*., 2001). In their demodulation model, they applied fast Fourier transformation to the captured spectra. As result, this transformation yields triangle shapes centred at the frequency of the respective local sensors. The frequency response of a local sensor (twin-grating) is presented in Figure 1-9.

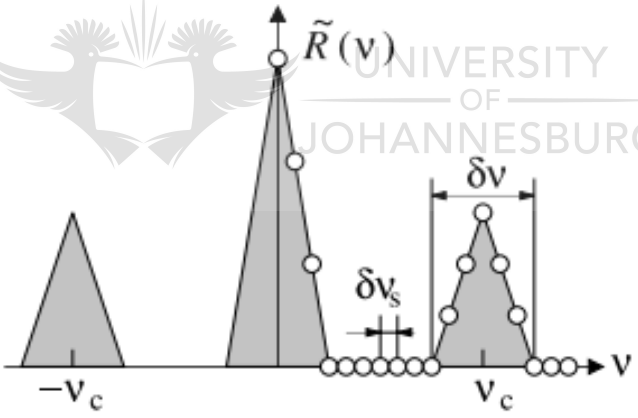

Figure 1-9. Spectral Response of the Local Sensor in Fourier Domain.

On Figure 1-9, v_c represents the frequency of the interference of the twin-grating as shown in Figure 1-7, while $-v_c$ is a reflection of the frequency of the sensor. In frequency division multiplexing (FDM) setup, the frequency of the interference from the twin-grating changes with the cavity length.

S. V. Miridonov *et al*., 2001 clearly showed that changes in temperature induces changes in phase, which is calculated thereafter using their demodulation algorithm. This demodulation

algorithm can be applied to a multiplexed system. S. V. Miridonov *et al*., 2001 further demonstrated that the phase response to temperature changes in a multiplexed system is linear.

In this thesis, we are interested in applying the theory described by M. G. Shlyagin *et al.*, 1997 and the demodulation algorithm presented by S. V. Miridonov *et al*., 2001 to a practical project, whereby the sensor system is made of 9 local sensors on a serial array of optical fibre interferometers. In this sensor system, local sensors are practically imprinted on the single mode telecommunication fibre. A correlation between the findings related to the sensor system presented in this project and those of M. G. Shlyagin *et al*., 2002, and S. V. Miridonov *et al*., 2001 are discussed.

The efficient and proper working conditions of the twin-grating fibre sensor was theoretically presented through mathematical equations, in which consecutive triangle shapes should not overlap (M. G. Shlyagin *et al*., 2002). This limits the number of local sensors in the serial array. Increasing the number of local sensors in the array might lead to a situation whereby they come closer in their spatial distribution. Using the mathematical equations presented by M. G. Shlyagin *et al*., 2002 and practical experiments, further investigations are considered in a situation whereby the local sensors on the array overlap in Fourier domain. The findings should clearly elucidate the limitations in the performance of the local sensors compared to their accuracy. The findings shall reveal the behaviour of the sensor in each respective case and dictate a trade-off between the multiplexing capabilities of the sensor system compared to its sensing accuracy.

1.4. Project Objectives

The objectives of this project are to design, simulate, build and conduct experimental testing on the multi-point temperature optical fibre sensor based on a serial array of optical interferometers. The sensor system is implemented in a combined frequency division multiplexing (FDM) and wavelength division multiplexing (WDM) arrangement. A sensor system of 20 local sensors per channel, spatially separated by 50 cm from each other with a resolution of 0.01℃ and a temperature sensitivity of 10 $\frac{pm}{℃}$ are targeted in this project.

Also, the theoretical and experimental investigation of two consecutive local sensors in a design where the spectrum of two local sensors comes closer touching each other of about 25

%, 50 % and 75 % in their Fourier domain, which is intended as a goal as well as the amplification of the sensor system for dynamic monitoring applications.

1.5. Chapters' Overview

A clear description and the working principles of the FBG and the interferometric sensors are discussed and outlined in Chapter 2. In order to contextualize this project, a state of the art temperature interferometric optical fibre sensor is presented.

In Chapter 3, the simulation of the multi-point temperature optical fibre sensor is introduced using mathematical equations. The sensors interrogated in the simulated systems are demodulated using the algorithm presented by S. V. Miridonov *et al*., 2001. The cross talks are analysed in order to evaluate their impact on the performance of the sensors.

In Chapter 4, experimental setup description and their respective procedures are presented. These setups include the multi-point fibre sensor system of 9 local sensors and the experimental investigation of the two local sensors that overlap in Fourier domain.

In Chapter 5, the results of all the experiments performed for this project are discussed. These results include the performance of the quasi-distributed system followed by a discussion of findings.

In Chapter 6, the conclusion of the project is presented as well as possible future investigations based on the results obtained.

2. Intrinsic Fabry-Perot Interferometric Fibre Sensor

2.1. Introduction

Intrinsic fibre Fabry-Perot interferometric sensors are good candidates for strain and temperature sensing. They have attracted considerable interests over the last few decades (C. E. Lee and H. F. Taylor, 1988). Intrinsic Fabry-Perot (F-P) cavities have been implemented using different configurations. The potential of using cavities formed by ultra violet (UV) induced fibre Bragg gratings (FBGs) of weak reflectivity for large multiplexing capacity is enormous. However, the printing of UV induced FBG's internal mirrors and the signal detection of low power reflection have been challenging tasks. In this chapter, FBGs used as mirrors in the F-P configuration are introduced, as well as their theoretical working principles and multiplexing. The important sections in this chapter relate to the F-P interferometer working principles and recent progress in F-P intrinsic temperature fibre sensors.

2.2. Fibre Bragg Grating

The fundamental properties of fibre Bragg gratings (FBGs) have been discussed in several books (K. T. V. Grattan and B. T. Meggitt, 2000; A. Othonos and K. Kalli, 1999). Fibre Bragg grating (FBG) is a periodic perturbation of the refractive index along the fibre length, which is formed by exposure of the core to intense UV radiation. Since the discovery of the FBG in 1978 (K. O. Hill, *et al.,* 1978), FBGs have been widely used in sensing applications in areas including temperature monitoring, strain sensing, stress monitoring, et cetera. FBGs are robust and comprise a huge multiplexing capability, hence suitable to be embedded directly into structures. Therefore, they are used as mirrors forming the cavities in the multi-point temperature fibre sensor based on a serial array of optical fibre interferometers, presented in this project. The principle of the FBG is presented in Figure 2-1.

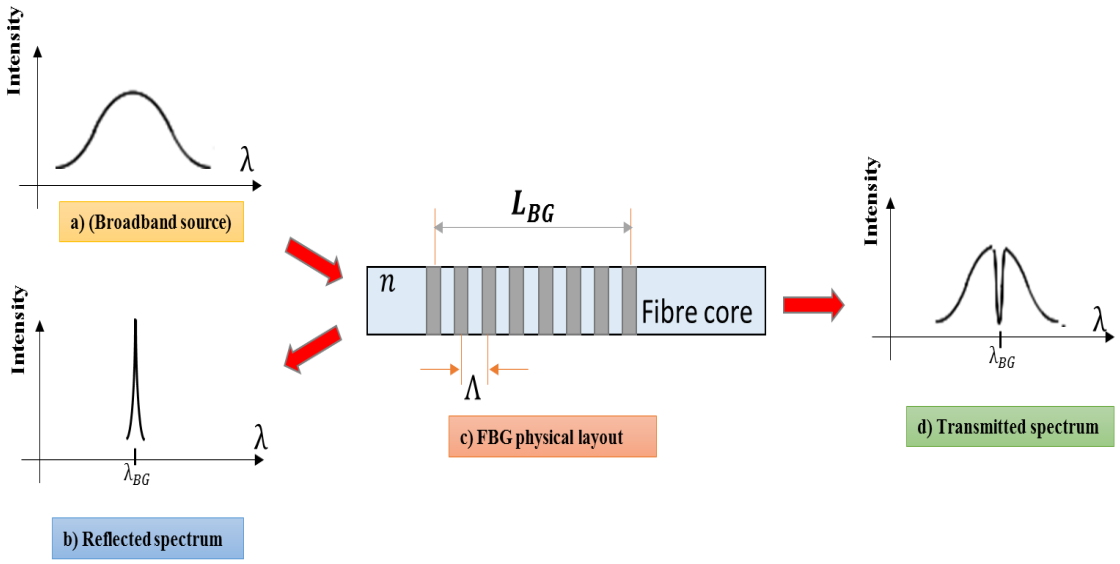

Figure 2-1. FBG Principles of operation.

Figure 2-1 a) is the spectral representation of the broadband source that is launched inside the optical fibre that propagates to the FBG. The reflected spectral shape centred to the Bragg wavelength is represented in Figure 2-1 b), while the transmitted spectral shape is represented in Figure 2-1 d).

In a uniform FBG, the phase fronts are perpendicular to the longitudinal axis of the fibre and the grating planes are of a constant period, as illustrated in Figure 2-1 c). When light propagates in the optical fibre, it interacts with each grating plane. A narrow band of the incident optical field within the fibre is reflected by successive, coherent scattering from the index variations. The strongest interaction or mode coupling occurs at the Bragg wavelength given by (R. Kashyap, 1999).

$$\lambda_{BG} = 2 \wedge n_{eff} \,, \qquad (2-1)$$

where: λ_{BG} is the Bragg wavelength, $\wedge$ is the grating period and n_{eff} is the effective refractive index of the core of the fibre.

From Equation 2-1, it is clear that any change in FBG properties, change the Bragg wavelength. Since the period of the grating depends upon these physical parameters, it is possible to realise a basis for a simple sensor such as the FBG sensor. Considering a uniform grating formed inside the core of an optical fibre with an average refractive index n_0. The refractive index profile can be expressed as:

$$n(z) = n_0 + \Delta n cos\left(\frac{2\pi z}{\Lambda}\right) \quad (2-2)$$

where: Δn represents the modulation amplitude of the refractive index, typically ranging from 10^{-5} to 10^{-3} and z the distance along the longitudinal axis of the fibre.

The reflectivity of the grating illustrated in Figure 2-1 b) which represents the physical amplitude or the intensity of the reflected wave having a constant refractive index modulation amplitude is derived using a coupled mode theory (D. K. W. Lam and B. K. Garside, 1981) as:

$$R_{BG}(L_{BG}, \lambda_{BG}) = \left(\frac{\Omega^2 sinh^2(s \times L_{BG})}{\Delta\beta^2 sinh^2(s \times L_{BG}) + s^2 cosh^2(s \times L_{BG})}\right), \quad (2-3)$$

where: $R_{BG}(L_{BG}, \lambda_{BG})$ is the reflectivity of the FBG which is a function of the grating length (L_{BG}) and Bragg wavelength (λ_{BG}), Ω is the coupling constant for sinusoidal variation in the refractive index perturbation represented by:

$$\left(\Omega = \frac{2\pi\Delta n}{\lambda}\right) M_{Power}, \quad (2-4)$$

where: M_{Power} represents the fraction of the fibre mode power contained by the core of the fibre always approximated to $1 - V^2$, where V represents the normalised frequency of the fibre given by: $\left(\frac{2\pi}{\lambda}\right) a\sqrt{n_{co}^2 - n_{cl}^2}$ such that $'a'$ represents the core diameter of the fibre and n_{co} and n_{cl} representing respectively the core and cladding refractive index.

From Equation 2-3, $\Delta\beta$ is the detuning wave vector represented by:

$$\left(\Delta\beta = \beta - \left(\frac{\pi}{\lambda}\right)\right), \quad (2-5)$$

With β as the propagation constant defined by:

$$\left(\beta = \frac{2\pi n_0}{\lambda}\right), \quad (2-6)$$

And:

$$s^2 = \Omega^2 - \Delta\beta^2. \quad (2-7)$$

According to Equation 2-3, the reflectivity of the FBG and its wavelength have been designed as sensor elements (Y. J. Rao, 1997), reflectors to form F-P interferometers (M. G. Shlyagin, 1997) inside the optical fibre, dispersion compensation (J. A. R. Williams, 1994), and optical filters (C. R. Giles, 1997) et cetera.

2.3. Fibre Bragg Grating Sensor

FBG sensors have excelled in being embedded to smart structure (R. M. Measures *et al.,* 1992) for real time monitoring of physical parameters which include temperature (A. D. Kersey and T. A. Berkoff, 1992), strain (A. D. Kersey *et al.,* 1992), vibration (W. Thongnum *et al*., 2002), acceleration (S. Theriault *et al.,* 1996), pressure (S.C. Tjin *et al.,* 1998) et cetera.

Fibre Bragg grating sensors are easily printed on the fibres, are good candidates for mass production, have high wavelength selectivity, possess multiplexing capabilities such as wavelength division multiplexing (WDM), time division multiplexing (TDM) (C. R. Giles, 1997) et cetera. They make absolute measurements, since they are insensitive to fluctuations in the irradiance of light source. Furthermore, the measurements made are obtained through the shift of the Bragg wavelength induced by the physical parameter.

Most of the research on the FBG as sensors has been focused on using them to monitor strain and temperature as point sensors, quasi-distributed sensors et cetera. As a sensor, the shift in Bragg wavelength induced by the physical disturbance is mainly due to two parameters, namely temperature and strain perturbations (G. Meltz and W.W Morey, 1991). The temperature response of the FBG arises from the temperature dependence of the refractive index and to the inherent thermal expansion of the fibre material. The strain response arises from the elongation of the FBG with respect to fractional changes in the grating periodicity and the changes in the refractive index due to the photo elastic-effect.

If we apply temperature changes to Equation 2-1 at constant strain, we have the following Equation:

$$\Delta\lambda(T) = 2\left[\frac{n\delta\wedge}{\delta T} + \frac{\wedge\,\delta n}{\delta T}\right]\Delta T, \qquad (2-8)$$

If we divide Equation 2-8 by Equation 2-1 we have:

$$\frac{\Delta\lambda(T)}{\lambda_{BG}} = \frac{2\left[n\delta\wedge + \wedge\delta n\right]\Delta T}{2\wedge n_{eff}} = \left[\left(\frac{1}{\wedge}\right)\left(\frac{\delta\wedge}{\delta T}\right) + \left(\frac{1}{n}\right)\left(\frac{\delta n}{\delta T}\right)\right]\Delta T, \qquad (2-9)$$

The sensor wavelength variation with respect to temperature is given by:

$$\Delta\lambda(T) = \lambda_{BG}\left[\left(\left(\frac{1}{\wedge}\right)\left(\frac{\delta\wedge}{\delta T}\right)\right) + \left(\left(\frac{1}{n}\right)\left(\frac{\delta n}{\delta T}\right)\right)\right]\Delta T. \qquad (2-10)$$

Equation 2-10 provides the two main characteristics of the FBG namely the thermal expansion represented by $\alpha_{\wedge}$and the thermo-optic effect represented by ς_n as shown in Equation 2-11.

$$\Delta\lambda(T) = \lambda_{BG}(\alpha_{\wedge} + \varsigma_n)\Delta T. \qquad (2-11)$$

where: $\alpha_{\wedge} = \left(\frac{1}{\wedge}\right)\left(\frac{\delta\wedge}{\delta T}\right)$ and $\varsigma_n = \left(\frac{1}{n}\right)\left(\frac{\delta n}{\delta T}\right)$.

The thermal expansion is related to the change in geometric structure of the fibre while the thermo-optic effect arises from the temperature dependence of the mode refractive index $\left(\frac{\delta n}{\delta T}\right)$ (Y. J. Rao, 1997). When the FBG is exposed to temperature, the observed wavelength shift in silica fibre is dominated in the order of 95% by the thermo-optic effect as compared to the thermal expansion. At constant strain, the normalised temperature response is represented by (A. D. Kersey *et al.*, 1997):

$$\frac{1}{\lambda_{BG}}\frac{\delta\lambda_{BG}}{\delta T} = 6.67 \times 10^{-6}{}^{\circ}\mathrm{C}^{-1}, \qquad (2-12)$$

where δT is the changes in temperature.

The temperature response of the gratings is calculated using different demodulation algorithms schemes. These demodulation algorithms play a significant role in extracting the external perturbation information from the spectral shift of the grating. In this regard using silica fibre, temperature sensitivities as function of wavelength are reported such as $6.35\,\frac{pm}{^{\circ}C}$ in the 800 nm region (D. F. Murphy *et al.*, 2001), $10.85\,\frac{pm}{^{\circ}C}$ in the 1300 nm region (A. L. Triques *et al.*, 2003) and $13\,\frac{pm}{^{\circ}C}$ in the 1550 nm region (Y. J. Rao *et al.*, 1996).

2.3.1. The Quasi-distributed Fibre Bragg Grating Sensor

One of the most popular fibre sensors, used in quasi-distributed sensing, is the FBG sensor – the reason for its popularity being the advantages associated with multiplexing and simplicity. A quasi-distributed FBG sensor network is made up of a number of point FBG sensors spaced along the fibre length. The layout of the quasi-distributed FBG sensor is presented in Figure 2-2.

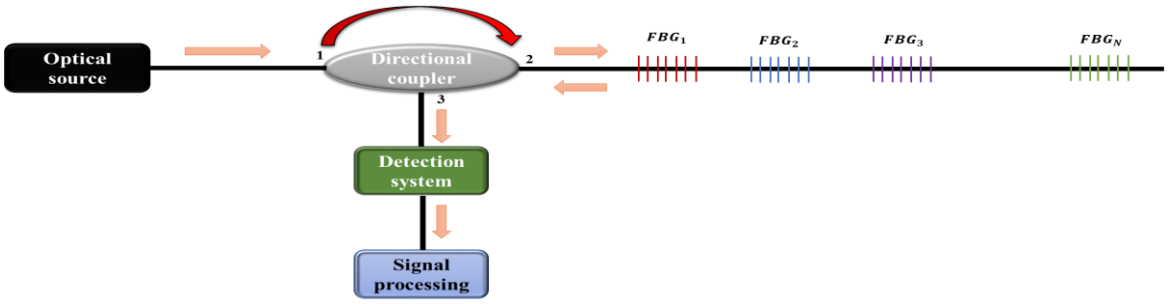

Figure 2-2. WDM Serial Array FBG Sensor Configuration.

The FBG point sensors on the network are printed on the fibre and all share the same detection system. Using the same optical source and detection system and demodulation considerably reduces the system cost. The individual point FBG sensors are separated from one another with certain designed intervals.

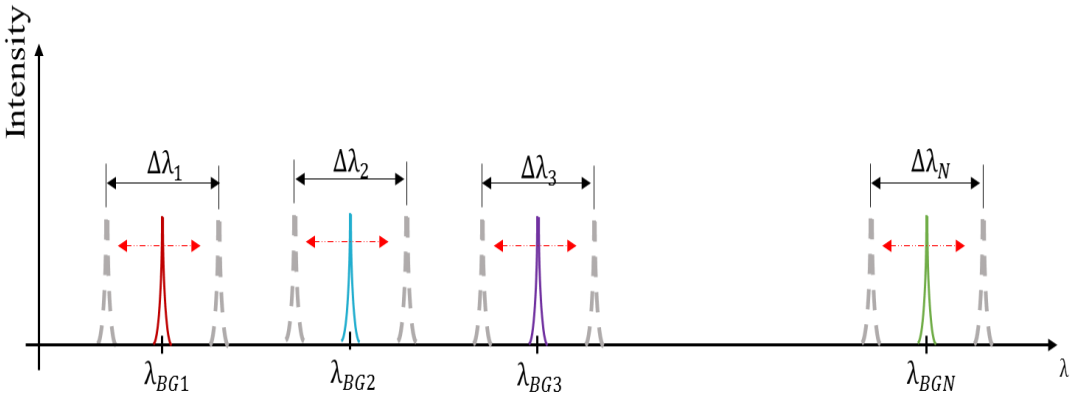

Figure 2-3. Spectral Shift of the Gratings in the Network.

In this section, we limit ourselves to presenting the quasi-distributed FBG sensor in wavelength division multiplexing (WDM) and time domain multiplexing (TDM).

In a WDM configuration, the FBGs are identical in their respective reflectivity, but differ in wavelength. They can be implemented in serial or parallel arrays, whilst a distinctive sensor on

the network can be directly interrogated. The number of FBG sensors that can be multiplexed is limited by the spectral range of the optical source, detection system and the wavelength spacing between consecutive local FBG sensors (C. Crunelle *et al.*, 2009).

In a TDM system, the Bragg gratings are interrogated by a short pulse of incident light that has enough bandwidth to measure the desired sensing range. They are identified by the time it takes for the optical signal to arrive at the fast scanning detection system. The FBGs are identical in wavelength and their reflectivity must be kept low to ensure that a sufficient portion of the optical power reaches the last sensor in the system. The reflectivity of the gratings must be greater than the losses introduced from the optical filter. The losses generated by the optical filter impact on the amplitude reflected spectrum from the respective FBG sensors. Such low power signal (0.2%) in a scanning system cannot be detected by the photo-detector. Thus, the signal discrimination between gratings is enhanced by the used of some types of time sensitive element as presented by (T. A. Berkoff *et al*., 1995) and (M. L. Dennis *et al*., 1997). The optical setup of such system is presented in Figure 2-4.

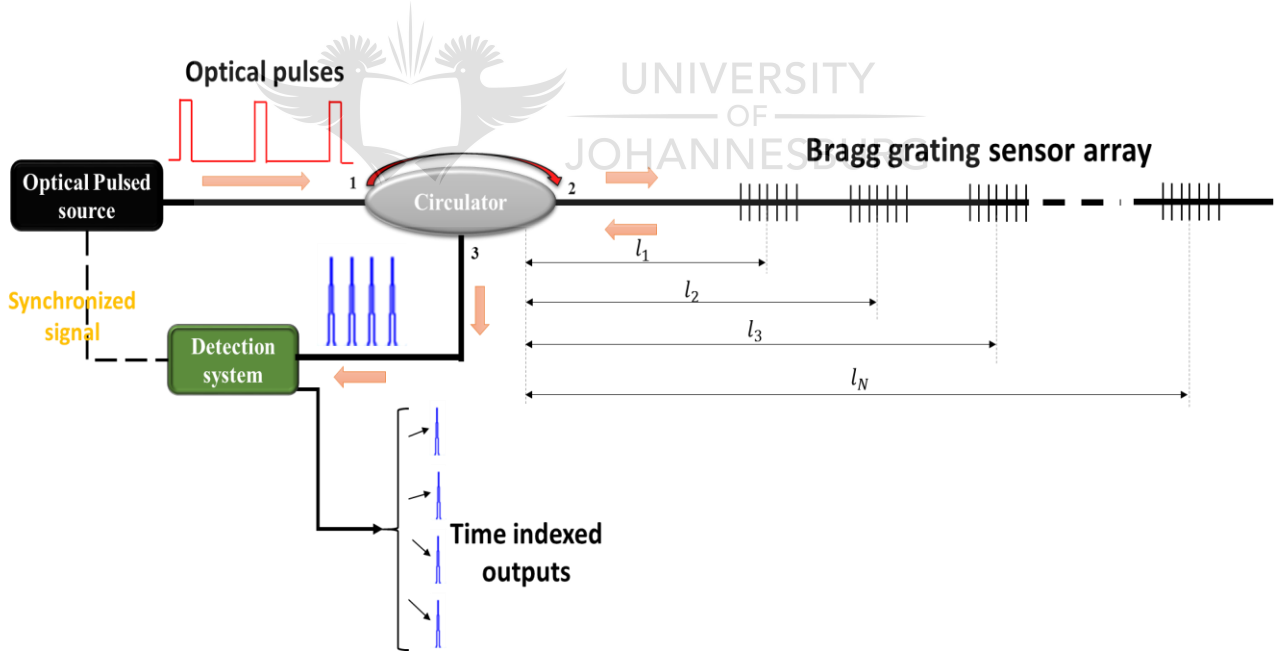

Figure 2-4. TDM principles using FBG sensor array.

The pulses reflected by the fibre Bragg gratings pass through the dispersive fibre. Because the group delay of the fibre fluctuates with wavelength, the Bragg wavelength of each of the gratings is evaluated by measuring the time for the reflected pulses to traverse the length of dispersive fibre such as follows:

$$t_i = \frac{2l_i}{nc}. \qquad (2-13)$$

where: *c* is the speed of light in vacuum and *n* is the fibre refractive index.

In T'DM systems, the very important considerations are to have each time slot to be as small as possible. This is aimed at having a large number of time slots available, and to have enough optical power reflected from each FBG point sensor. This allows the system to utilize a large number of sensors, such that they can be placed in close proximity to each other. Therefore, with WDM, tens of local sensors can be arranged on a single fibre. While using TDM, this number can be multiplied several times by re-using the spectrum of the optical source. This technique is commonly employed to support distributed sensors for the monitoring of temperature and strain. Having established the position of a grating in an array, a system of passive sloped filters is used to determine the wavelength of each pulse as it arrives.

2.4. The Fabry-Perot Interferometric Sensor

The fibre Fabry-Perot interferometer (FPI) is typically known as a multiple-beam device. The basic interferometer consists of two parallel partially-reflective mirrors opposing each other with reflectivities R_1 and R_2, both of which are separated by a cavity length, L_{F-P} (C. Fabry and A. Perot, 1899). The cavity is either of air or some transparent medium having a refractive index *n*. Applied in optical fibre sensors, the partially reflecting mirrors are printed on the fibre. They can be extremely sensitive to physical parameters and the sensing region can be made very compact. FPI can be classified as extrinsic (EFPI) or intrinsic (IFPI) (Q. Wang *et al*., 2011; W. H. Tsai and C. J. Lin, 2001).

In the EFPI configuration, the mirrors are formed out of the fibre. They have an air gap between them. When the mirrors are high in reflectivity, they can achieve a high finesse interference pattern (D. Hunger *et al*., 2010). EFPI fabrication is relatively simple, but suffers from problems such as alignment, low coupling efficiency and packaging (J. S. Sirkis *et al*., 1975). The layout of an EFPI is presented in Figure 2-5.

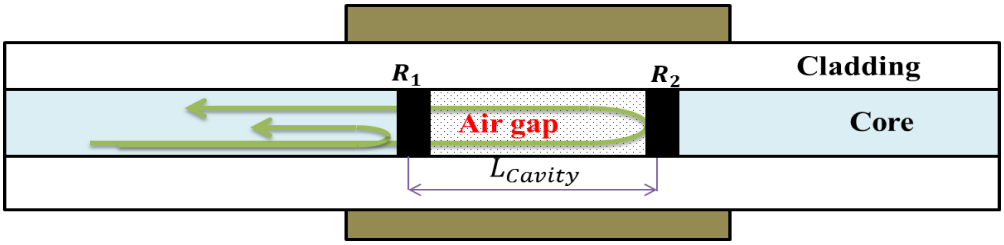

Figure 2-5. EFPI layout.

In some configurations, two portions of the fibre are highly polished to form the extrinsic mirrors separated by the air gap where $R_1$and R_2represent the reflectivities of the mirrors, as shown in Figure 2-5.

In the IFPI, the mirrors are incorporated within the fibre by micromachining (J. Ran *et al.*, 2009; T. Wei *et al.*, 2008), UV irradiation (Z. Wang *et al.*, 2007; X. Wan and H. F. Taylor, 2002), chemical etching (V. R. Machavaram *et al.*, 2007) or thin film deposition (J. R. Zhao *et al.*, 2010; P. Morris *et al.*, 2009). The drawback is the expensive equipment used for the fabrication of the F-P cavity. The layout of an IFPI composed of two FBG is presented in Figure 2-6.

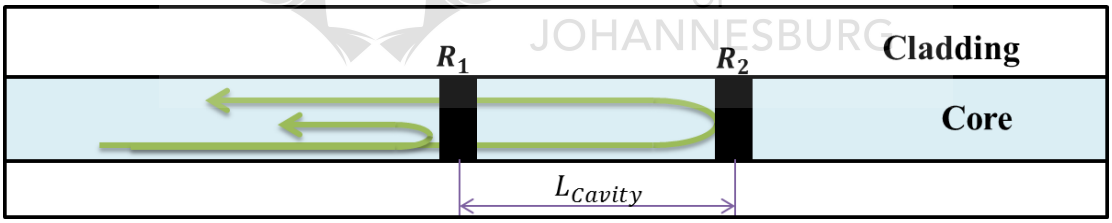

Figure 2-6. FPI sensor schematic layout.

A portion of the fibre whereby the two FBGs are imprinted using UV irradiation is shown. The Fabry-Perot interferometer is useful for high precision measurements, sensing and optical wavelength filtering.

2.4.1. Working Principles of the FPI Sensor

The optical setup of a F-P fibre interferometer based on the F-P etalon made of two partially reflective mirrors separated by a cavity is presented in Figure 2-7.

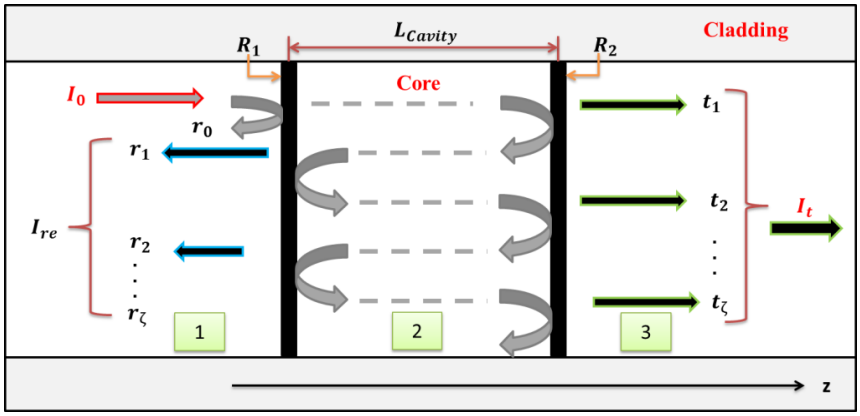

Figure 2-7. F-P Multiple Beam Interference Interferometer.

When an incident light spectrum (I_0) at an arbitrary angle is launched onto the cavity, multiple reflections are produced within the cavity. The intensity distribution of the reflected (I_{re}) and transmitted (I_t) beams renders it possible to generate interference on a detection system (F. L. Pedrotti et al., 2007). The distance between successive interference valleys or peaks is proportional to the separation (cavity length) between the two partially reflective mirrors.

The electrical field of the incident light that propagates in the z direction as presented in Figure 2-7 is written as:

$$E(x,y,z,t) = e(x,y)e^{-j\beta z}e^{j\omega t}; \qquad (2-14)$$

where: z is the propagation direction, t is time and β is the propagation constant.

Let us consider that light propagates from region i to region j. Consider r_{ij} and t_{ij} to be the respective complex amplitude reflection and transmission coefficients. If ζ is the maximum number of reflections in the cavity, the reflected (r_ζ) and transmitted (t_ζ) signal is presented as (Hernandez, 1986).

$$r_0 = r_{12}\,, \qquad (2-15)$$

$$r_\zeta = t_{12}t_{21}r_{23}(r_{21}r_{23})^{\zeta-1}e^{(-j\zeta\emptyset_{F-P})}; \qquad (2-16)$$

$$t_\zeta = t_{12}t_{23}(r_{21}r_{23})^{\zeta-1}e^{\left(-j\left(\zeta-\frac{1}{2}\right)\emptyset_{F-P}\right)}; \qquad (2-17)$$

where: $\emptyset_{F-P}$ is the phase delay caused by a single round trip of light inside the cavity and it is :

$$\emptyset_{F-P} = 2\beta(\lambda)L_{F-P}\,; \qquad (2-18)$$

where: L_{F-P} is the cavity length of the sensor, $\beta(\lambda)$ is the propagation constant, n is the refractive index and λ is the operational wavelength of the incident light.

The FPI total reflection and transmission complex amplitude coefficients r_{F-P} and t_{F-P} are the sum of all the reflection and transmission components respectively, presented as follows:

$$r_{F-P} = \sum_{\zeta=1}^{\infty} r_{\zeta} = \frac{r_{12} + (t_{12}t_{21} - r_{12}r_{21})r_{23}e^{(-j\emptyset_{F-P})}}{1 - r_{21}r_{23}e^{(-j\emptyset_{F-P})}}; \qquad (2-19)$$

$$t_{F-P} = \sum_{\zeta=1}^{\infty} t_{\zeta} = \frac{t_{12}t_{23}e^{\left(-j\frac{1}{2}\emptyset_{F-P}\right)}}{1 - r_{21}r_{23}e^{(-j\emptyset_{F-P})}}\,; \qquad (2-20)$$

When the two partially transmissive mirrors are identical in their respective characteristics, the reflectivity and the transmission from the above equations are such as:

$$R = r_{12}r_{22} = r_{21}r_{23}\,, \qquad (2-21)$$

$$T = t_{12}t_{21} = t_{12}t_{23}\,, \qquad (2-22)$$

Introducing the Equations 2-21 and 2-22 into the Equations 2-19 and 2-20, we have:

$$r_{F-P} = \frac{r_{12}\left(1 - e^{(-j\emptyset_{F-P})}\right)}{1 - Re^{(-j\emptyset_{F-P})}}; \qquad (2-23)$$

$$t_{F-P} = \frac{Te^{\left(-j\frac{1}{2}\emptyset_{F-P}\right)}}{1 - Re^{(-j\emptyset_{F-P})}}\ ; \qquad (2-24)$$

The reflectivity power known as the Airy function is represented by:

$$R_{F-P} = \frac{2R\left(1 - cos(\emptyset_{F-P})\right)}{1 + R^2 - 2Rcos(\emptyset_{F-P})} = \frac{Fsin^2\left(\frac{\emptyset_{F-P}}{2}\right)}{1 + Fsin^2\left(\frac{\emptyset_{F-P}}{2}\right)}; \qquad (2-25)$$

where: $F = \frac{4R}{(1-R)^2}$ is known as the finesse of the fringes of the spectrum.

A typical reflection spectrum of the FPI is presented in Figure 2-8.

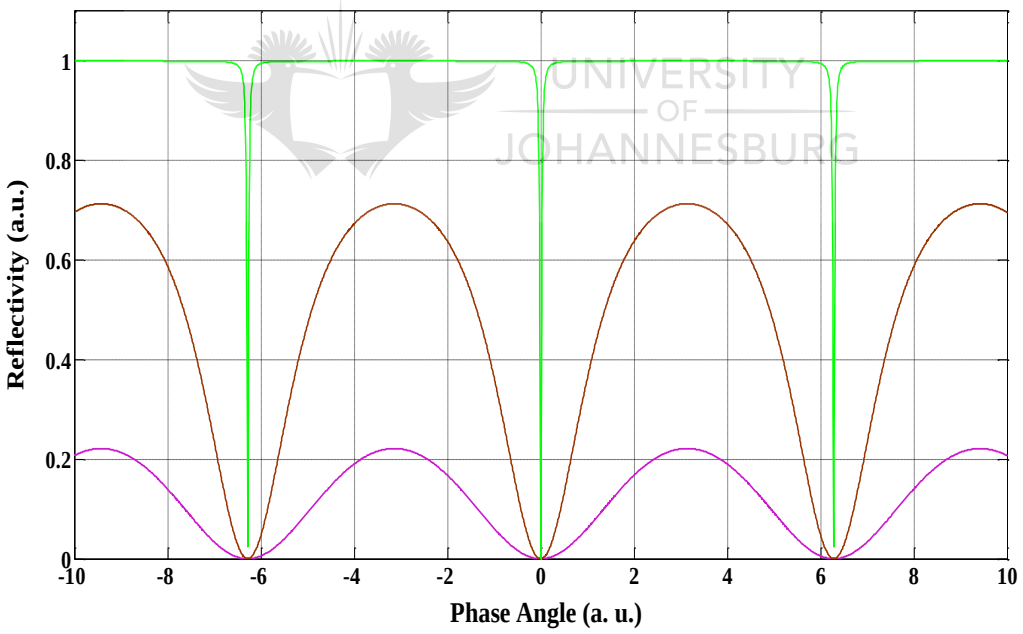

Figure 2-8. Typical FPI Reflection Spectrum.

From Equation 2-18, the phase is directly related to the refractive index *n* and the cavity length. When the external perturbations are applied to the system, the refractive index and the cavity length change – as does the phase – and the reflected spectrum shifts. Therefore, by monitoring the shift of the reflected spectrum, the FPI could be used as an optical fibre sensor. Compared

to the other fibre interferometers, the F-P interferometer generally has at least twice the sensitivity, due to its multiple reflections.

2.5. Fibre Bragg Grating Based Fabry-Perot Fibre Sensor

In the FBG based F-P sensor system, the sensor is made of two identical gratings printed on the optical fibre and separated by a cavity L_{F-P}. The identical gratings are of weak-reflectivity. In such situation, the system is reduced to a two wave interference. Its basic configuration is presented in Figure 2-9.

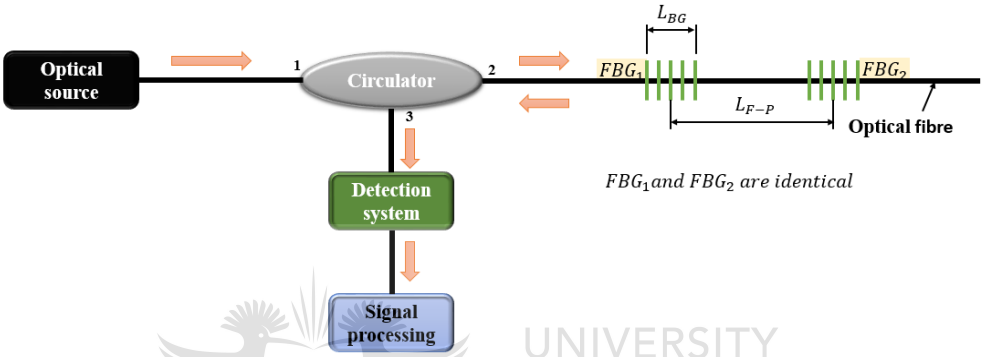

Figure 2-9. FBG Based F-P Interferometric Sensor Configuration.

A zoomed representation of the weak-reflectivity identical-grating F-P sensor is presented in Figure 2-10, purposely for a description of its working principles.

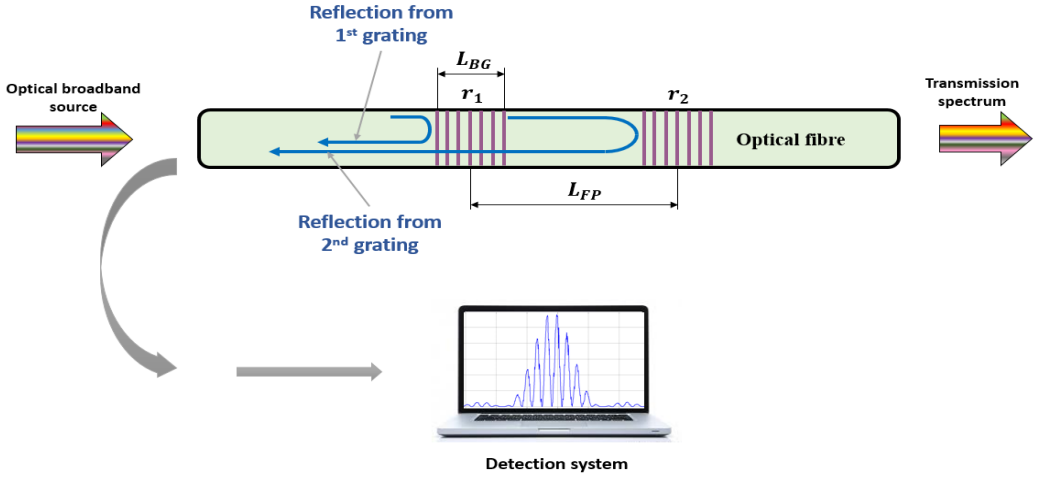

Figure 2-10. Twin-grating fibre sensor configuration.

As presented in Figure 2-10, r_1 and r_2 represent the reflectivity of the identical-gratings and their respective transmissions are represented by t_1 and t_2. The identical-gratings are separated by a distance represented by L_{F-P}.

When the broadband source spectrum is coupled into the fibre, it experiences a first reflection represented by r_1 and a second reflection represented in complex format by $r_2 e^{-i\emptyset_{F-P}}$. The remaining light spectrum is transmitted as presented in Figure 2-10. The two reflected light spectrum are now propagating in the same direction towards the optical source, generating an interference centred to their Bragg wavelength, observed on the detection system as shown. This interference pattern is theoretically derived as a sum of both reflected signals.

$$r_{Tot} = r_1 + r_2 e^{-i\emptyset_{F-P}}, \qquad (2-26)$$

where: $e^{-i\emptyset_{F-P}}$ represents the phase difference between the two reflections

Since both gratings are of identical characteristics, we can assume:

$$r_1 = r_2 = r_{BG}, \qquad (2-27)$$

Substituting Equation 2-27 into Equation 2-26 gives the following:

$$r_{Tot} = r_{BG}\left(1 + e^{-i\emptyset_{F-P}}\right), \qquad (2-28)$$

The reflected spectrum using Equation 2-28 in conjugate format is represented by:

$$R_{F-P}(\lambda_{BG}) = r_{BG}\left(1 + e^{-i\emptyset_{F-P}}\right) \times r_{BG}\left(1 + e^{i\emptyset_{F-P}}\right), \qquad (2-29)$$

By developing Equation 2-29 gives the followings:

$$R_{F-P}(\lambda_{BG}) = r_{BG}^2\left[1 + 1 + \left(e^{i\emptyset_{F-P}} + e^{-i\emptyset_{F-P}}\right)\right]; \quad (2-30)$$

By applying complex numbers identity,

$$e^{i\emptyset_{F-P}} + e^{-i\emptyset_{F-P}} = 2\,cos(\emptyset_{F-P}); \quad (2-31)$$

Substituting Equation 2-31 into Equation 2-30 yields the following:

$$R_{F-P}(\lambda_{BG}) = r_{BG}^2\left(2 + 2cos(\emptyset_{F-P})\right) = 2r_{BG}^2\left(1 + cos(\emptyset_{F-P})\right); \quad (2-32)$$

Considering that $r_{BG}^2 = R_{BG}$, the total reflected spectrum of the weak-reflectivity identical-grating sensor is presented by:

$$R_{F-P}(\lambda_{BG}) = 2R_{BG}(\lambda_{BG})\left(1 + cos(\emptyset_{F-P})\right); \quad (2-33)$$

where: R_{BG} represents the reflectivity of the identical-gratings and $\emptyset_{F-P}$ represents the F-P phase angle of the interfering spectrums shown in Equation 2-3.

$$\emptyset_{F-P} = 2\beta(\lambda_{BG})L_{F-P} = 2\left(\left(\frac{2\pi n}{\lambda}\right) \times L_{F-P}\right); \quad (2-34)$$

A complete expression of the total reflected spectrum is presented as follows:

$$R_{F-P}(\lambda_{BG}) = 2 \times \left(R_{BG}(\lambda_{BG})\right) \times \left(1 + \cos\left(\frac{4\pi n L_{F-P}}{\lambda}\right)\right); \quad (2-35)$$

Equation 2-35 is constituted of two main function mainly the envelope function represented by the spectrum of the gratings.

$$E_{function} = 2 \times R_{BG}(\lambda_{BG}), \qquad (2-36)$$

and the modulated function represented by a constant and the cosine.

$$M_{function} = \left(1 + \cos\left(\frac{4\pi n L_{F-P}}{\lambda}\right)\right). \qquad (2-37)$$

If the wavelength variation is minor, then the modulated function can be expressed as (S. V. Miridonov *et al*., 1997).

$$M_{function} = \left(1 + \cos\left(\frac{4\pi n L_{F-P}}{\lambda_{BG}^2}(\lambda - \lambda_{BG})\right) + \emptyset_0\right). \qquad (2-38)$$

where $\emptyset_0 = \frac{4\pi n L_{F-P}}{\lambda_{BG}}$ is the maximum phase shift of the cosine function.

The frequency of the interference pattern of the twin-grating can be derived from Equation 2-38 as:

$$M_{function} = \left(1 + \cos\left(2\pi f(\lambda - \lambda_{BG})\right) + \emptyset_0\right), \qquad (2-39)$$

Where this frequency can be represented as (M. G Shlyagin et al., 1997).

$$f = \frac{2nL_{(F-P)}}{\lambda_{BG}^2} \ ; \qquad (2-40)$$

The change of optical path translates into a change in the phase of the output from the interfering light signal. The operational range is determined by the bandwidth of the overlapping FBGs.

From Equation 2-35, the quantity to be measured is the change in phase of the interference pattern in radian, per degree and per unit length, as presented by (R. Martinez Manuel, 2009).

$$\frac{\Delta\emptyset_{F-P}}{\Delta T L_{F-P}};$$

where: $\Delta\emptyset_{F-P}$ is the change of the phase in radians and ΔT is the change of temperature in degree Celsius.

By applying temperature changes in Equation 2-34, we have the following:

$$\frac{\Delta\emptyset_{F-P}(T)}{\Delta T} = \frac{4\pi}{\lambda}\left(\frac{n\delta L}{\delta T} + \frac{L\delta n}{\delta T}\right); \qquad (2-41)$$

Dividing Equation 2-41 by Equation 2-34 we have the following:

$$\frac{\Delta\emptyset_{F-P}(T)}{\emptyset_{F-P}} = \frac{\frac{4\pi}{\lambda}\left(\frac{n\delta L}{\delta T} + \frac{L\delta n}{\delta T}\right)\Delta T}{\left(\frac{2\pi n}{\lambda}\right)2L_{F-P}}\ ; \qquad (2-42)$$

Using simplifications, the above equation is represented by:

$$\frac{\Delta\emptyset_{F-P}(T)}{\emptyset_{F-P}} = \left(\left(\frac{1}{L}\frac{\delta L}{\delta T}\right) + \left(\frac{1}{n}\frac{\delta n}{\delta T}\right)\right)\Delta T; \qquad (2-43)$$

where: $\left(\frac{1}{L}\frac{\delta L}{\delta T}\right)$ represents the thermal expansion component and $\left(\frac{1}{n}\frac{\delta n}{\delta T}\right)$ represents the thermo-optic effect component.

Therefore, the changing phase as a function of changing temperature over the cavity length is represented by:

$$\frac{\Delta\emptyset_{F-P}(T)}{\Delta T L} = \frac{4\pi n}{\lambda}(\alpha_{\wedge} + \varsigma_n)\ ; \qquad (2-44)$$

where: $\alpha_\wedge$represents the thermal expansion coefficient and ς_n represents the thermo-optic effect coefficients.

In these circumstances, using a SMF fibre, with the refractive index n = 1.46, thermal expansion coefficient $\alpha_\wedge = 0.55 \times 10^{-6}\,℃^{-1}$, thermo-optic effect coefficient $\varsigma_n = 8.6 \times 10^{-6}\,℃^{-1}$ (H. S. Ohn and R. M. Measures, 1995) and $\lambda = 1550\,nm$, the phase expectation per length is defined as (R. Martinez Manuel, 2009).

$$\frac{\Delta\emptyset_{F-P}(T)}{\Delta TL} = 108{,}3\frac{rad}{m\,℃}. \qquad (2-45)$$

2.6. Multiplexed Fabry-Perot Interferometric (FPI) Sensor Arranged in FDM and WDM

The multiplexed (FPI) sensor system consists of local sensors in a serial array spaced at fixed distances from one another along the whole length of the fibre. Each local sensor is made of two identical FBGs of low-reflectivity. Using FBGs of low-reflectivity, many local sensors can be printed on the same optical fibre. The optical layout of the multiplexed F-P interferometric sensor is presented in Figure 2-11.

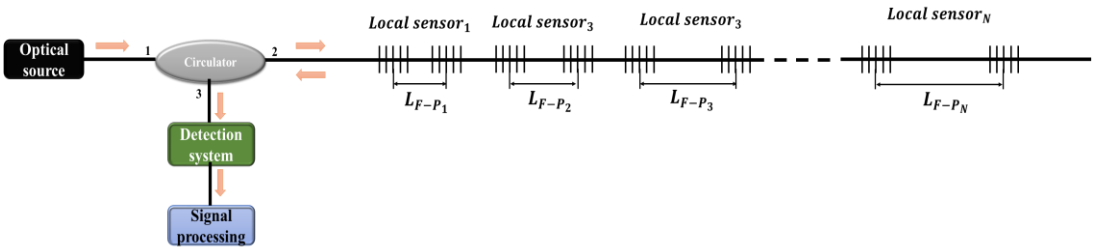

Figure 2-11. FDM Sensor Setup.

When the multiplexed F-P interferometric sensor is configured in a frequency division multiplexing (FDM), all the FBGs are identical in their respective wavelengths and reflectivities. Local sensors differ from one another by their respective cavity length. By having cavities of different length, many local sensors can be implemented on the array. The separation between consecutive local sensors must be designed with precision in order to avoid an overlap of information between them, which might lead to errors.

When the system is implemented in a wavelength division multiplexing (WDM), the Bragg wavelength of each respective local sensor differs from one cavity to the other, but with identical reflectivity for all the gratings.

When the light from the Broadband source is coupled into the fibre where the local sensors forming the multiplexed sensor system is, it propagates to the first local sensor. In this first local sensor, a small percentage of the incident light is reflected from the first and second gratings. These two reflected light waves from the identical FBGs create an interference as they propagate in the direction of the source. The transmitted light which propagates to the second local sensor, is again reflected from the two gratings and a second interference pattern is created. This process is repeated until the last local sensor of the system is reached.

In FDM, the interference patterns generated by each local sensor superimpose to produce the total reflection spectrum displayed on the detection system in the wavelength domain. In WDM, each respective local sensor interference pattern occupies a narrow width on the working spectrum space and is centred to each respective Bragg wavelength. In both cases, the total reflected spectrum is theoretically expressed as:

$$R_{(F-P)_{Tot}}(\lambda_{BG}) = 2\sum_{j=1}^{N} R_{BG_j}(\lambda_{BG})\left[1 + cos(\emptyset_{F-P_j})\right], \qquad (2-46)$$

where: $R_{(F-P)_j}(\lambda)$ is the reflection spectrum from the j^{th} local sensor and N is the number of local sensors in the system.

2.7. Recent Progress in F-P Temperature Fibre Sensors

Optical fibres have been involved in the area of sensing applications for more than four decades. During this time, numerous types of interferometers have been developed by researchers, considering improvement in functionality, efficiency and potential implementation in sensing applications. In this regard, Fabry-Perot Interferometric (FPI) fibre sensors have been extensively investigated for their effectiveness and simple fabrication.

A section of the trend have focussed their studies in developing Fabry-Perot fibre sensors using a combination of three different optical fibres, namely the Single Mode Fibre (SMF), Photonic Crystal Fibre (PCF) and the Hollow Optical Fibre (HOF) as such utilised by H. Y. Choi *et al*. In this respect, an in-line F-P high temperature fibre sensor was developed (H. Y. Choi *et al*.,

2008). In this configuration, a small piece of HOF – having a 40 μm air-hole and 125 μm outer diameter – is fusion spliced between a PCF and a short length of SMF, serving as cavity and having well-cleaved end faces. A super luminescent emitting diode (SLED) is used as broadband source to provide light to the optical system, where the HOF is used as a micro-air gap. When the SLED is on, as light propagates inside the sensor, it is reflected at the end face of the PCF and then reflected at the two end faces of the single mode fibre (SMF). The reflections at the SMF generate an interference pattern. The structure of their proposed sensor is presented in Figure 2-12.

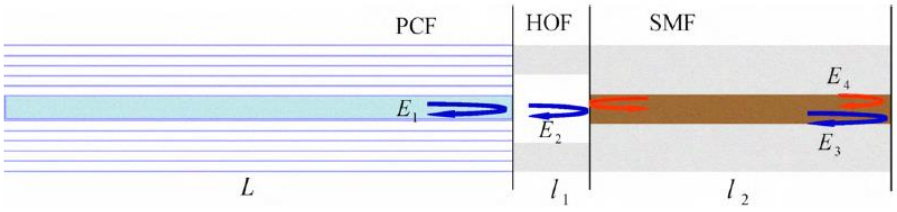

Figure 2-12. F-P interferometer Sensor Head.

The sensor fabrication only required cleaving and splicing. The HOF length was extremely controlled during splicing in order to achieve high interference fringe contrast using a high resolution micro-translation stage. In order to avoid the collapse of the air-hole at both PCF and SMF during the splicing, the fusion was made with a particular arc condition. The overall sensor head length was about 580 um comprising 70 μm of HOF and 510 μm of SMF. An optical spectrum analyser (OSA) was used to capture the interference pattern. The captured interference pattern centred at 1535 nm is presented in Figure 2-13.

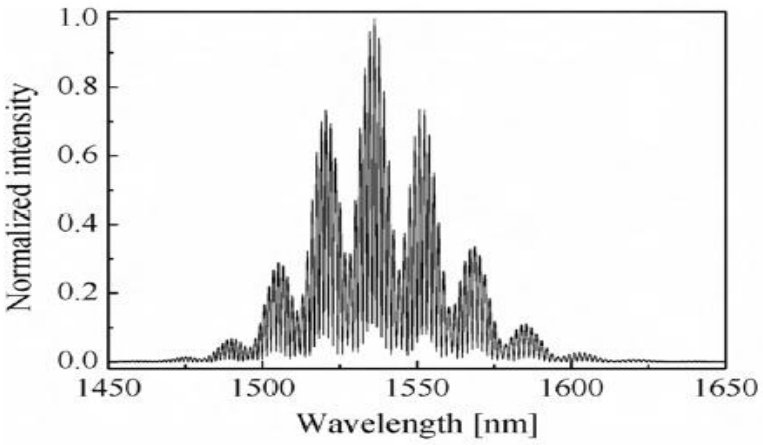

Figure 2-13. Reflection Spectrum of the F-P Sensor.

It is observed that high frequency interference fringes, formed by the SMF cavity, are enveloped with low frequency interference fringes produced by the micro-air-gap. In their demodulation, an interferogram was used and the spatial frequency spectrum was calculated by taking the fast Fourier transform. This is illustrated in Figure 2-14.

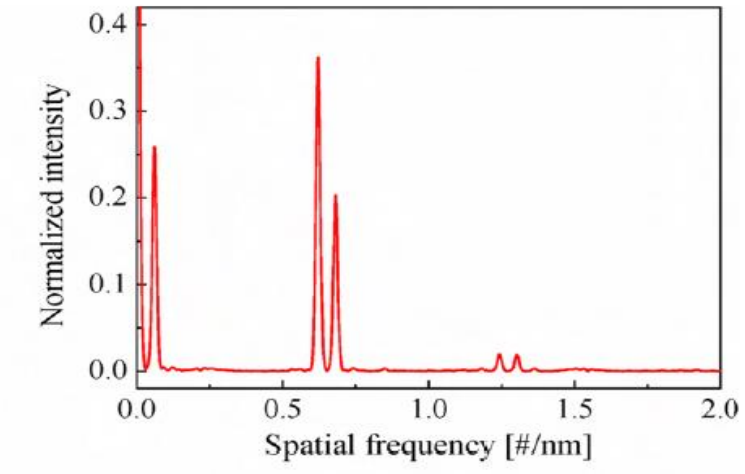

Figure 2-14. Spatial frequency Spectrum of the F-P Sensor.

The spectrum presented in Figure 2-14 clearly shows the impact of the four reflection beams of the interference spectrum. In this report, they sensed temperatures from 50℃ *to* 1000℃, with a resolution of 50℃. It was found that the higher frequency interference fringes were shifted towards longer wavelength direction, while the envelope was kept unchanged all along the experiment. It was also shown that temperature dependency of the HOF length was considerably small and should be neglected in practical applications, while the spatial frequency was increased with temperature.

They concluded that the temperature sensitivity can be controlled by a proper design of the length of the SMF. This temperature sensitivity might furthermore be improved by the addition of dopants in the core of the SMF, as they concluded.

In the same period of time, other researchers focused their studies in dense multiplexing using a single mode fibre to monitor temperature changes. In this instance, a fibre Fabry-Perot interferometric sensor based on twin Bragg gratings of ultra-short and low-reflectivity was reported (Z. Wang *et al.*, 2007, building on M. G. Shlyagin *et al.*, 1997). The sensor was designed to monitor temperature and strain changes in an arrangement of 50 local frequency division multiplexed sensors. The twin-grating were all identical, that is, of the same

reflectivity and wavelength. The cavity length of respective local sensors ranged from 450 μm to 5450 μm, with 100μm increments. The experimental setup and the local sensor structure is presented in Figure 2-15.

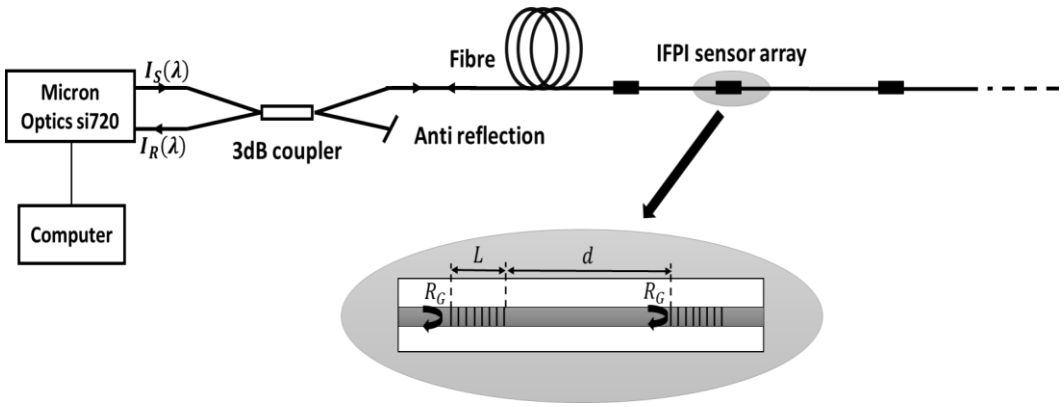

Figure 2-15. Optical Setup for Dense Multiplexing.

The sensor system working principles were exactly stated by M. G. Shlyagin *et al*., 1997 and S. V. Miridonov *et al*, 2001. The interrogation of the sensor signal was enabled by using the Micron Optics si720 sensor monitoring system. This comprised an extremely low-noise tuneable fibre laser and a high precision optical spectrum analyser (OSA). Using low reflectivity twin-gratings and having short cavity lengths between them, the total reflected signal is a linear superposition of all respective local sensors signals (presented in Figure 2-16).

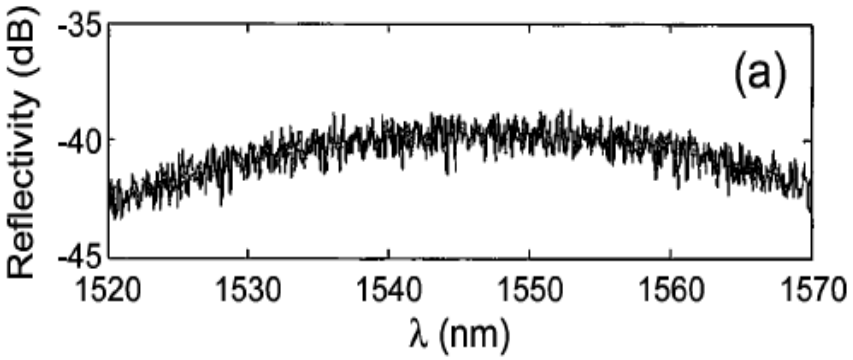

Figure 2-16. Total Reflected Spectrum of the Sensor System.

Five local sensors were exposed to temperature changes from 0℃ to 170℃, with 10℃ increments. These local sensors were placed inside chambers and were observed at 20 minutes

per increment. The total reflected signal from all the local sensors in the array was coupled into the OSA by a 3-dB optical coupler and thereafter to the computer for demodulation. The total reflected signal was captured on the OSA. Applying discrete Fourier transform on the total reflected signal captured on the OSA, each respective interrogated local sensor was represented by a discrete peak corresponding to its frequency (based on F. Shen and A. Wang, 2005). The transformed signal was band pass filtered and then Hilbert transformed. The sensing interrogation system was based on the measurement of the relative peak wavelength shift in the local sensor's reflection spectrum, induced by the physical parameter. The problem of the 2π ambiguity form the cosine part of the interfering spectrum was solved as presented by S.V. Miridonov *et a*l., 2001 using linear regression. A temperature and strain sensitivity of $6.21\,\frac{ppm}{℃}$ and $0.773\,\frac{ppm}{\mu\epsilon}$ were measured. A temperature and strain resolution of 0.1℃ and $1.3\mu\varepsilon$ were achieved.

Some researchers took advantage of the Erbium doped fibre in a F-P fibre sensor configuration, whereby the Er doped fibre was used to provide the broadband light source to the local sensors (UV printed in a parallel array). Moving forward in this prospect, a new technique of multiplexed FBG based sensor to monitor temperature was presented (X. Wan and H. F. Taylor, 2003). The sensing element was formed by a pair of FBGs in a low-finesse Fabry-Perot configuration. The pair gratings were identical in their respective wavelengths and reflectivities. The separation between grating pairs was different from one sensing point to the other. Their optical setup is presented in Figure 2-17.

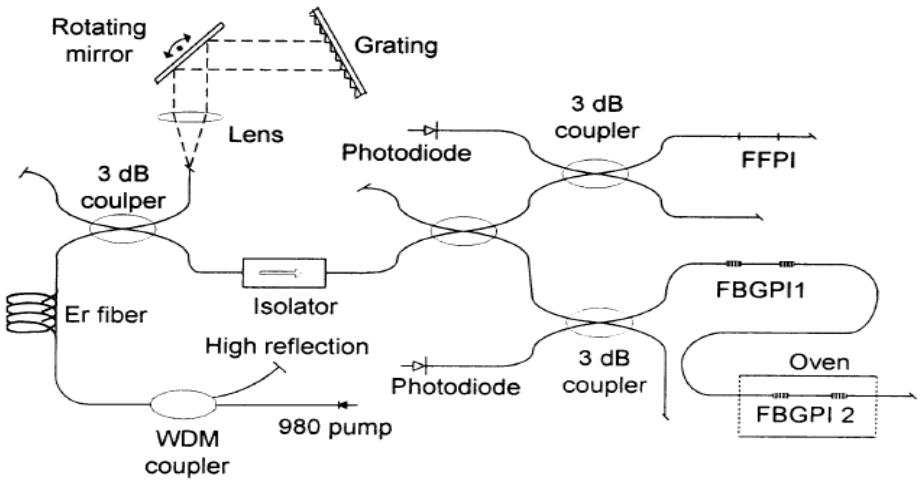

Figure 2-17. Optical Setup.

In their experiment, a linearly chirped Erbium doped fibre was used as a light source with a rotating galvanometer as a rotating element. The power of the optical source varied 46 nm spectral range corresponding to 1dB. As presented on Figure 2-18, the respective sensing elements are $FBGPI_1$ and $FBGPI_2$, displayed in a serial array. The reflectivity of the grating pair was 1%, while the cavity length of the sensing elements was 12 mm and 14.5 mm respectively. The other interferometer FFPI was aimed at monitoring the chirp rate of the laser and to correct the nonlinearities in that chirp. In this interferometer, the reflectors forming the cavity comprised 5% reflectivity each. They were fusion spliced in a short length single mode fibre. $FBGPI_2$ was placed inside an oven and was exposed to temperature changes from room temperature up to $360\,℃$, while $FBGPI_1$ was kept at constant room temperature for comparison.

In their demodulation process, the exposed sensor signal was convoluted with in-phase and quadrature components of a reference waveform. This was aimed as measuring the optical frequency of the peak of the grating reflectance. The convoluted signal was evaluated over a frequency range and the magnitude of the phase could then be calculated. The result of the phase shift over frequency range is presented in Figure 2-18.

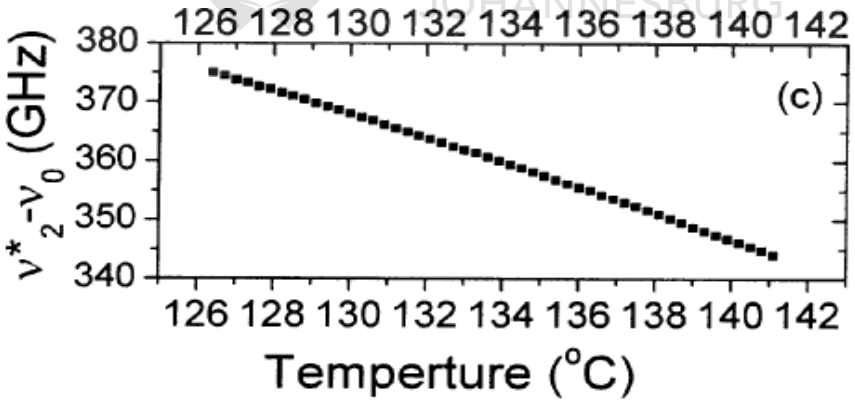

Figure 2-18. FBGPI Response to Temperature Changes Evaluated Using Phase Shift.

This multiplexed sensor system was composed of two sensing points as presented in Figure 2-18 and a spectral resolution of 0.045 GHz, correspondence with a temperature resolution of 0.035 was completed.

In the very early days of the Fabry-Perot interferometric fibre sensor, certain other research groups were intensely implementing the design of the sensor cavity using twin-gratings and

establishing a theoretical foundation in multiplexing. In their development, a twin Bragg grating Fabry-Perot sensor designed to monitor static strain and temperature was presented (M. G. Shlyagin *et al.*, 2002). This optical sensor system was aimed at measuring micro-strain with a large dynamic range. The sensor system was made of two local sensors imprinted on a single array of a single mode fibre. The two local sensors were made of FBGs of identical low-reflectivity (1%) and wavelength (1552.7), separated by a cavity 20 mm and 30 mm respectively. The two local sensors were separated from each other at 2.5 m distance to avoid crosstalk. The working principle of the sensor system was as described by M. G. Shlyagin *et al*., 1997. Before using the sensor system to strain monitoring, it was first used for temperature measurement. The two local sensors were placed inside a closed box, along with a temperature diode sensor. The disturbed signal was captured on the detection system as an overlap of the interference pattern from each of the local sensors. The captured spectrum was thereafter demodulated (according to S. V. Miridonov *et al*., 2001) in order to measure the magnitude of temperature changes. Using S. V. Miridonov *et al*., 2001 algorithm, the local sensors were represented as two triangle shapes centred to their respective frequencies. A temperature resolution of $0.02℃$ and a strain resolution of $0.2\frac{\mu m}{m}$ were achieved.

In the earliest stage, some sectors of the trend used the interface between two different fibre materials to form the sensor in a novel structure of an intrinsic Fabry-Perot fibre optic temperature sensor (Woo-Hu Tsai and Chun-Jung Lin, 2001). The system was mathematically modelled using the parameters of the SMF and a 3M single mode fibre. In their experiment, the optical fibres used had different core diameters of $8.3\ \mu m$ and $4\ \mu m$ respectively, while their claddings were identical at $125\ \mu m$. The sensor was aimed at measuring temperature changes as a function of the change in the reflectivity of the mirrors. The structure of the F-P sensor configured with the two different fibre core is presented in Figure 2-19.

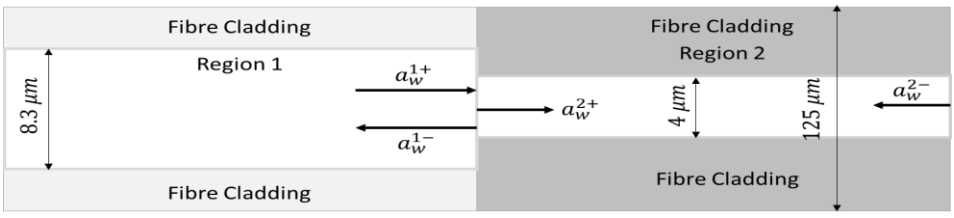

Figure 2-19. F-P Fibre Sensor with Different Fibre Core Layout.

In this experiment, the step index fibre was modelled with a fundamental mode function and with a cosine function near the axis, as well as an exponential like function far from the axis. The mode function is represented as:

$$\psi_t(R) \approx \begin{cases} cos(\gamma R) & R \leq 1 \\ tR^{-\frac{1}{2}}e^{sR} & R \geq 1 \end{cases}, \qquad (2-47)$$

where: $R = \frac{r}{\rho}$ with ρ as the core radius of the fibre, and γ as the only parameter which is variant. By applying the boundary conditions that require $\psi_t(R)$ and its derivative to be continuous at $R = 1$, the two constants t and δ can be determined by:

$$\begin{cases} s = \gamma tan(\gamma) - \frac{1}{2} \\ t = cos(\gamma)e^{\left(\gamma tan(\gamma) - \frac{1}{2}\right)} \end{cases}, \qquad (2-48)$$

Applying Mathematica software as a tool, the coefficient γ was calculated for the SMF (0.94555) and the 3M (1.2323) fibres using 1553.9 nm as wavelength and $c = 2.9979 \times 10^8 m/s$. The reflectance (6.18 %) and transmittance (93.82 %) of the reflectors were calculated to using the below theoretical formula:

$$\begin{cases} R = \left(\frac{K_{uv}^2 - 1}{K_{uv}^2 + 1}\right)^2 \\ T = \left(\frac{2K_{uv}}{K_{uv}^2 + 1}\right)^2 \end{cases}, \qquad (2-49)$$

where: K_{uv} represents the inner product between two modes at the junction.

The sensor system experimental setup is presented in Figure 2-20.

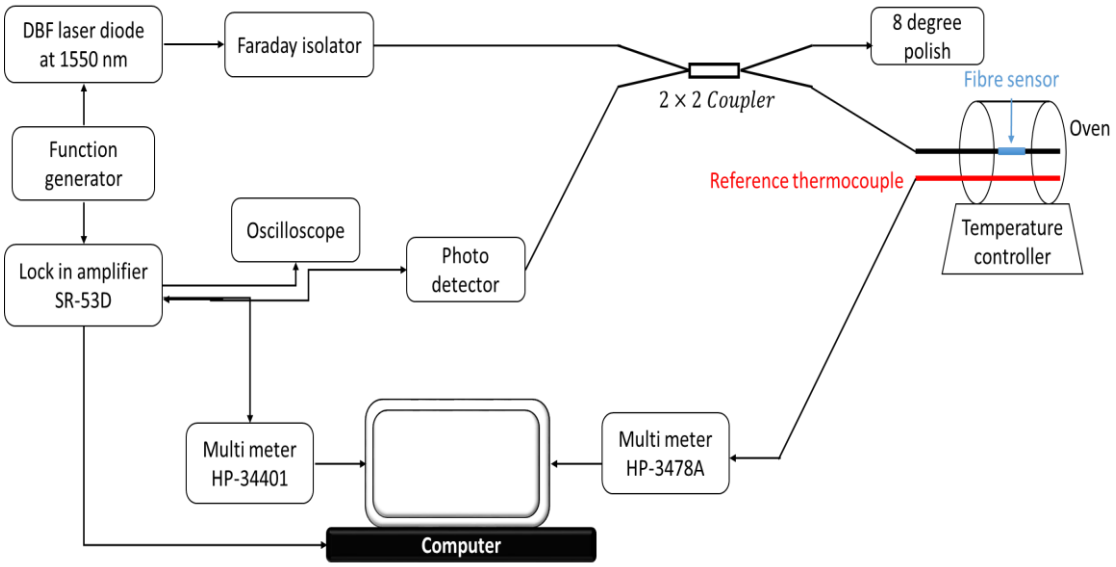

Figure 2-20. Optical Setup for the Experiment Performed.

Their experimental setup consisted mainly of a pig tail laser diode centred at 1553.9 nm, an InGaAs photo-detector, a fused bi-conical taper coupler, an optical filter et cetera. The sensor was equipped with a thermo-coupler and then placed inside an oven. The thermocouple (reference instrument) was equipped with a precision temperature controller with 0.5 ℃ increments every minute.

When light from the optical source was coupled into the F-P sensing head, as result of reflection at the interface of region 2 as presented in Figure 2-20, an interference pattern was generated. The phase shift is given by the following:

$$\Delta\delta = \frac{4\pi(\Delta nL)}{\lambda}, \qquad (2-50)$$

A measurement range from 30 ℃ to 250 ℃ was tested and the modulated captured interference pattern from the detection system was demodulated thereafter. The phase of the interference pattern as presented in Equation 2-50 was used to reveal temperature changes. In this regard, 4.31% and 3.96%, reflectivity of the mirrors was experimentally measured as compared to the theoretical calculation as presented in Figure 2-21.

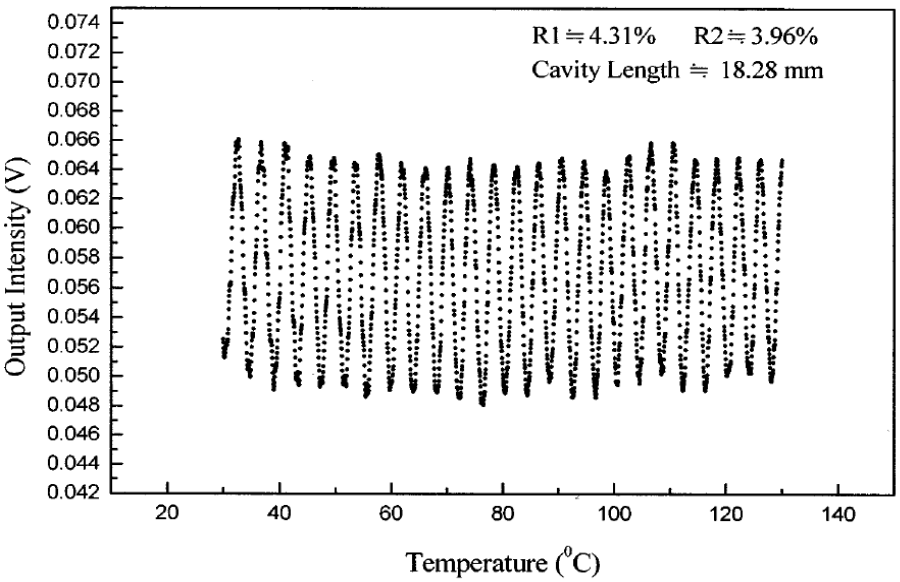

Figure 2-21. Reflectivity of the Mirrors as Function of Temperature Changes.

A dynamic range of the sensor that stretched from 30ºC up to 250 ℃, which was comparable to conventional IFPI, was achieved.

A significant section of the trend focussed on using low-reflectivity FBG to form the F-P cavity. This can be seen as one of the strong movements of the trend where theoretical and practical models have been reported. In this regard, an inline-intrinsic fibre Fabry Perot sensor based on collocated FBG in a low coherence configuration was developed and presented (S. C. Kaddu *et al.*, 1997). This F-P fibre sensor fabrication did not involve a cleave head, nor splicing. The F-P cavity was made using dielectric mirrors (FBGs), having a space between them. The FBGs were spaced closely to each other and had almost identical characteristics in reflectivity and in Bragg wavelength. In the multiplexed system, the collocated identical FBGs were equidistantly spaced form each other and their wavelength differed from one collocated cavity to the other. This optical system was simulated and their results compared to the experimental work. Experimentally, they imprinted 3 cavities on the fibre and their optical detection system was in transmission mode. When the sensor is illuminated, the expected normalised low coherence interference fringes are represented by:

$$P(x) = exp\left(\frac{-x^2}{(\Delta x)^2}\right) cos\left(\frac{2\pi x}{\Lambda}\right), \qquad (2-51)$$

where: $\Lambda = \frac{\lambda}{2}$ is the fringe period, $\Delta x = \frac{\Lambda^2}{\Delta\lambda}$ determines the width of the Gaussian envelop, and the length parameter x is chosen as the variable for Equation 2-51, in order to compare the experiment to the simulation.

The results of the simulation in form of spectrums are presented in Figure 2-22 with Bragg wavelength around 827 nm, 829 nm and 831 nm and a reflectance band width of 0.6 nm.

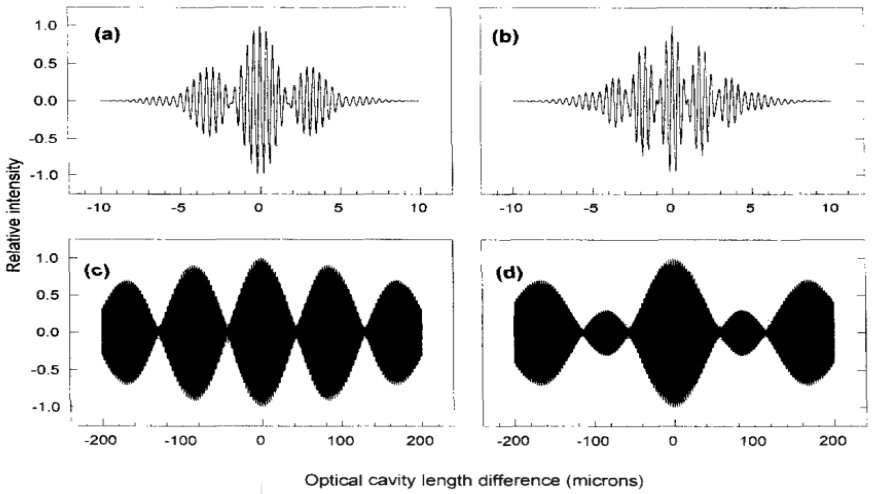

Figure 2-22. Spectrum of the Simulated Sensor System of Three Collocated Sensors with Different Wavelengths.

In their experiment, a triple cavity of collocated FBGs were printed on the fibre and the transmission spectrum presented in Figure 2-23, with a wavelength separation of 3.6 nm and band width of 0.6 nm, as captured on the optical spectrum analyser.

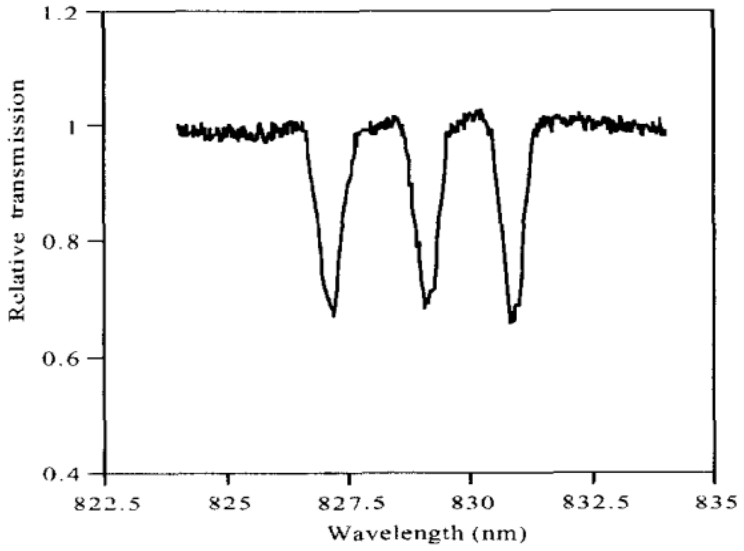

Figure 2-23. Transmitted Spectrum of the Sensor System made of 3 Collocated Grating Pairs.

The sensor was exposed to temperature changes from 20℃ to 60℃. The information retrieved from the sensor was derived using a chi-squared fitting technique (S. C. Kaddu, 1996) and the temperature response to temperature changes was linear. The behaviour of the experiment overlapped with the predictions from simulation.

At the same time in the development of the trend, a twin-grating based interferometric fibre sensor was presented (M. G. Shlyagin *et al*., 1997). Based on the work developed by M. G. Shlyagin *et al* in 1997. Miridonov *et al*., proposed a demodulation algorithm for the twin-grating based sensors using a Fourier transform (FT) (Miridonov *et al*., 2001), as presented in Chapter 1.

Even though it is very difficult to clearly find an overlap in the setup, demodulation and results in the recent progress presented above, all the sensors described aimed for an effective, accurate and efficient system. We therefore take advantage of the above recent progress in the Fabry-Perot interferometric fibre sensor in terms of theoretical background and the demodulation system needed to experimentally design and test the multipoint sensor system presented in this project.

2.8. Summary

The functioning of the Fabry-Perot fibre sensors – as well as other interferometric fibre configurations – have been discussed in this Chapter. This is followed by recent progress in Fabry-Perot interferometric fibre sensors for temperature monitoring, presented and discussed in full. The serial array is implemented on the single mode telecommunication fibre (SMF 28), where local sensors are printed and therefore simulated as presented in chapter 3.

3. Simulation of the Multi-point Temperature F-P Fibre Sensor

3.1. Introduction

The design and simulation of the multi-point fibre sensor, based on a serial array of optical fibre interferometers for temperature monitoring, is presented in this chapter. In the multi-point system, two different setups – including the wavelength division multiplexing (WDM) and the frequency division multiplexing (FDM) – implemented on the serial array are simulated. In these simulations, the interferometric configurations are based on the Fabry-Perot (F-P) interferometer using theoretical equations. The partially reflective mirrors used to form the F-P cavities are the FBGs of identical characteristics. The demodulation algorithm introduced in this chapter is based on S. V. Miridonov *et al*., 2001 to measure temperature changes at each respective interrogated local sensor. A further simulation of two local sensors is intended in order to find answers on the sensor response to temperature changes when the spectrum of two local sensors come closer and touch each other in Fourier domain, based on M. G. Shlyagin *et al*., 1997.

3.2. Simulation of the F-P Local Sensor

The F-P local sensor that is simulated in this section is composed of two weak-reflectivity identical gratings of 1550 nm wavelength and 1 % reflectivity and 1 cm cavity length. The optical setup is presented in figure 3-1.

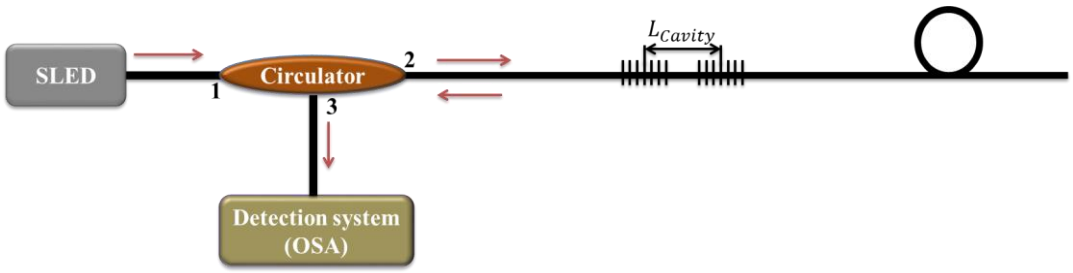

Figure 3-1. F-P local sensor optical setup for the simulation experiment.

The separation between the identical weak-reflectivity FBGs is designed to be 1 cm long for simplicity. Having such short separation between gratings, warrants fringed visibility. The FBGs are theoretically implemented on the single mode fibre (SMF), because it is the fibre to be used during experimental work and also because it can be found easily on market.

The theoretical illustration of the optical setup presented in Figure 3-1 is represented by:

$$R_{F-P}(\lambda) = 2 \times \left(\frac{\Omega^2 sinh^2(s \times L_{BG})}{\Delta\beta^2 sinh^2(s \times L_{BG}) + s^2 cosh^2(s \times L_{BG})} \right) \times \left(1 + \cos\left(\frac{4\pi n L_{F-P}}{\lambda} \right) \right); \quad (3-1)$$

Mat-Lab is used as tool to simulate Equation 3-1. In the simulation, a broadband wavelength of 8 nm centred around 1550 nm is sampled with a resolution of 5 pm representing signal from the optical source. The parameters of the SMF – such as the refractive index, thermal expansion and thermo-optic effect coefficients – are included into Equation 3-1 where the identical weak-reflectivity gratings are 1% reflectivity.

Temperature changes and a white noise having a Gaussian distribution are applied to Equation 3-1. Because the demodulation algorithm used in this project is based on changes in phase, any white noise added in amplitude should have minimal effect. In this sense, the white noise having a standard deviation of $\sigma = 0.1$ is added to the phase of Equation 3-1 represented by the cosine function. This noise represents the random fluctuation of the reflected signal from the first and the reflected signal of the second gratings. As the two reflected signals interfere, the phase of the interference pattern is corrupted by the added phase noise. This phase noise is mostly generated by vibration from the lab environment.

The sensor response to temperature changes is observed on the virtual detection system as a reflected interference in wavelength domain. The system is calibrated and a 1℃ temperature changes is incrementally applied to Equation 3-1 from 10℃ to 24℃. By applying temperature changes, the reflected interference pattern responds by a spectral shift. The spectrums of the calibrated and the measurement is presented in Figure 3-2.

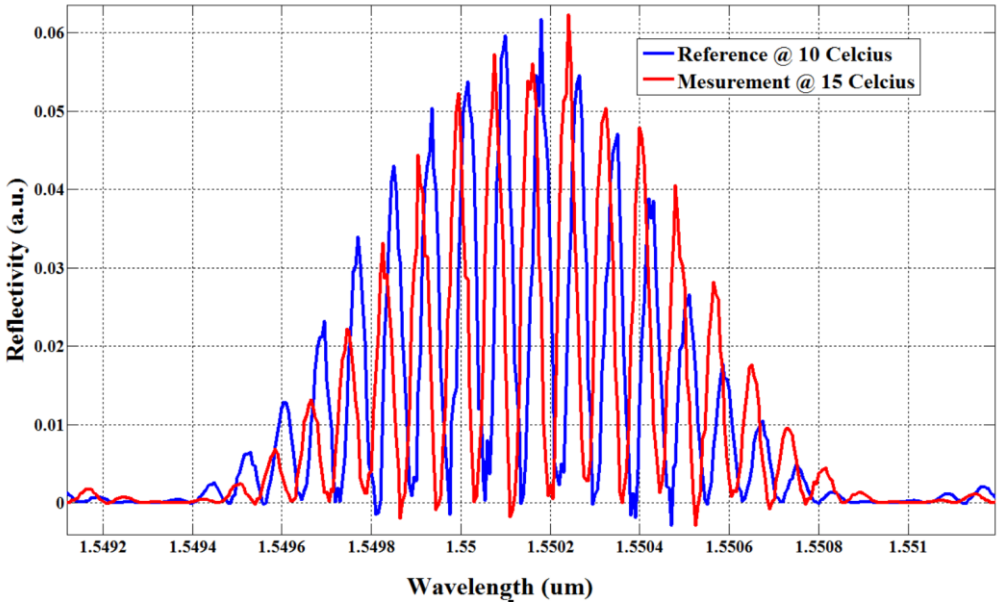

Figure 3-2. Reflected Spectra from the Undisturbed and Disturbed Sensor.

The spectrum in blue at 10℃ is the calibration while the spectrum in red represents the measurement at 15℃.

As observed, the interference pattern is centred at 1550 nm, as stated by the literatures. The ripples on the two spectrums result from the additional phase white noise having a Gaussian profile, as stated. The spectrum of the interference pattern observed on the detection system is fast Fourier transformed. This transformation yields triangle shapes as shown in Figure 3-3 that is fully explained in our demodulation algorithm.

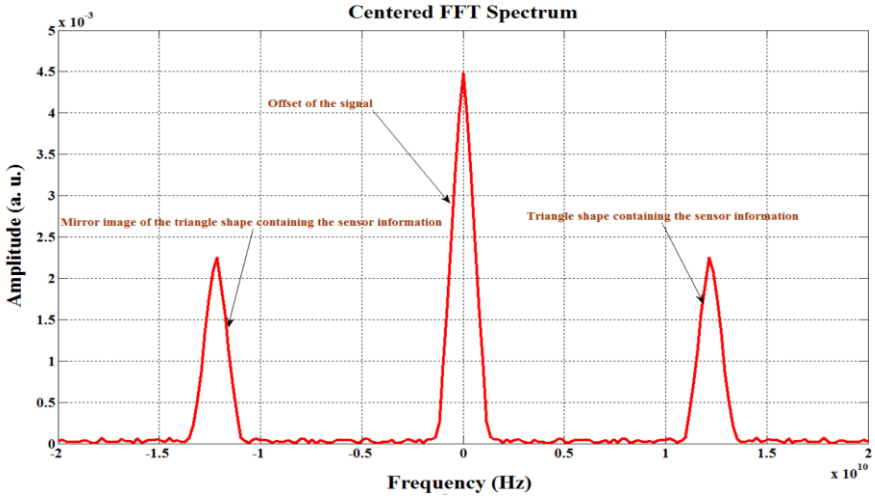

Figure 3-3. Centered FFT spectrum of the local sensor.

As shown on Figure 3-3, the triangle shapes are as expected and correlate to the literature. Using the demodulation algorithm presented by S. V. Miridinov *et al., 2001* in this project, temperature changes is calculated. The phase response of the F-P local sensor is presented in Figure 3-4.

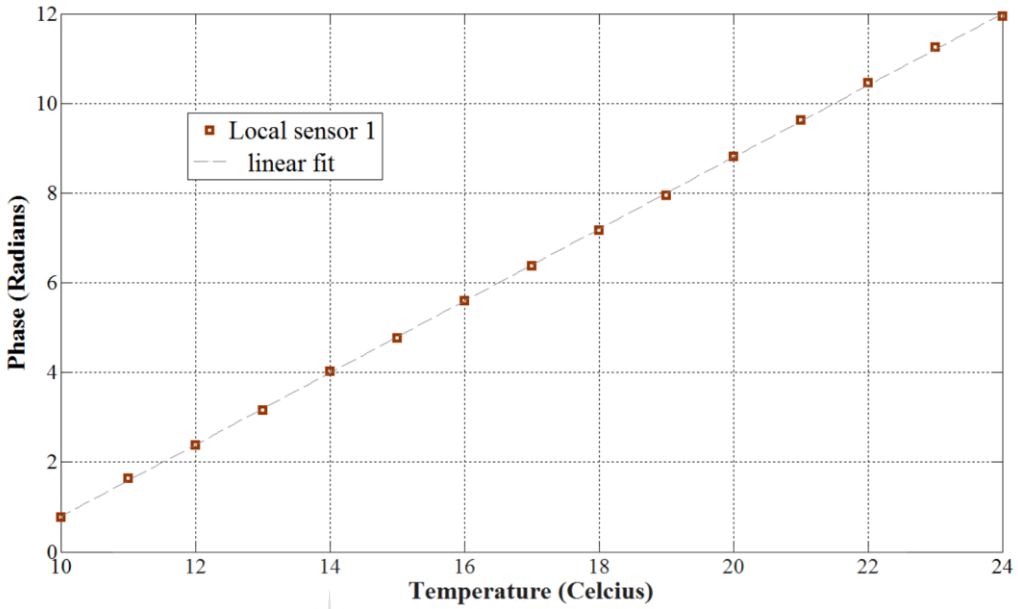

Figure 3-4. F-P Local Sensor Phase Response to Temperature Changes.

The F-P local sensor response to temperature changes being linear is shown as expected and is similar to the literature. Using the parameters of the single mode fibre in the simulation, the sensitivity is measured at $10\frac{℃}{pm}$. This measurement is expected. It is observed that with every 6℃ of temperature increment, a 2π cross over is observed.

3.3. Simulation of the Multi-point Temperature F-P Fibre Sensor Systems

The simulation of the multi-point temperature F-P fibre sensor is divided into two main parts, namely the frequency division multiplexing (FDM) and wavelength division multiplexing (WDM) configurations.

The first configuration addressed is the FDM, which consists of three F-P local sensors printed on the single mode fibre (SMF). Each F-P local sensor is made of identical gratings of weak-

reflectivity of 1% and wavelength 1550 nm. The cavity lengths are respectively 1 cm, 2 cm and 3 cm for the first, second and the third local sensor. Assuming that the coherence length of the source is larger than the third cavity length. In this sense, the interference pattern from each local sensor has its specific frequency defined by the characteristics of the SMF and the cavity length. The optical setup of the FDM sensor system is presented in Figure 3-5.

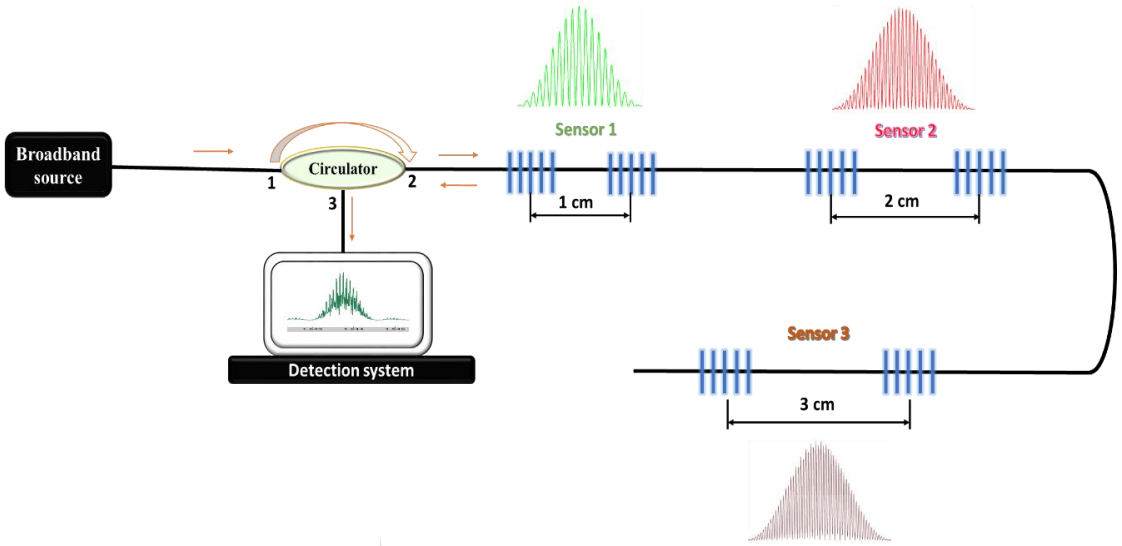

Figure 3-5. Optical Setup of the Multi-point F-P Fibre Sensor System Implemented in a FDM.

From design, the separation between consecutive F-P local sensors is set to 50 cm to avoid cross talking. The theoretical illustration of the optical system presented in Figure 3-5 is represented by:

$$R_{(F-P)_{Tot}}(\lambda) = 2\sum_{j=1}^{N}\left(\frac{\Omega^2 sinh^2(s \times L_{BG})}{\Delta\beta^2 sinh^2(s \times L_{BG}) + s^2 cosh^2(s \times L_{BG})}\right)_j \left[1 + cos(\emptyset_{L-P_j})\right]; \quad (3-2)$$

where: $R_{(F-P)_j}(\lambda)$ is the reflection spectrum from the j^{th} local sensor and N is the number of local sensors namely 3 in the system.

Using Mat-lab as a tool, Equation 3-2 representing the sum of all the reflected interference generated by the three local sensors in wavelength domain is simulated. This spectrum is a superimposition of all the local sensor spectrum. In the simulation, white noise with a Gaussian distribution and a standard deviation of $\sigma = 0.1$ is added to the phase of Equation 3-2 represented by the cosine function. Temperature is also applied to Equation 3-2 with an increment of 1°C. The system is calibrated to 10°C and temperature changes is applied to all 3

local sensor. Data is simulated from 10℃ to 20℃. This total reflected spectrum is presented in Figure 3-6.

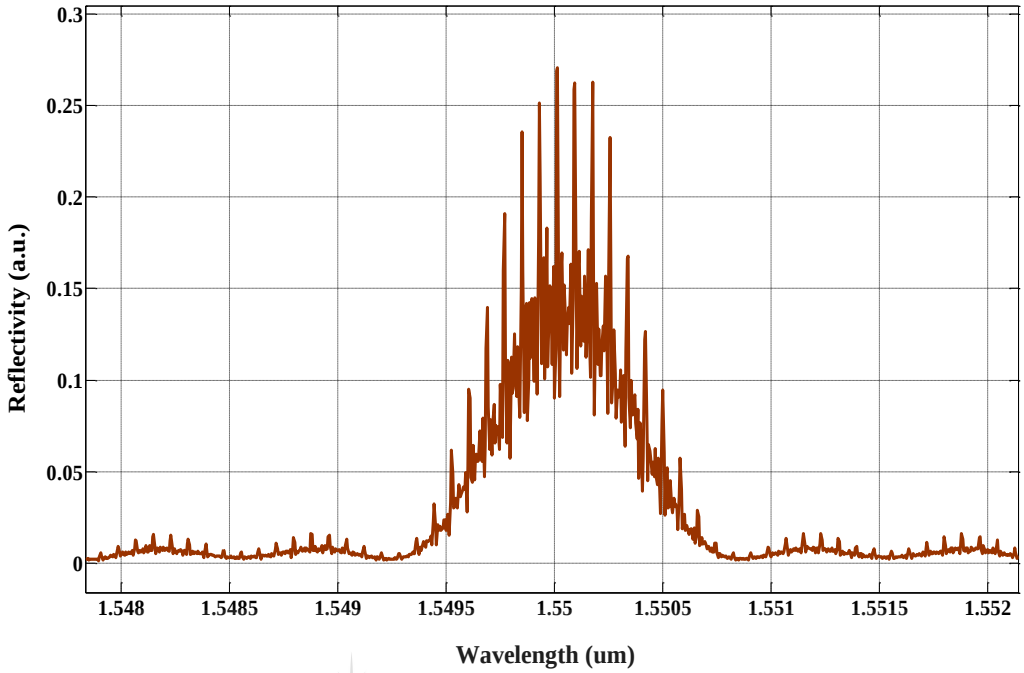

Figure 3-6. Total Reflected Spectrum of the F-P Sensor System Implemented in FDM.

The total reflected spectrum is captured at each temperature increment. The spectrum presented in Figure 3-6 is fast Fourier transformed to yield the triangles shapes presented in Figure 3-7.

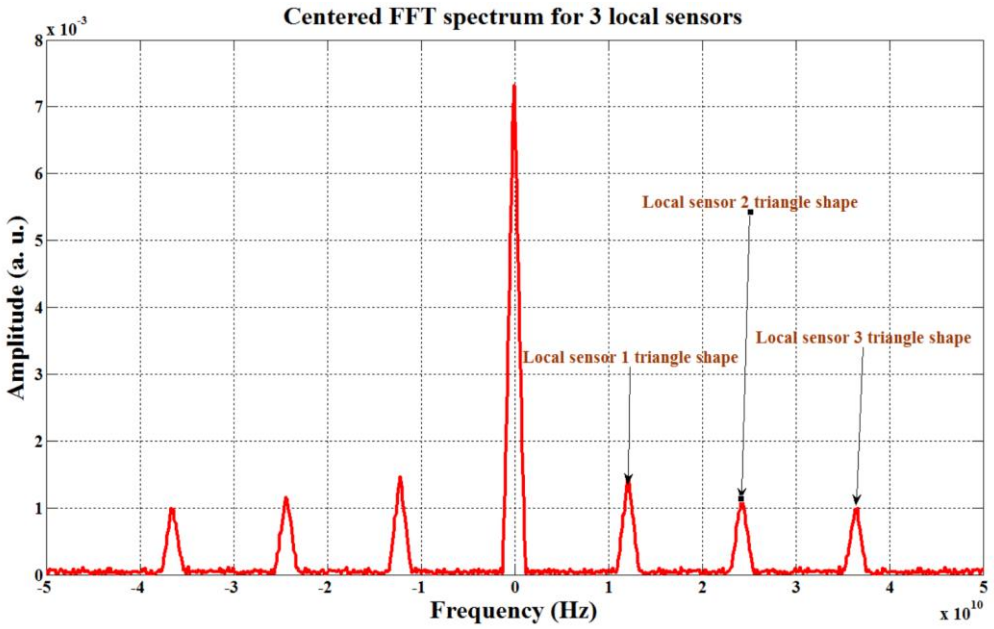

Figure 3-7. Centered FFT spectrum of the FDM system of 3 local sensors.

Using our demodulation algorithm, the calculated phase response to temperature changes at each respective local sensor from the simulation is presented in Figure 3-8.

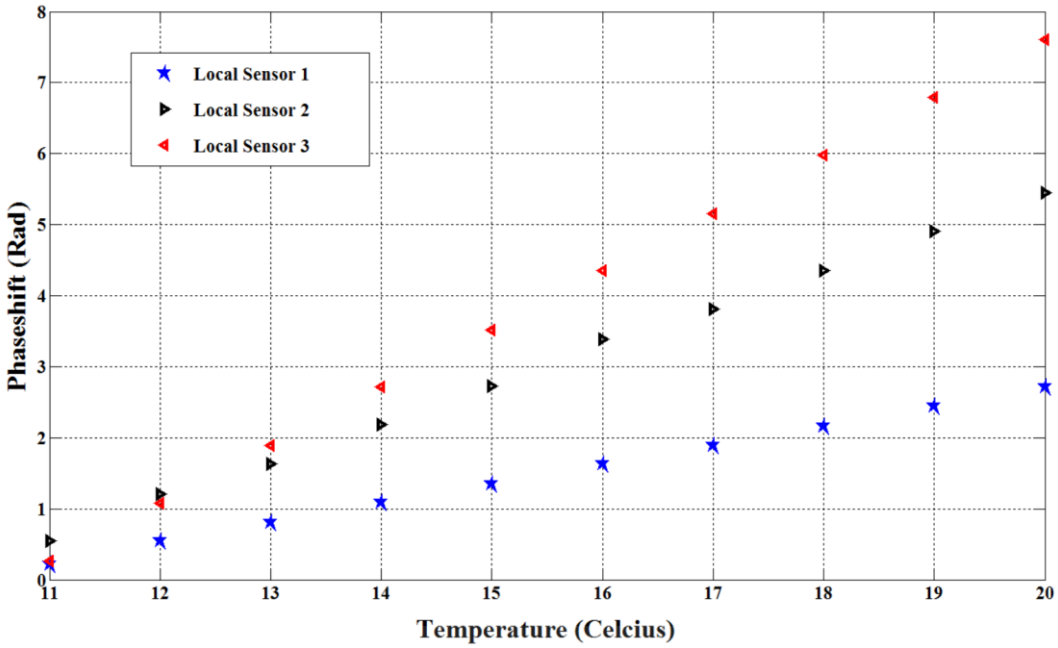

Figure 3-8. Responses of the simulation of the 3 local sensors simultaneously affected.

Figure 3-8 is made up of 3 graphs representing the phase responding to temperature changes in the interrogated sensors. As presented in the figure, the graphs in blue, black and red represent the phase responses of the 1st local sensor with 1 cm cavity length, 2nd local sensor with 2 cm cavity length and the 3rd local sensor with 3 cm cavity length. All local sensors phase responses to temperature are linear. A 2π cross over of 6℃ is observed respectively observed on the plot for the first local sensor, 3℃ for the second and 1.5 ℃ for the third sensor.

The WDM sensor system is composed of 3 F-P local sensors. Each F-P local sensor is composed of a two identical gratings of weak-reflectivity (1%) and identical Bragg wavelength (1550, 1555 nm and 1560 nm) separated by a cavity. The cavity lengths are respectively 1 cm for the first local sensor, 2 cm for the second local sensor and 3 cm for the third local sensor. The optical setup of the WDM F-P fibre sensor is presented in Figure 3-9.

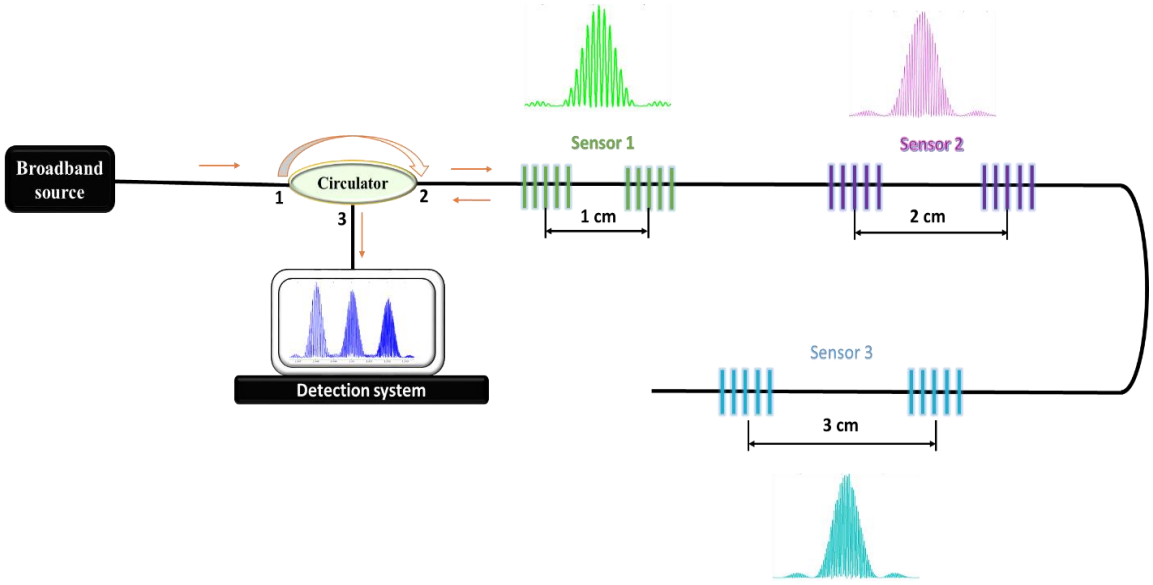

Figure 3-9. Optical Setup of the Multi-point F-P Fibre Sensor System Implemented in a WDM.

The optical setup represented in Figure 3-9 is also illustrated by Equation 3-2. A white noise having a Gaussian distribution with a standard deviation of $\sigma = 0.1$ is added to the phase of Equation 3-2. This equation is simulated in the same condition as in previous simulations.

The total reflected spectrum captured on the detection system is the sum of the interference pattern from each respective F-P local sensor and is centred at each respective Bragg wavelength respectively. Temperature changes are applied to Equation 3-2 with an increment of 1℃. The system is calibrated to 10℃ and data is captured from 11℃ to 30℃ as similar to the FDM setup in Figure 3-9. The total reflected spectrum of the WDM is presented in Figure 3-10.

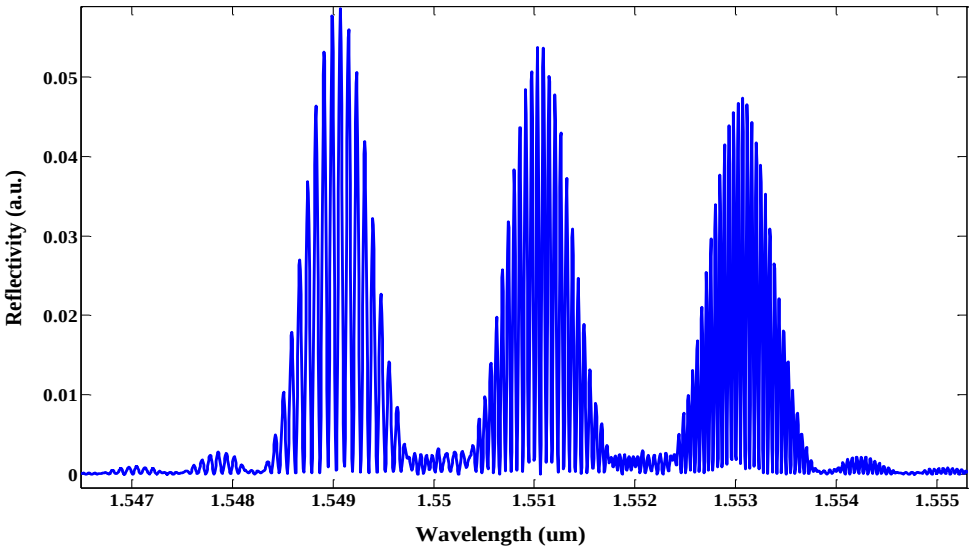

Figure 3-10. Total Reflected Spectrum of the F-P Sensor System Implemented in WDM.

Using the demodulation algorithm presented by Miridinov *et al*., the interrogated sensors' performances are evaluated. This simulation is not aimed at testing the performance of the sensor system. The clear meaning of the above section is to prove a point that the multi-point sensor system can be multiplexed in WDM and FDM. Using the same algorithm similar to the FDM the sensors should be interrogated identically leading to the combined sensor system presented in chapter 4.

3.4. Demodulation Algorithm

3.4.1. Demodulation of a Local Sensor

This section presents the algorithm whereby temperature changes in a local sensor is evaluated. It is understood that temperature variation in a local sensor causes a shift of its reflected interference pattern in the wavelength domain. The demodulation algorithm used in this project is based on Fourier transform (FT) shift analysis. Variations in the reflected interference in wavelength domain induce changes in phase in Fourier domain. By evaluating changes in phase, temperature changes can be monitored.

Fast Fourier transform (FFT) is applied to the spectrum captured in wavelength domain. By applying the FFT, the resulting spectrum is presented in the form of triangle shapes (S. V. Miridonov *et al*., 2001). The triangle shapes result from the convolution of the envelop function and the interference pattern, as graphically derived and shown in Figure 3-11.

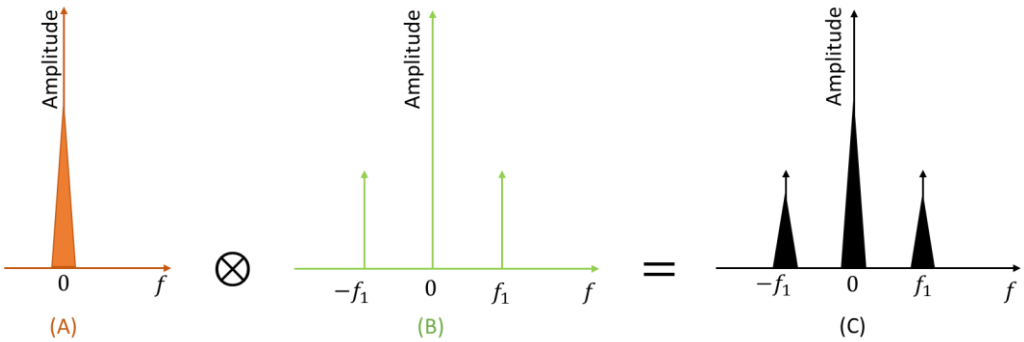

Figure 3-11. Triangle Shapes Transformation.

The FT of a constant is known as a δ-function centred at the origin. The FT of a cosine function produces two δ-functions, one centred at the frequency of the cosine function and the other mirrored to the left side of the origin. The FT of $\frac{\Omega^2 sinh^2(sL)}{\Delta\beta^2 sinh^2(sL)+s^2 cosh^2(sL)}$ yields a triangle function. Therefore, the convolution in Fourier domain of the grating and the cosine function creates the triangle shapes presented in Figure 3-11 (C). From Figure 3-11 (C), the amplitude of the Fourier component at 0 frequency is offset of the signal, and the triangle shape at the left ($-f_1$) is a mirror image of the one at the right (f_1), which is the signal of the sensor in Fourier domain. One of the characteristics of the triangle shape is its spectral width.

The spectral width is a function of the Bragg wavelength and the refractive index of the fibre in Fourier domain, as presented (M. G. Shlyagin *et al*., 1997):

$$\Delta f_{BG} = \frac{4nL_{BG}}{\lambda_{BG}^2}; \qquad (3-3)$$

In the demodulation algorithm, the FT is made up of samples. In this sense, the local sensor's triangle shape is also constituted with few samples having a band-width as defined by Equation 3-3. The band-width of the triangles shapes is limited in both sides by a minimum and a maximum frequency. These respective frequencies are represented by Equation 3-4 and Equation 3-5.

$$f_{max} = f + \frac{\Delta f_{BG}}{2} = \frac{2nL_{F-P}}{\lambda_{BG}^2} + \frac{2nL_{BG}}{\lambda_{BG}^2} = \frac{2n(L_{F-P}+L_{BG})}{\lambda_{BG}^2}; \qquad (3-4)$$

$$f_{min} = f - \frac{\Delta f_{BG}}{2} = \frac{2nL_{F-P}}{\lambda_{BG}^2} - \frac{2nL_{BG}}{\lambda_{BG}^2} = \frac{2n(L_{F-P}-L_{BG})}{\lambda_{BG}^2}; \qquad (3-5)$$

where: f is the frequency of the interference pattern of the local sensor, Δf_{BG} is the spectral bandwidth, f_{max} is the local sensor maximum frequency and f_{min} is the local sensor minimum frequency in the triangle shape.

For proper demodulation, the Nyquist theorem is applied to sample the signal in frequency domain, in order to recover the information kept inside the local sensor (Miridonov *et al*., 2001). Including the Nyquist theorem, the sampling frequency is presented as follows:

$$f_m \geq \frac{2 \times 2n\left(L_{BG} + L_{(F-P)}\right)}{\lambda_{BG}^2}; \qquad (3-6)$$

where: f_m is the sampling frequency.

When the signal is calibrated, the captured spectrum presented in Equation 3-1 is now represented by $R_{F-P}(f)$. At this point we consider that no disturbance has been applied to the local sensor. When disturbance is applied, the captured spectrum is represented by $R'_{F-P}(f)$. The evaluation of the disturbance is done by calculating the relative phase shift between the calibrated reference spectrum and the instantaneous measured spectrum. If there is no disturbance in the sensor after calibration, the relative phase difference is zero. The calculation of the relative phase is presented as:

$$\emptyset_m = \arg[R'_{F-P}(f)R^*_{F-P}(f)]; \qquad (3-7)$$

where: $R^*_{F-P}(f)$ is the complex conjugate of the calibrated spectrum of the local sensor and $\emptyset_m$ is the relative phase as function of samples in Fourier domain.

After the calculation of the relative phase, a 2π problem experienced by interferometric fibre sensors needs to be addressed. This is because interferometric fibre sensors give the same values for phases, which differ by multiples of 2π and are known as the ambiguity (Miridonov *et al*., 2001). This ambiguity is caused by the cosine function presented in Equation 3-1, generally common to interferometric sensors. As temperature varies, it affects all the sensors. Using linear regression, the ambiguity can be measured.

The layout of the triangle shapes is completely in line with the explanation provided in Figure 3-11 and therefore overlaps with the literature.

The phases of all samples inside the triangle shapes are plotted against the sample number and are approximated by a straight line (F. Shen and A. Wang, 2005). The linear fit is presented in Figure 3-12.

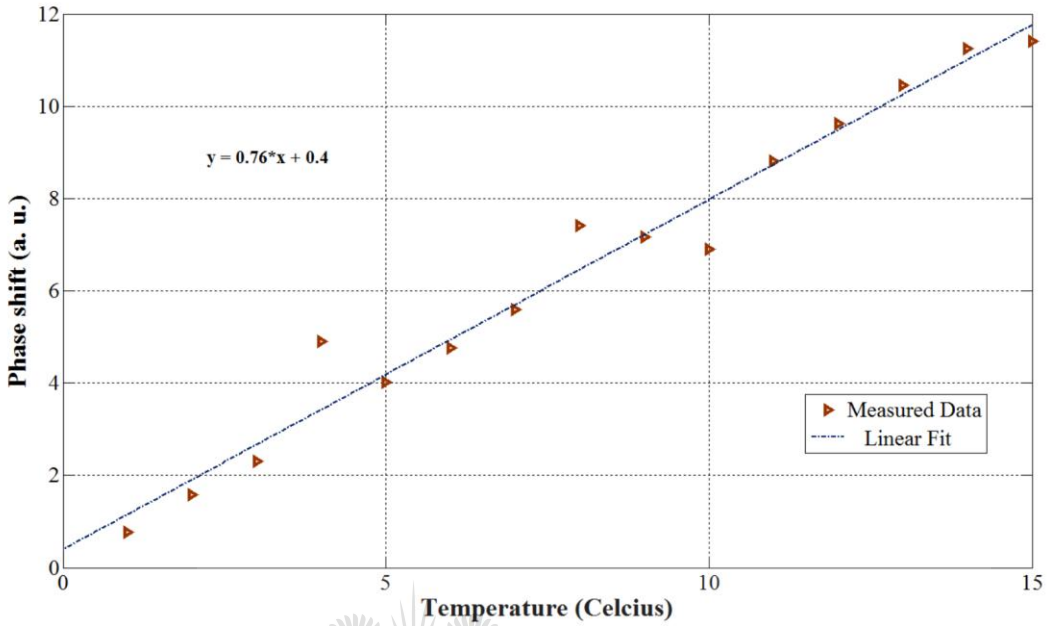

Figure 3-12. Linear Regression Approximation.

The coefficients of the linear fit are used to calculate the total phase shift as follows:

$$\emptyset_{Relative} = Aj + B; \qquad (3-8)$$

where: A and B are the coefficients of the linear equation and j is the sample (Miridonov *et al*., 1998). The ambiguity M is given by:

$$M = floor\left(\frac{B}{2\pi}\right), \qquad (3-9)$$

Knowing the relative phase and the ambiguity gives the possibility to evaluate the total phase shift induced by the applied temperature.

$$\emptyset_{Abs} = \emptyset_{Relatve} + 2\pi M; \qquad (3-10)$$

In this project, the demodulation algorithm is summarised in the flow chat presented in Figure 3-13.

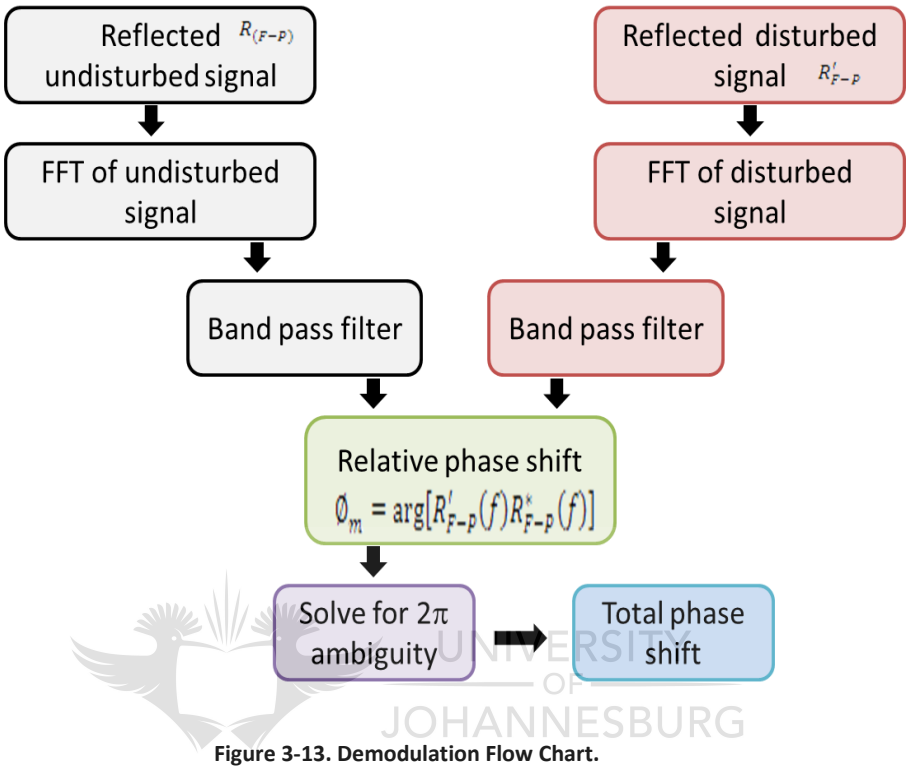

Figure 3-13. Demodulation Flow Chart.

3.4.2. Demodulation of the Multi-point Fibre Sensor System

In the multi-point fibre sensor system, the total reflected spectrum captured on the detection system is Fourier transformed. The Fourier transform (FT) spectrum is presented in the form of multiple triangle shapes where each triangle shape located at the right hand side of the frequency zero represents the respective local sensors information. Each local sensor is centred on its respective interference pattern frequency, represented by:

$$f_j = \frac{2nL_{(F-P)_j}}{\lambda^2_{BG_j}}; \qquad (3-11)$$

where: f_j represents the frequency of the j^{th} local sensor, λ_{BG_j}represents the Bragg wavelength of the j^{th} local sensor and $L_{(F-P)_j}$ represents the cavity length of the j^{th} local sensor.

The frequency band-width of each respective local sensor is represented as:

$$\Delta f_{BG_j} = \frac{4nL_{BG_j}}{\lambda_{BG_j}^2}; \qquad (3-12)$$

where: L_{BG_j} represents the Bragg grating length of the j^{th}local sensor.

Equation 3-12 clearly shows that in the FDM configuration, all the local sensors have identical bandwidth while in the WDM, the bandwidth are different from one local sensor to the other.

The triangle shapes, containing the information of each respective local sensor in Fourier domain has a bandwidth made of few samples of different amplitude. This bandwidth is limited on both sides by the minimum frequency (sample number 1) and the maximum frequency (sample number *j*) as presented in the Equations 3-4 and 3-5.

Equation 3-7 is used to discretely calculate the relative phase induced by temperature changes. It is calculated at each sample within the broadband. Because the information confined in the triangle shapes are made of few samples, linear regression is used to have the best approximation of the phase in each respective local sensor. The total phase is then calculated thereafter using Equation 3-10.

The benefits associated with this demodulation algorithm to evaluate temperature changes is that each respective local sensor can be interrogated distinctively using the flow chart presented in Figure 3-13.

3.5. Characteristics of the Multi-point Fibre Sensor

The characteristics of the multi-point sensor system present the range whereby, the sensor works perfectly. The idea in this section is to present some restrictions on the minimum and maximum cavity length, the separation between consecutive local sensors and the difference in length between 2 consecutive local cavities.

The minimum length of the F-P cavity is the limitation on the separation between the two identical gratings, wherein the interference pattern of local sensor can still be recovered for proper demodulation. The spectral width of the grating and the frequency of the interference of the local sensor are very important parameters used to size the minimum cavity length.

On the other hand, the maximum cavity length of the local sensor is the acceptable length whereby the interference pattern fringes can still be resolved by the detection system for proper demodulation. This is because the separation of the fringes in F-P interferometer is a function of the cavity length. The minimum separation of the fringes depends on the resolution of the detection system. Therefore, if the resolution of the detection system is not enough to separate the fringes, information is lost.

The separation between local sensors should be carefully designed to avoid confusion in the demodulation. In the multi-point sensor systems, the rule of thumb says that the minimum separation between 2 local sensors should be bigger than the largest cavity length on the system.

The minimum difference in length between local sensors had to be established to prevent an overlap when the Fourier analysis is performed. In order to avoid such an overlap, the local sensors' cavity in multi-point sensor systems must be properly designed.

From the theory, these characteristics have been defined by (M. G. Shlyagin *et al.*, 2002; S.V. Miridonov *et al.*, 2001; M. G. Shlyagin *et al.*, 1997) and presented in Table 3-1.

Designation	Formula
Minimum cavity length	$L_{(F-P)_{min_j}} \geq 2L_{BG_j}$
Maximum cavity length	$L_{(F-P)_{max}} \leq \frac{\lambda_{BG}^2}{4nF}$
Minimum difference in length between local sensors	$L_{(F-P)_j} - L_{(F-P)_{j-1}} \geq 2L_{BG}$
Separation between local cavities	$L_{(minimal\ length)} > \frac{\lambda_{BG}^2}{4nF}$

Table 3-1. Multi-point fiber sensor characteristics.

Experiments through simulation are performed to quantify their impact on the multi-point sensor system. To give a full illustration of the information presented in Table 3-1, a sensor system made of a minimum F-P cavity length is designed and simulated. In this simulation, the

gratings have their Bragg wavelength at 1550 nm and a 1 mm length. The separation between them is kept to 1 mm. A white noise having a Gaussian profile is added to the phase of the F-P local sensor as presented in Equation 3-1. Their captured spectrums, including the calibrated reference and the instantaneous change, are respectively presented in Figure 3-14.

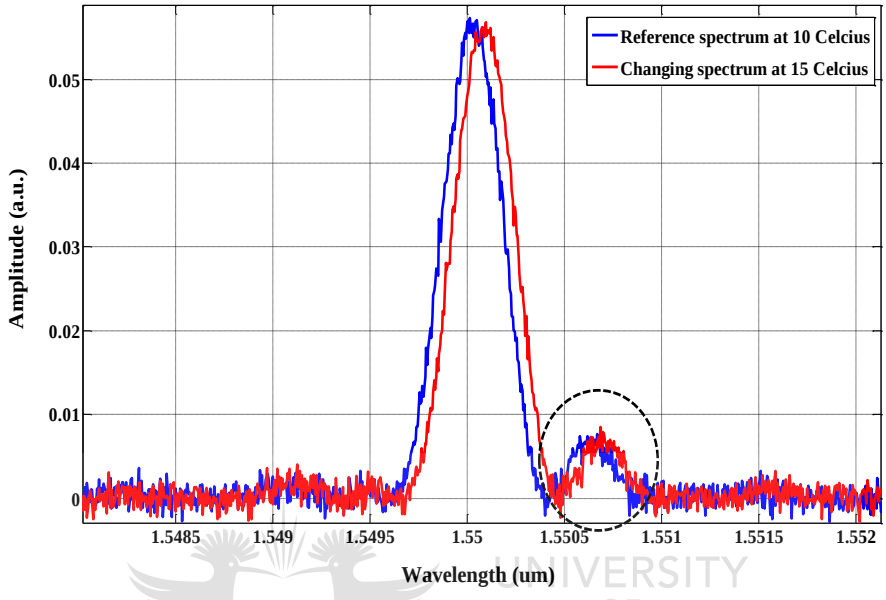

Figure 3-14. F-P Unaccepted Minimum Cavity Length.

The above spectrums in red and blue consist of a main peak and a side right lobe, which can be described as low interference pattern. Using these spectrums should yield and correct information retrieved by the demodulation.

To illustrate the maximum cavity length, another simulation is performed using a cavity length of 1 m, with identical gratings of 1550 nm wavelength and 1 mm length. The reflected spectrum is presented in Figure 3-15 where the system is calibrated to 10℃ and the measurement to 15℃.

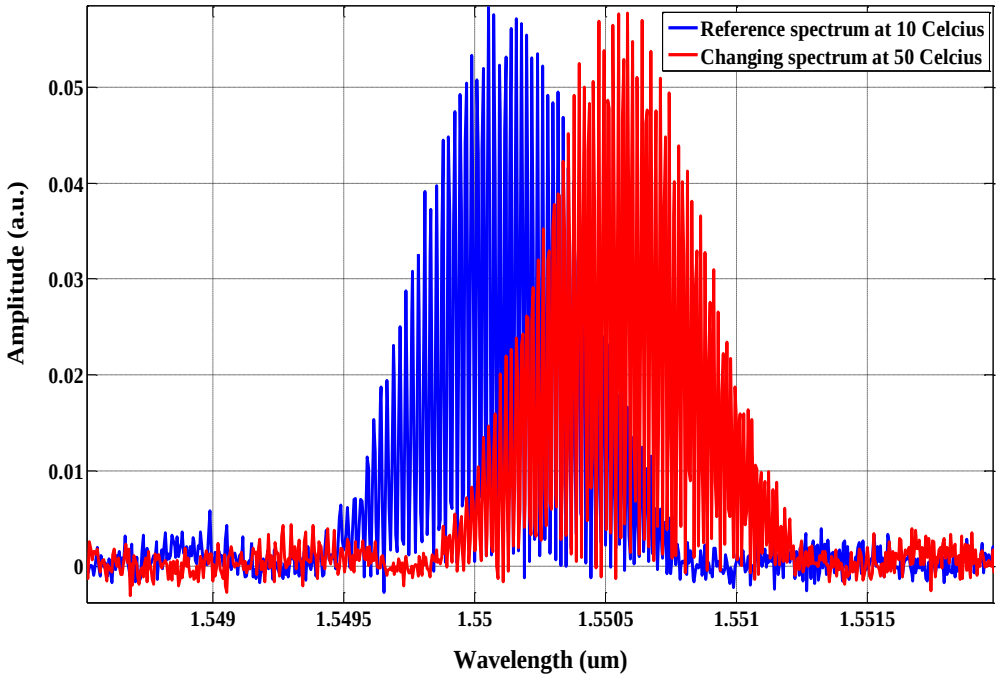

Figure 3-15. F-P Unaccepted Maximum Cavity Length.

The spectrum in blue is calibrated, while the spectrum in red is the instantaneous changing temperature. As can be seen, the resolution of the detection system is too low, it is therefore impossible to resolve the interference pattern using the OSA in our facility.

3.5.1. Cross-talk Analysis of the Multiplexed Sensing System

In a multi-point F-P sensor system implemented in series, cross-talk originates from reflectance of any of the two mirrors which influence the readings of the sensor's array. The analysis of the cross-talks in this sensor system yields an important task in lowering their effects in the demodulation. Since any two mirrors interact with the incident light, the reflectance and the transmittance of the j^{th} local sensor are respectively represented by R_j and T_j. The transmittance of the j^{th} local sensor is represented by:

$$T_j = (1 - R_j)\alpha_j; \qquad (3-13)$$

where: represents the power loss or attenuation in the fibre.

If we consider an incident power source having a low attenuation, the power that reaches the j^{th} sensor in the system is described as (F. Shen, 2006):

$$P_j = P_0 R_j \prod_{i=1}^{j-1} T_i^2 = P_0 R_j \prod_{i=1}^{j-1} \alpha_i^2 (1 - R_i)^2 \; ; \qquad (3-14)$$

where: P_0 is the initial power in the fibre, T_i^2 is the i^{th} local sensor's round-trip transmittance of the j^{th} local sensor. At low reflectivity, Equation 3-14 can be approximated as (F. Shen, 2006):

$$P_j \approx P_0 R_j \left(1 - 2\sum_{i=1}^{j-1} R_i\right) \prod_{i=1}^{j-1} \eta_i^2 \; ; \qquad (3-15)$$

It is apparent that the signal of the j^{th} local sensor is affected by the attenuation and the reflectance of the $j^{th} - 1$ sensors before it. Because the attenuation of the SMF-28 is very low, we can assume that $\prod_{i=1}^{j-1} \eta_i^2 = 1$. The power of the j^{th} local sensor is be normalised as (F. Shen, 2006):

$$\frac{P_j}{P_0} = R_j \left(1 - 2\sum_{i=1}^{j-1} R_i\right) = R_j - 2R_j \sum_{i=1}^{j-1} R_i \; ; \qquad (3-16)$$

where: R_j is the reflection from the j^{th} sensor, while $2R_j \sum_{i=1}^{j-1} R_i$ is the cross-talk by:

$$r_{Cross-Talk\,j} = 2\sum_{i=1}^{j-1} R_i \; ; \qquad (3-17)$$

Furthermore, it is important to state that using the super luminescent emitting diode (SLED) as optical source, its coherence length is shorter as compared to that of a diode laser. Using weak reflectivity gratings as reflectors in the local sensors, minimizes the impact of the cross-talks as well. Therefore, in the multi-point sensor systems presented in this project, the cross-talk is very low. This is due to the low attenuation of the SMF in the 1550 nm region and the low losses related to the low-reflectivity of the identical-gratings and then to the coherence length of the broadband source. Therefore, $r_{Cross-Talk_j}$ is negligible and their effects on the sensor system are limited.

3.6. Investigation of the Response of 2 Local Sensors When They Overlap in Fourier Analysis

This section is aimed at investigating how much the magnitude of the overlap in Fourier analysis affects the performance of the sensor. The optical setup is shown in Figure 3-16.

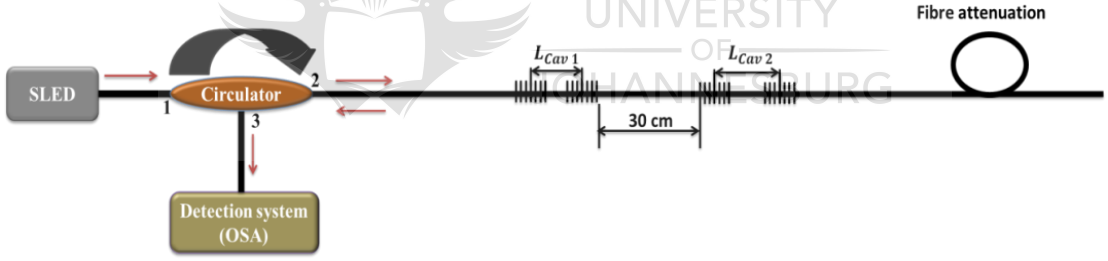

Figure 3-16. Optical Setup of the Overlap Simulation with Two Local Sensors Investigated.

In the simulations three different cases are investigated where the spectrums of the triangle shape representing local sensor 1 and that of local sensor 2 move towards each other such as 25%, 50% and 75 %. In this simulation, all the gratings are identical in their respective Bragg wavelength (1550 nm), and weak reflectivity. The separation between the two F-P local sensors is kept to 30 cm as shown if Figure 3-16. A temperature increment of 1℃ is applied to local sensor 1 from 13℃ to 41℃, while keeping sensor 2 at constant temperature.

From theory, the difference between the two local sensors should be at least bigger than 2 mm after calculations as shown in Table 3-1 due to the length of the grating used in the simulation. In this simulation, the cavity length of the F-P local sensor 1 is 1.825 cm, while that of local

sensor 2 is to 2 cm. In this setup, the difference in length from the cavity length on and cavity length two is $L_{F-P_2} - L_{F-P_1} = 2\ cm - 1.825\ cm = 1.75\ mm$, marginally less than 2 mm (recall Figure 3-14).

In this simulation, the system is calibrated and temperature changes are applied to local sensor 1. The total reflected spectrum is Fourier transformed using our demodulation algorithm. On the spectrum in Fourier domain, it is observed that the triangle shape of local sensor 2 has shifted to into that of the second local sensor 1 of about 25%. This spectrum is schematically presented in Figure 3-17.

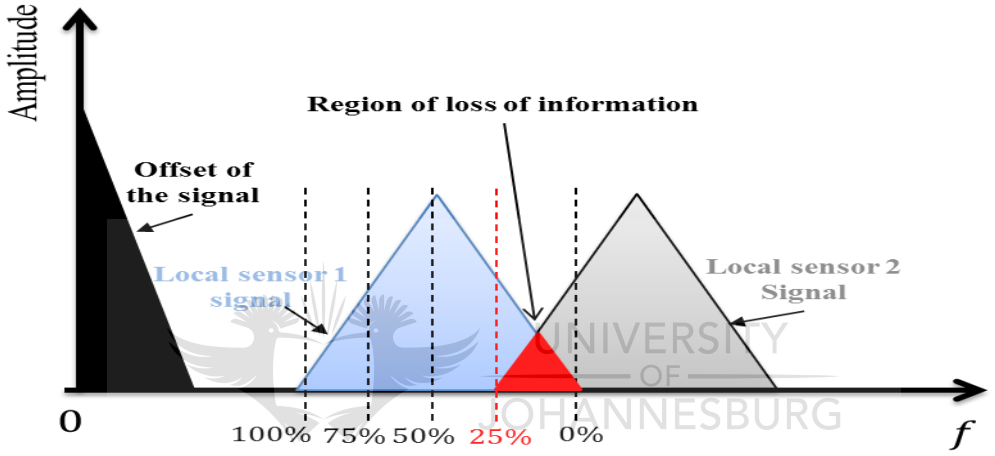

Figure 3-17. Intrusion of the triangle shape of local sensor 2 into that of local sensor 1 of about 25%.

The region whereby the two local sensors cross into each other of about 25 % as shown on Figure 3-17 is an area of loss of information which impacts on the sensor performance.

Using algorithm presented in this project, the spectrums from the simulation of the sensor system made of 2 local sensors having 1.825 cm cavity length for the local sensor 1 and 2 cm cavity length for local sensor 2 are presented in Figure 3-18.

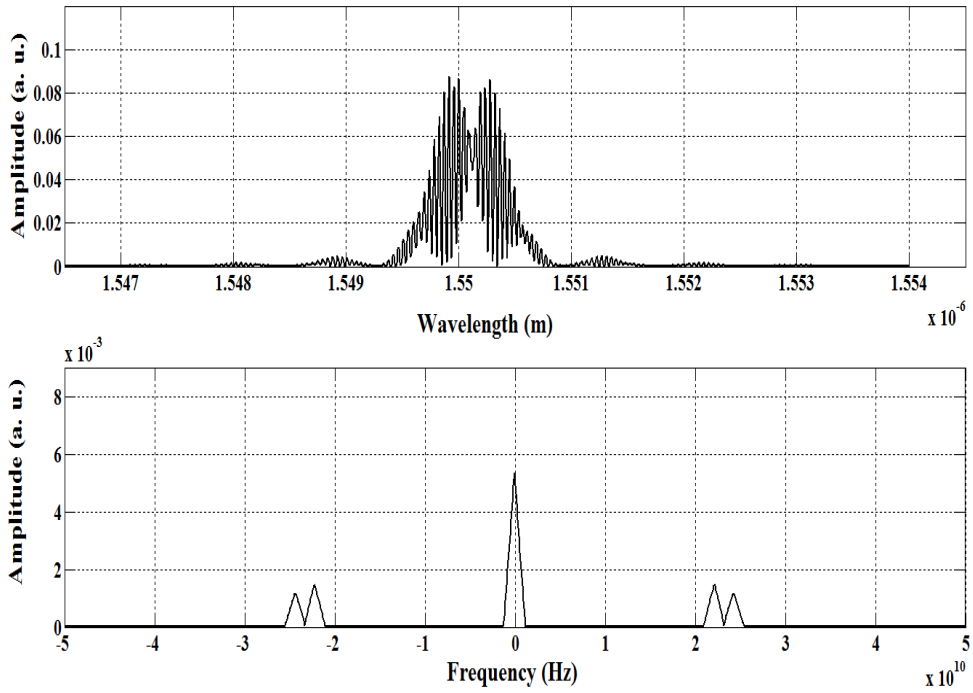

Figure 3-18. Simulated spectrum of the sensor system with 1.825 cm cavity length for Local sensor 1.

After applying our demodulation algorithm, the response of the local sensor 1 with respect to temperature changes is presented in Figure 3-19.

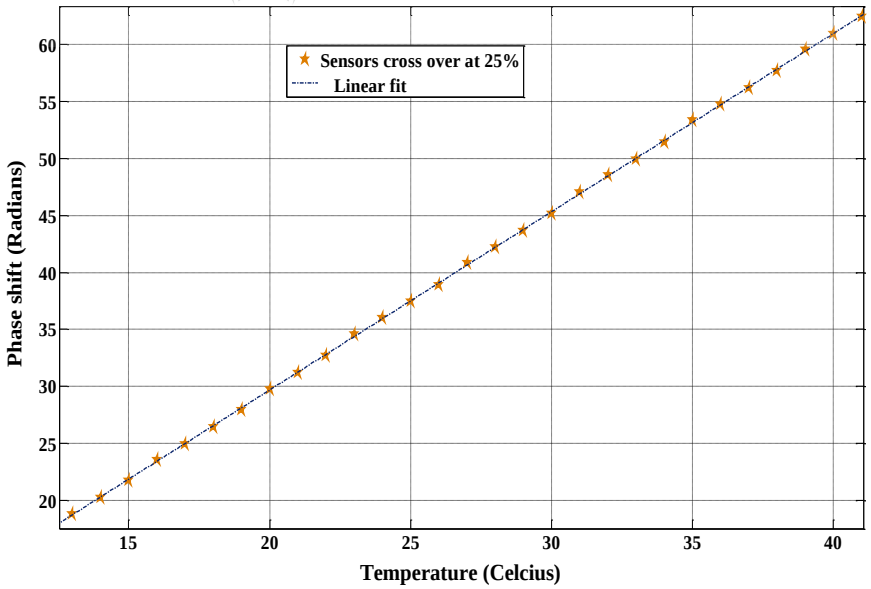

Figure 3-19. Phase Response to Temperature of the 25 % Overlap.

Figure 3-18 is a representation of the change in phase shift, with respect to temperature changes of the interrogated local sensor 1 having the cavity length of 1.825 cm in brown while the

dashed line represents the linear fit. The response is a linear. The loss of information of about 25 % does not affect the sensitivity of the sensor too much as shown.

In the other simulation, the cavity length of local sensor 1 is 1.875 cm instead of 1.825 cm than earlier while that of the second local sensor is still 2 cm. The sensor system is still made of two local sensors separated by 30 cm from each other. Temperature changes are applied to local sensor 1 from 13℃ to 41℃ while local sensor 2 is kept at constant temperature. After calibration and temperature changes, the spectrum captured are Fourier transformed.

In Fourier domain, it is observed that, as the cavity length of local sensor 1 increases from 1.825 cm up to 1.875 cm, so does the region of loss of information. Now the difference in the cavity length of local sensor 2 and that of local sensor 1 is $L_{F-P_2} - L_{F-P_1} = 2\,cm - 1.875\,cm = 1.25\,mm$. The impact of the triangle shape of local sensor 1 and local sensor 2 moving towards each other increases to 50%. The spectrum of the sensor system in Fourier domain is schematically presented in Figure 3-20.

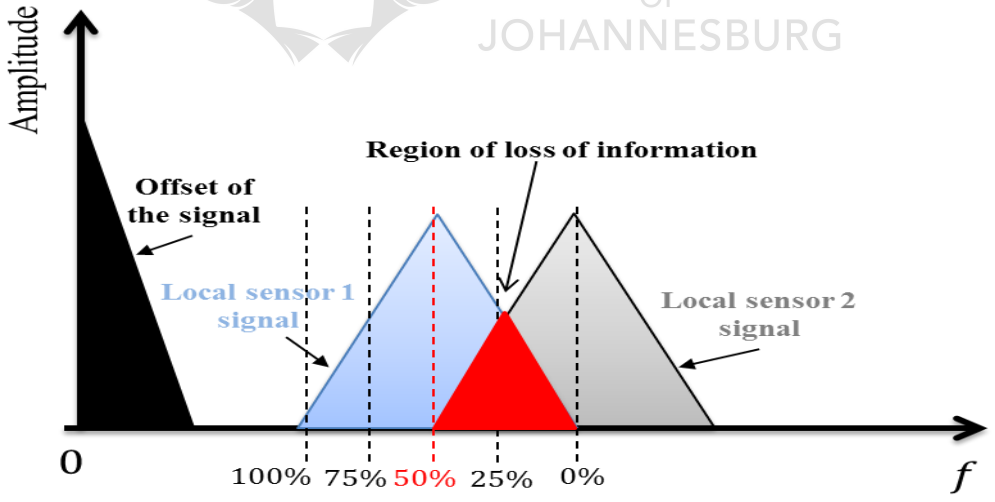

Figure 3-20. Intrusion of the triangle shape of local sensor 2 into that of local sensor 1 of about 50%.

Similarly to the above, the simulated spectrums of the sensor system having a 50 % loss of information and the 1.875 cm cavity length for the second local sensor is presented in Figure 3-21.

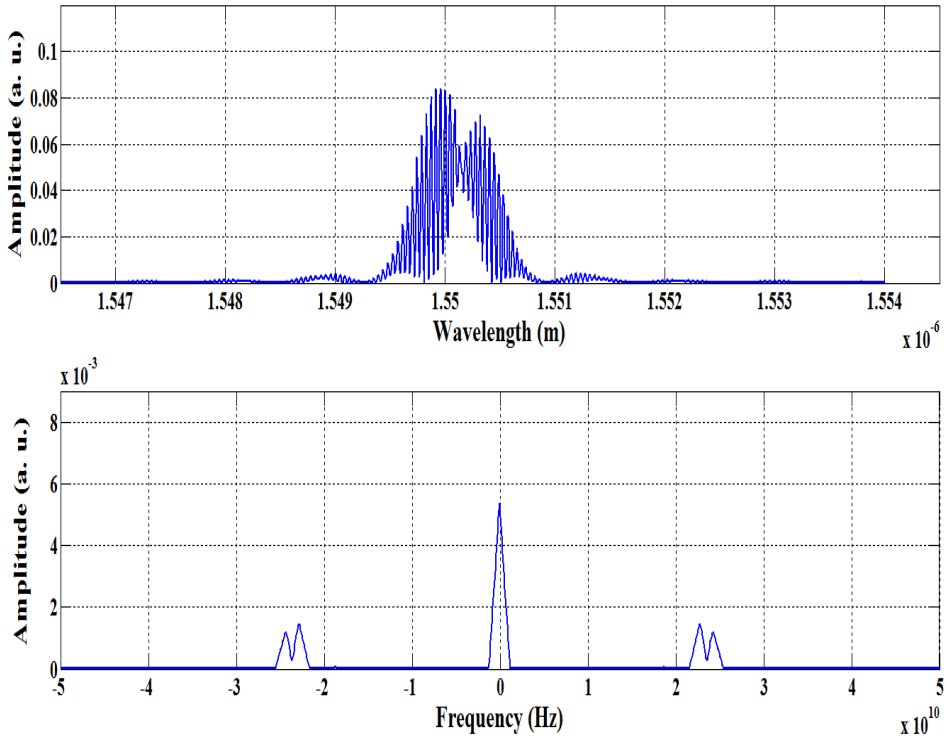

Figure 3-21. Simulated spectrum of the sensor system with 1.875 cm cavity length for Local sensor 1.

Applying our demodulation algorithm, the phase response of the local sensor 1 having 1.875 cm cavity length with respect to temperature changes is presented in Figure 3-22.

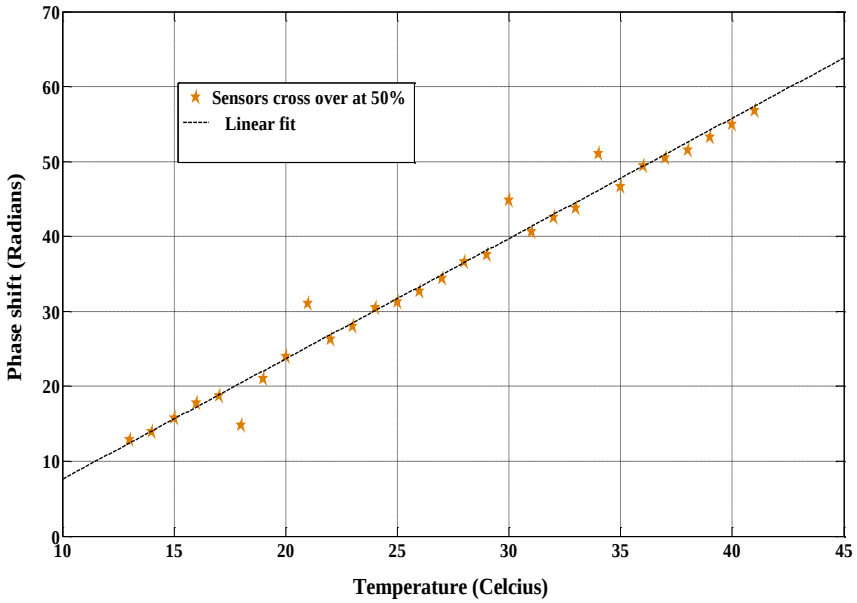

Figure 3-22. Phase response to temperature of the 50 % overlap.

The graph in brown represents the response of the sensor 1 under investigation having 1.875 cm cavity length with respect to temperature changes. The dashed line in grey represents the polynomial fit. This clearly shows that the sensor response to temperature is no longer linear as expected due to the influence of the samples in the triangle shape from sensor 2 that attach themselves with those from local sensor 1.

In this last investigation, the cavity length of local sensor 1 is designed to be 1.925 cm, keeping the other conditions similar to those previously discussed. In this simulation, we have two local sensors separated from one another by 30 cm. In this simulation, temperature changes are applied to local sensor 1 as previous at an increment of 1℃ from 13℃ to 41℃. Now the difference in the cavity length of local sensor 2 and that of local sensor 1 is $L_{F-P_2} - L_{F-P_1} = 2\ cm - 1.925\ cm = 0.75\ mm$. Having 0.75 mm length in difference increases the rapprochement between them to 75 % in Fourier domain. The 75 % overlap is schematically presented in Figure 3-23 in frequency domain.

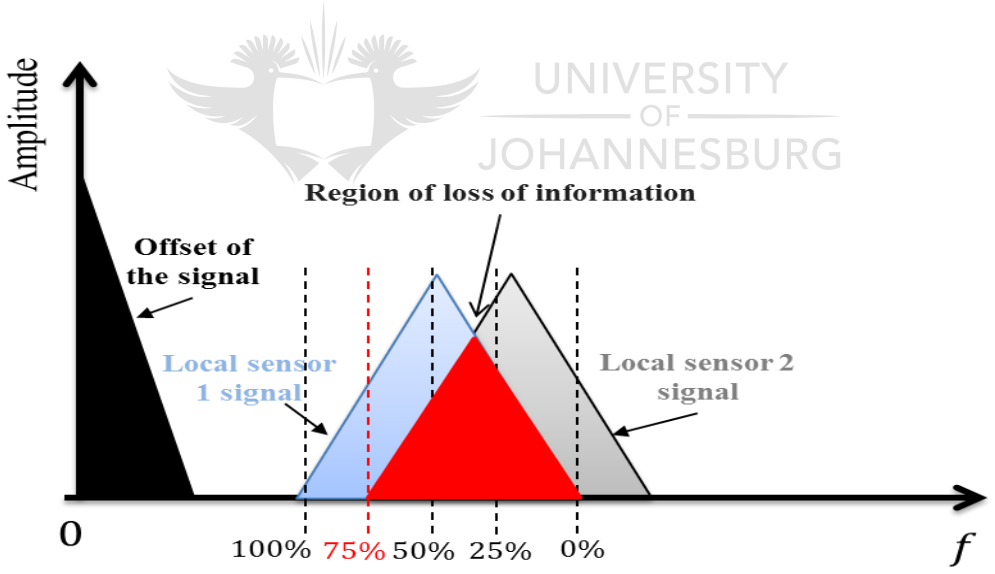

Figure 3-23. Intrusion of the triangle shape of local sensor 2 into that of local sensor 1 of about 75%.

For a sensor system where the loss of information is around 75 %, the spectrums of the simulated system with 1.925 cm as the cavity length of local sensor 1 is presented in Figure 3-24.

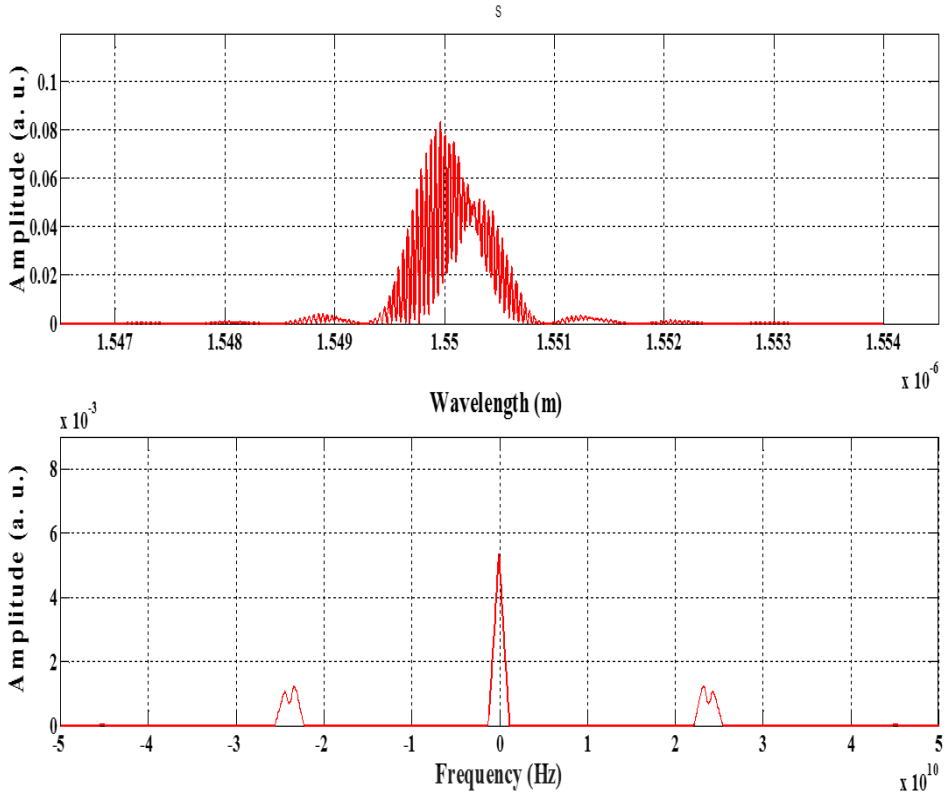

Figure 3-24. Simulated spectrum of the sensor system with 1.925 cm cavity length for Local sensor 1.

The phase response to temperature changes of the local sensor 1 having 1.9 cm cavity length is presented in Figure 3-25.

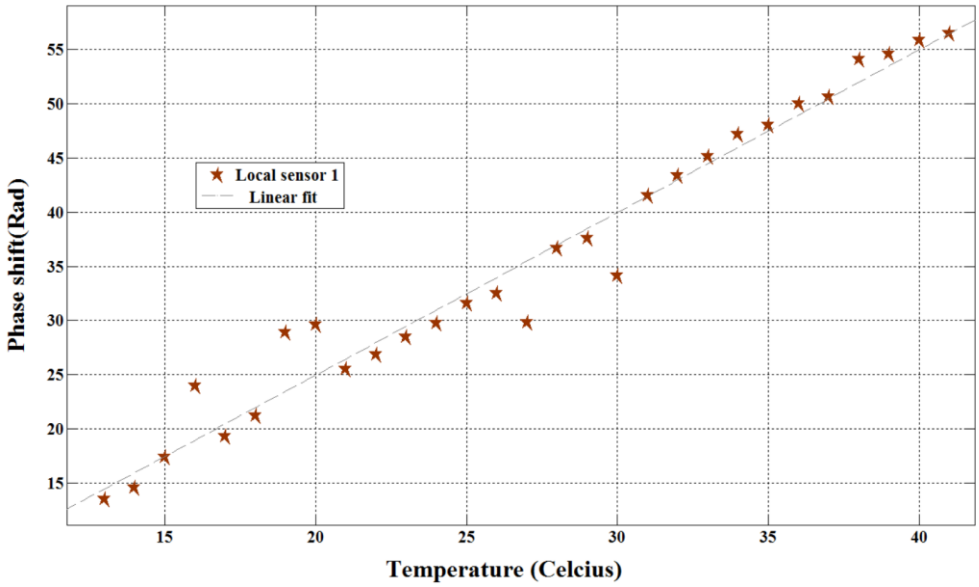

Figure 3-25. Phase Response to Temperature of the 75 % Overlap.

Figure 3-22 shows the behaviour of the sensor system when the triangle shapes of local sensor 1 and local sensor 2 move towards each other of about 75 % in Fourier domain. As shown, local sensor 1 phase response to temperature changes is represented by the brown plot while a polynomial fit is represented by the dashed grey plot. The dashed line in grey is the linear fit. This also clearly shows that the local sensor 1 does not respond to temperature linearly anymore.

Taking a deep look into the above three simulations, it is very important to understand how the overlaps impact on the sensor spectrums and therefore on the accuracy of the sensor system. It can be observed on the Figures, 3-18, 3-21 and 3-24 that, the wavelength spectrums are distorted which yield overlapping triangle shapes when the fast Fourier transform is applied.

In normally designed sensor system simulated in the similar conditions as above, the spectrums of the local sensors having 1 cm cavity length for the local sensor 1 and 2 cm cavity length for the local sensor 2 is presented in Figure 3-26.

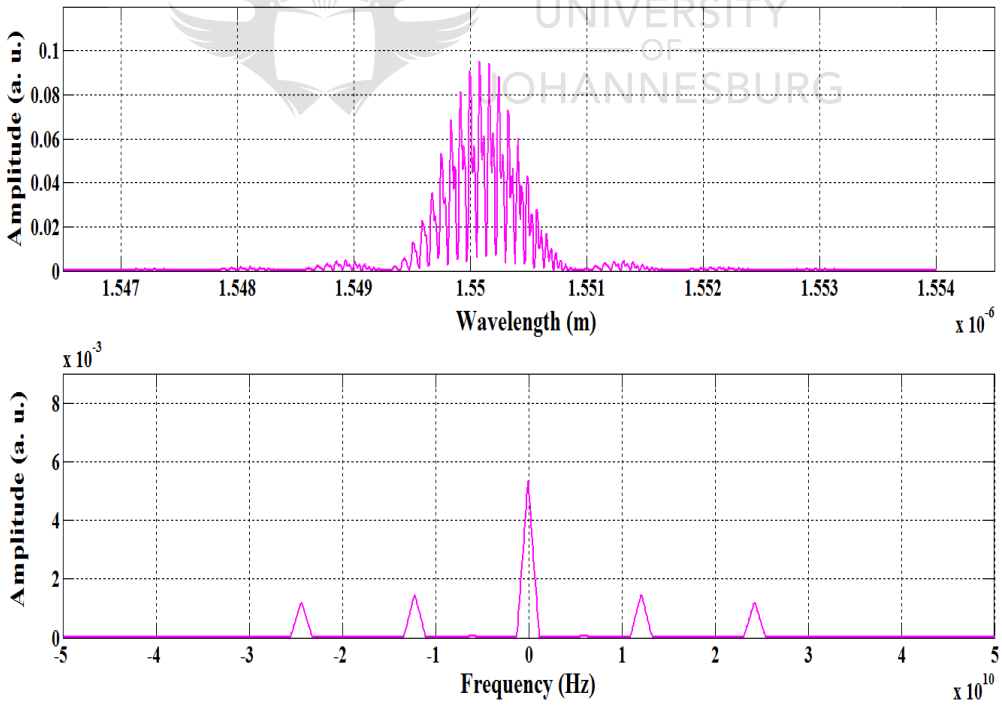

Figure 3-26. Simulated spectrum of the sensor system with 1 cm cavity length for Local sensor 1 and 2 cm for local sensor 2.

In order to provide a summary to the simulations presented in this section, the root mean square deviation (RMSD) is calculated with respect to the 3 overlap sensor systems simulated. This is

aimed at summarizing the trend in deviation of the measured phase shift as a function of the percentage of the overlap. This RMSD known as the sensor error with respect to phase shift is presented in Figure 3-27.

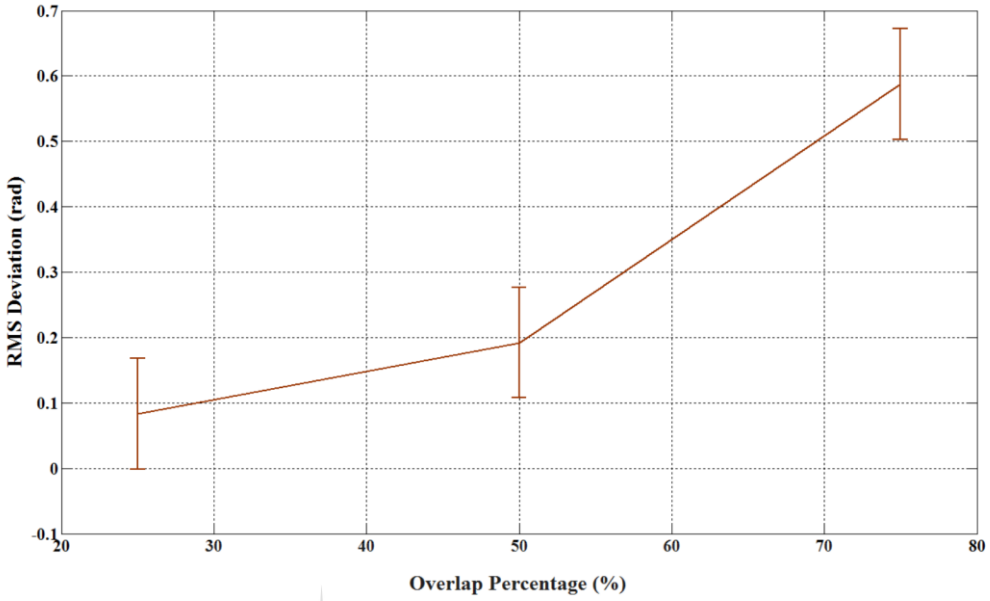

Figure 3-27. RMS Deviation error with respect to the overlap

A quick look at Figure 3-27 clearly confirms that the sensor error increases with the increase in the overlap. The RMSD calculated from the overlapped sensors simulated in this are respectively 0.02 rad, 0.06 rad and 0.187 rad as presented on the Figure 3-27.

3.7. Summary

The design and simulation results of the multi-point F-P fibre sensor system have been presented in this chapter, furthermore including the theoretical working principles and the demodulation algorithm. The simulated sensors' performances have been presented. These results are used as guide for the experimental work presented in Chapter 4.

4. Experimental Setup Description

4.1. Introduction

The experimental setup and the description of the multi-point temperature fibre sensor is presented in this chapter. The optical system is composed of 9 local sensors. Each local sensor is made of a F-P cavity formed by identical FBGs of weak reflectivity. The 9 local sensors (FBG based F-Ps) are imprinted in our facility at specific positions on a serial array in a combination of frequency division multiplexing (FDM) and wavelength division multiplexing (WDM) on the single mode fibre (SMF). In this sensor system, a heating system – such as thermal plate – is used to generate heat on the interrogated local sensors. For the purpose of the optical experiments, the thermal plates are characterized and calibrated.

The performance (sensitivity and resolution) of the multi-point sensor system presented in this chapter is tested. A further experimental test whereby two local sensors overlap in their Fourier domain is also presented in this chapter.

4.2. Thermal Plates Characterization

In order to use the thermal plates as heat generators in the sensor system, it is essential to characterize them. Therefore, a description, characterization and calibration of these thermal plates are presented in this section.

4.2.1. Thermal Plates

The thermal plates used in this project are resistive foil heaters having a $10\,K\Omega$ thermistor directly integrated into the plates and 4 terminals. Each thermistor is a negative temperature coefficient (NTC) thermistor which the resistance decreases when the temperature increases. The physical illustration of the thermal plate is shown in Figure 4-1.

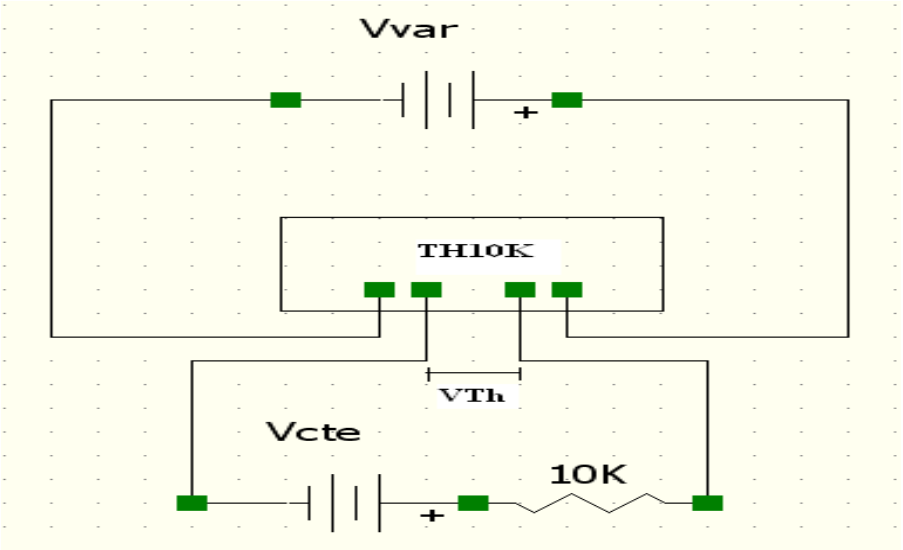

Figure 4-1. TH10K Schematic Layout.

As shown on the schematic layout in Figure 4-1, the two outer terminals are used to generate heat on the plate through the resistive foil heaters, and the two inner terminals used to monitor the temperature on the plate.

Power is applied (V_{var}) to the 2 outer terminals with a power supply (PS_1), while a second power supply (PS_2) is applied (V_{cte}) and connected in series to the thermistor and a 10 $k\Omega$ resistor. Because the resistance of the thermistor changes with temperature, the 10 $k\Omega$ resistor is aimed at achieving a voltage divider connected in series as shown. This is intended to monitor the voltage (V_{Th}) and the resistance at the thermistor.

4.2.2. Experimental Characterization

The experimental setup is composed of two direct current (DC) power supplies (PSs), a multi-meter, a thermal plate and a plastic glass box. The multi-meter is aimed at measuring the voltage changes at the thermistor (V_{Th}). The thermal plate is placed inside a plastic glass box of $6 \times 7 \times 5\ mm$ in dimension, used for isolation purposes. Four holes are drilled at the bottom of the plastic glass box in which four nuts with screws are inserted in order to stabilize the position of the thermal plate during experiments.

PS_1 is set to be variable (V_{Var}) from 3V up to 8V with an increment of 0.2 V. This voltage boundary is aimed at limiting the amount of current flowing through the plate for protection

purposes. By varying PS_1 voltage, so does the voltage at the thermistor. The change in voltage at the thermistor is used to calculate the change in the resistance and therefore the temperature of the thermistor.

PS_2 is set to a 5 V constant voltages (V_{Cte}), because using a $10K\Omega$ resistor in series yields a 2.5 V on the thermistor at 25℃. The voltage at the thermistor is acquired by the multi-meter and theoretically represented as:

$$V_{Th} = \frac{R_{Th}}{(R_{Th} + R)} V_{Cte}\ , \qquad (4-1)$$

where: R is the $10\ K\Omega$ resistance in series and R_{Th} is the thermistor resistance.

Knowing the voltage at the thermistor, it is possible to calculate its resistance each time the varying voltage status changes.

$$R_{Th} = \frac{V_{Th}}{(V_{Cte} - V_{Th})} R\ . \qquad (4-2)$$

The temperature coefficient of the thermistor is modelled with the Steinhart-Hart equation.

$$\frac{1}{T} = \frac{1}{T_0} + \frac{1}{B} ln\left(\frac{R_{Th}}{R_0}\right), \qquad (4-3)$$

where: T is the thermistor's temperature, T_0 is the initial temperature considered at $25℃ = 298\ K$, $R_0 = 10K\Omega$ the resistance of the thermistor at 25 °C and $B = 3750$ is a constant supplied by the manufacturer.

Knowing the instantaneous resistance at the thermistor enables the calculation of induced temperature at the thermistor as:

$$T = \left[\frac{1}{T_0} + \frac{1}{B}\ln\left(\frac{R_{Th}}{R_0}\right)\right]^{-1} - 273.2\ , \qquad (4-4)$$

When the thermal plate is completely isolated and fixed inside the plastic glass box and powered (PS_1 = 3V to 8V and PS_2 = 5V), the voltage at the thermistor drops continuously after a few seconds. It takes about 5 to 8 minutes for the voltage to stabilize. This voltage is recorded and an increment of $0.2\ Volts$ is applied to the PS_1. The voltage at the thermistor decreases again. When the voltage is stabilized, its value is recorded. This is repeated again until $8\ Volts$ is reached. All the voltage recorded at each increment are transformed using Equation 4-4 in order to determine the temperature variation at each increment.

4.2.3. Temperature Accuracy of the Thermistor (TH10K)

The tolerance value of the TH10K supplied by the manufacturer is used to calibrate the thermistor with accuracy. This tolerance is supplied in the form of percentage at $25℃$, known as temperature coefficient of the resistance α. The rated resistance and temperature tolerances are related by the following equation;

$$T_{Accuracy} = \frac{R_{Tolerance}}{\alpha}\ , \qquad (4-5)$$

The temperature coefficient supplied by the manufacturer is $\alpha = -4.4\%/℃$ and the resistance tolerance is ± 2 %. Using Equation 4-5, temperature accuracy is calculated at each distinct measurement.

4.3. The Fibre Bragg Grating Printing Description

The printing station consists of a laser source, the interferometric setup, a 3 directional translation stage, a super luminescent emitting diode (SLED), 2 m of a single mode fibre (SMF) and a detection system. The optical source is a frequency doubled continuous wave Argon ion laser at 244 nm wavelength, used as optical laser source. This laser can emit 13 wavelengths

in the visible and UV (C. BreckHitz et al., 2009). The two strongest lines are at 514 nm and 488 nm. The 488 nm line is frequency doubled and gives 244 nm in the ultra violet (UV). The 3 dimensional translation stage is used to optimise the position of the fibre where the irradiation takes place. The SLED is used to provide light inside the single mode fibre (SMF-28) and the optical spectrum analyser (OSA) is used as the detection system to monitor the grating's reflectivity during the experiment. The printing station setup is presented in Figure 4-2.

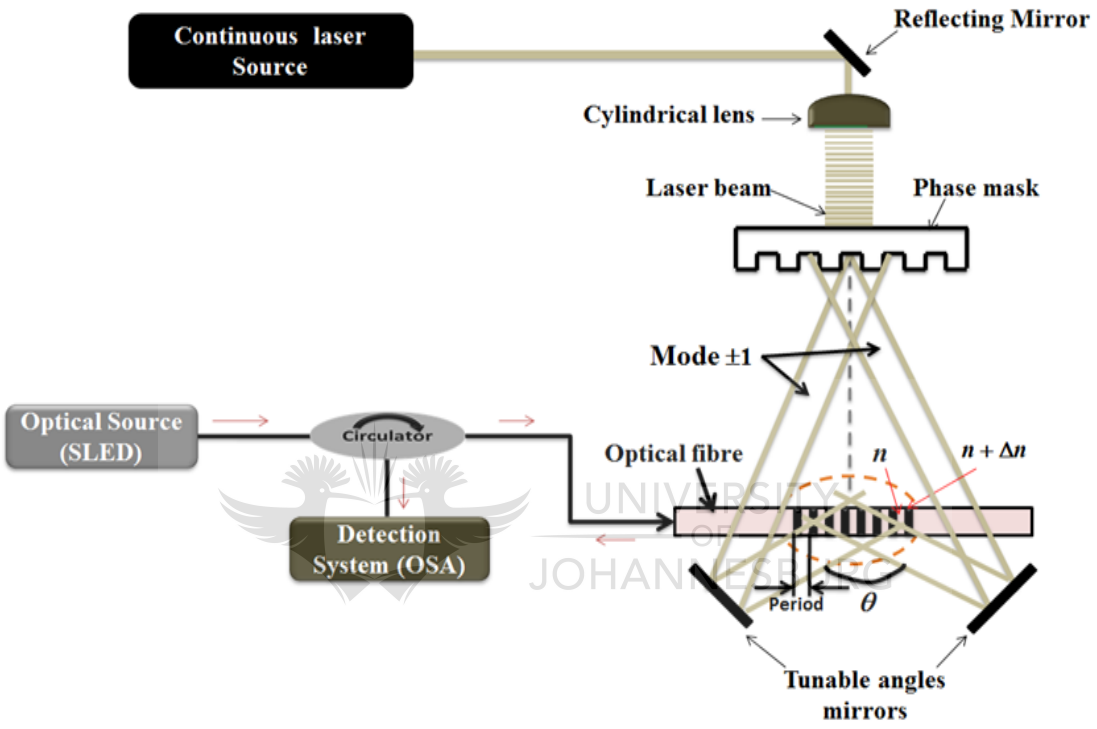

Figure 4-2. Sensor System Printing Setup.

The Argon ion laser is set to 100 mW output power and directed at a cutting knife edge used as spatial filter to size the beam spot. The beam spot sized 2.5 mm in diameter is directed thereafter to a phase mask. The phase mask is designed in such a way that the 0^{th} diffraction order is minimized to less than 3% and the ± 1 diffraction orders are maximized to 35% of the incident power (A. Othonos and K. Kalli, 1999). The ± 1 diffracted beams from the phase mask are redirected to 2 computer controlled mirrors. The SMF is placed on a 3 dimensional translation stage at the interference of the two beams from the controlled mirrors, where the fibre is printed. The Bragg wavelengths at each local sensor are selected by computer tuning the mirrors. By computer changing the Bragg wavelength results in a variation of the angles of the two interfering beams. In the sensor system, 3 wavelengths are computer selected (1550

nm, 1555 nm and 1560 nm). In each respective wavelength, 3 F-P local sensors having different cavity lengths are imprinted.

Before the printing station is on, the resolution of the OSA is set to $0.1\,nm$, $3\frac{dB}{D}$, and a wavelength range of $20\,nm$ span. The end tip of the SMF 90℃ is cleaved and attenuated thereafter.

When the printing station is on and the OSA set as explained above, the SMF fibre starts to absorb UV light. In this process, the reflectivity of the FBG monitored on the OSA grows with time until the desired amplitude is reached. This printing process could take the most 3 minutes. The monitored growth observed on the OSA is experimentally calculated according to R. Kashyap, 2008.

$$\%R = 3.5 \times 10^{\left(\frac{\Delta dB}{10}\right)}; \qquad (4-6)$$

where: $\%\,R$ is the reflectivity of the grating in percentage; 3.5 represents the Fresnel reflectivity percentage and ΔdB represents the difference in dB of the actual reflectivity of the grating and the Fresnel reference.

The printing sequence of the grating is presented in Figure 4-3.

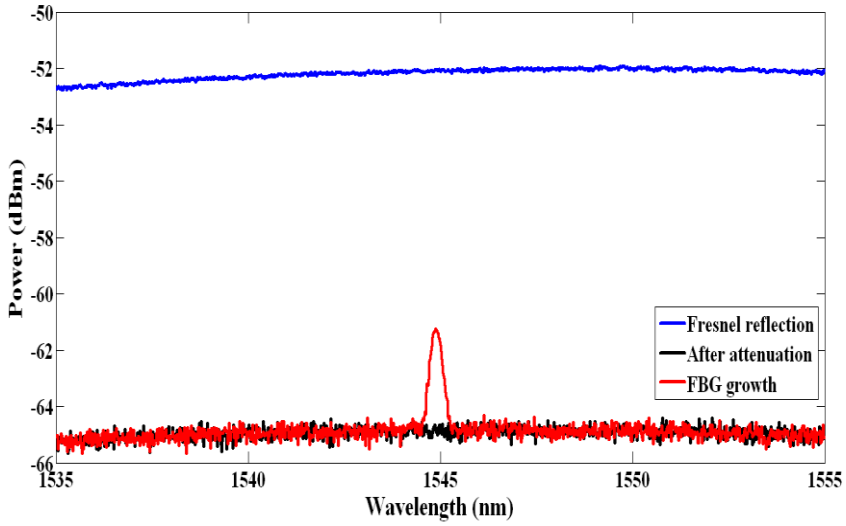

Figure 4-3. FBG Reflectivity Growth.

Before the gratings are printed, the cladding of the SMF is cleaned at each precise position and clamped on the translation stage thereafter where printing takes place. When light from the broadband source is coupled to the SMF where the gratings are printed, a 3.5% reflected Fresnel spectrum from the right angle tip end of the SMF is captured on the OSA and represented by the spectrum in blue. When the attenuation is applied at few centimetres from the tip end of the SMF, an attenuation is observed on the OSA and represented by the spectrum in black. The spectrum in red represents the growing fibre Bragg grating until the designed reflectivity is reached.

After printing the first grating, the printing argon laser is switched off. The SMF is unclamped and carefully shifted to the designed cavity length equal to 1 cm for the twin-grating local sensor presented in Figure 4-5. After re-clamping the SMF, the argon laser is switched on and the growth of the grating is observed on the OSA. This spectrum is presented in Figure 4-4.

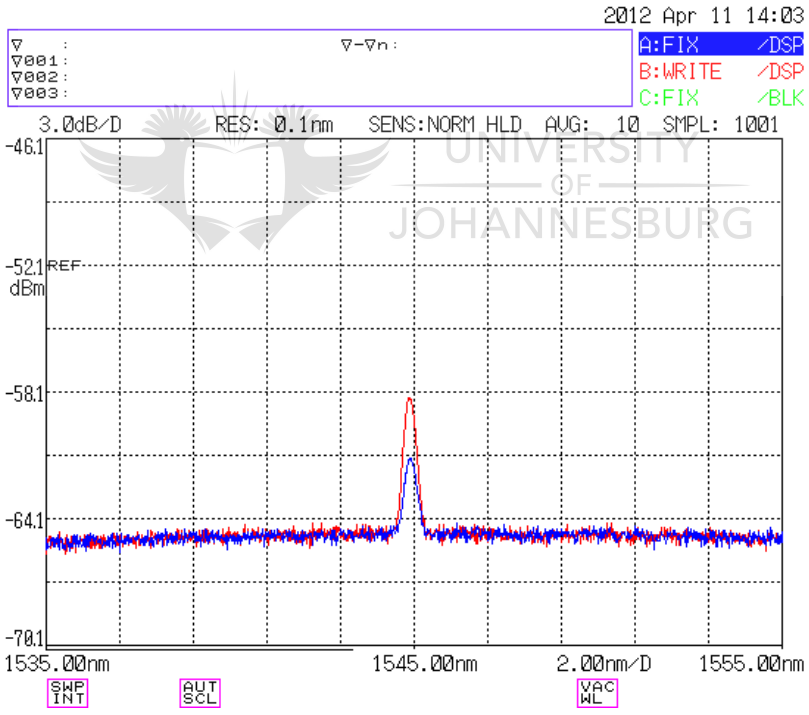

Figure 4-4. Spectral growth of the twin-grating having a cavity between.

The Figure plotted in blue represents the spectrum of the first grating printed while the Figure plotted in red represents the spectrum of the second grating. Choosing a $3\frac{dB}{D}$ on the detection system yields double the amount of the reflectance observed on the OSA. As presented on Figure 4-4, the reflectance presented in red is the double of that in blue. A zoom into Figure 4-

4 would show a cosine wave resulting from the interference from the two identical fibre Bragg gratings used.

4.4. Experimental Setup

This section presents the experimental setups of all the sensors imprinted in this project, namely the F-P local cavity, the multi-point sensor system with 5 local sensors in FDM and the multi-point sensor system in a combined FDM and WDM.

4.4.1. Fabry-Perot Local Fibre Sensor Setup

The SMF is positioned where the irradiation takes place, as described in Section 4.3, and then connected to the circulator. The Bragg wavelength is designed to be 1543.9 nm and the reflectivity monitored on the OSA, as shown in Figure 4-3. When the designed reflectivity is reached, the laser source notch is closed. The SMF is unclipped and shifted to the designed cavity of 1 cm. When clipping back the SMF, a minimal strain is applied to the fibre in order to enable a perfect overlap of the spectrums of the two gratings. When the notch of the laser source is reopened, the reflectivity of the reflected spectrum carries on growing. Since the two gratings are of identical wavelength, they overlap in their spectrums and generate an interference captured on the OSA. By using $3\frac{dB}{D}$, the reflectivity of the spectrum is doubled when a division is reached on the OSA. When the two gratings are equal in reflectivity, the system is stopped and the gratings printed are permanent. The optical setup of the F-P local sensor printed on the SMF is presented in Figure 4-5.

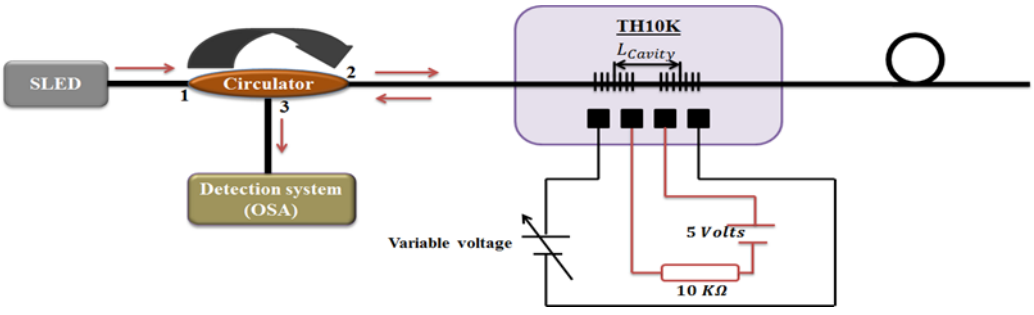

Figure 4-5. Twin-grating Local Sensor Layout.

The F-P local sensor is placed on the thermal plate inside the plastic glass box. This is aimed at testing the sensor performance. It takes some time for the temperature to settle inside the plastic glass box. After the settling time, a calibration is done as reference before any further measurement is taken. Measurements are taken every 10 minutes with a recursive increment of 0.1 V corresponding to about 1℃. The OSA is set to $3dB/Division$ and 0.01 nm resolution. The experimental procedures are kept similar to all the sensors' performance testing. The spectrums captured are demodulated to measure temperature changes.

4.4.2. Multi-Point F-P Sensor System Implemented in Frequency Division Multiplexing of 5 Local Fibre Sensors

The multi-point F-P sensor system implemented in FDM is made of 5 F-P local sensors printed on a 3 m long SMF as presented in Figure 4-6.

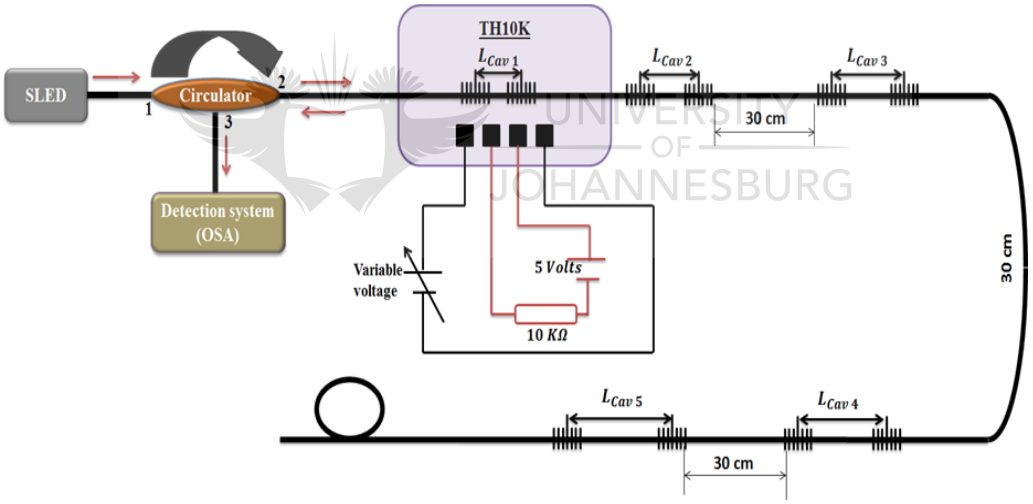

Figure 4-6. Multi-point F-P Sensor System with 5 Local Sensors Implemented in a FDM Configuration.

From design, all the gratings are of identical Bragg wavelength of 1550 nm and a reflective of 0.2 %. The separation between consecutive local sensors is 30 cm. The cavity lengths of the 5 local sensors range from 1 cm to 5 cm, with an increment of 1 cm respectively. The local sensors are printed exactly as in Section 4.4.1. The first local sensor is placed on the thermal plate inside the plastic box for temperature monitoring.

In this experiment, changes in temperature are applied to the 1st local sensor, while the other local sensors are not affected. In this way all of the sensors are tested. When the sensor system

is on, an incremental voltage of 0.1 V is applied to PS_1 from 3V to 8V, corresponding to almost 50℃ range, while the SLED provides the broadband source for all the local sensors. The thermal plate at the 1st local sensor starts heating up. Temperature equalizes inside the plastic glass box after 20 minutes. The OSA settings are kept similar to all the experiments previously done. When the system is settled, a calibration is performed serving as reference before any further measurements. The total reflected spectrums are acquired per interval of 10 minutes in a temperature increment of about 1℃. This acquired total reflected spectrum of all the local sensors is demodulated using the algorithm presented in Chapter 3. The acquired spectrum is a superposition of the entire reflection spectrum from each individual local sensor. The results of the performance of this sensor system are presented in Chapter 5.

4.4.3. Multi-point Sensor System in a Combined FDM and WDM Setup

In this experiment, a 4 m long SMF is used and the separation between local sensors is designed to 30 cm accordingly. The 9 local sensors printed on the SMF are made of 3 wavelength channels (1550 nm, 1555 nm and 1560 nm), each wavelength channel is made of 3 local sensors. From design, all the gratings in each respective wavelength channel are of identical Bragg wavelength and reflectivity. In each respective wavelength channel, the cavity length from the first to the third local sensor designed to 1 cm, 2 cm and 3 cm.

In the printing process, the optimal approach is to start with the 3rd local sensor in wavelength channel 3 (1560 nm with cavity length $L_{FP3} = 3\ cm$). This is aimed at efficiently controlling the grating growth of every local sensor. The SFM is attenuated between the 3rd and 2nd local sensors in order to enable the printing of local sensor 2 in the same wavelength channel. This process continues up until the 1st local sensor ($L_{FP1} = 1cm$) of the 1560 nm wavelength channel 3. This procedure is repeated again until the 1st local sensor ($L_{FP1} = 1cm$) in 1550 nm wavelength channel 1 is reached and printed. After the printing of local sensors in each channel, the Bragg wavelength (per channel) is computer changed. The conclusion of the 9 local sensors; printing leads to the sensing of experimental performance in the laboratory. The optical sensor system setup is presented on Figure 4-7.

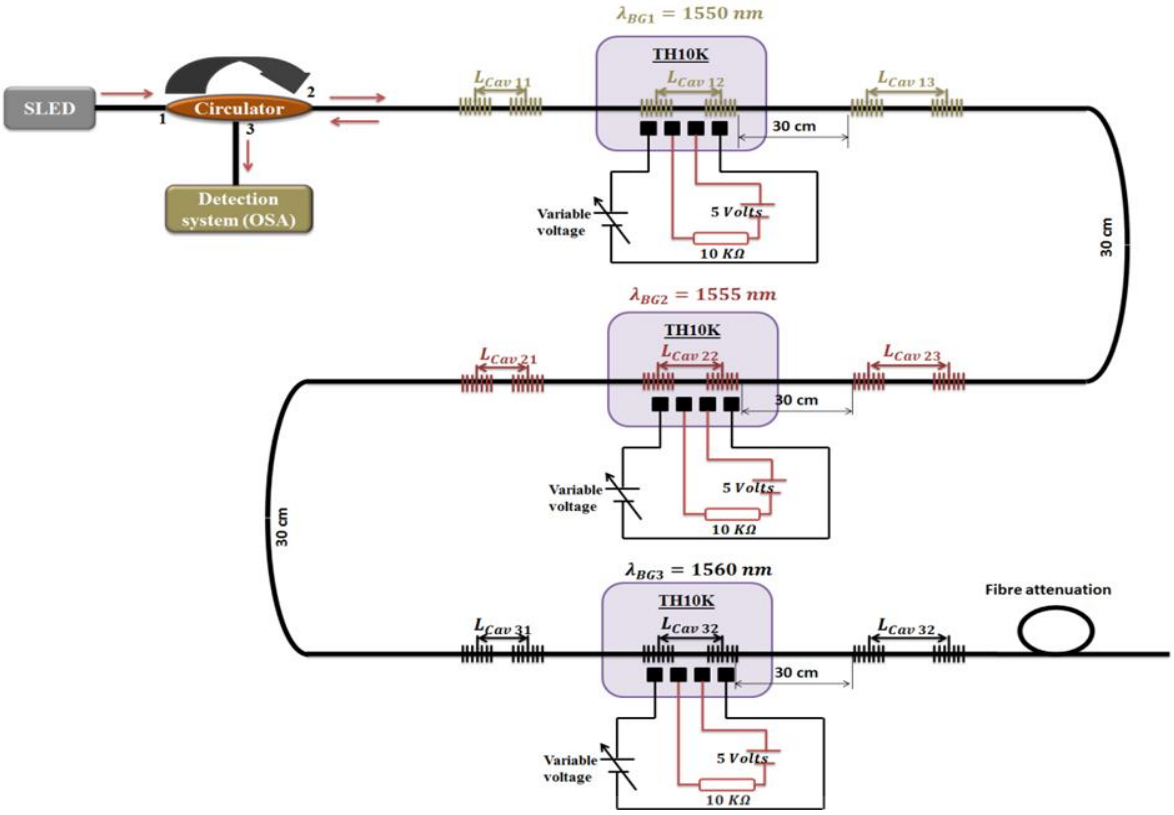

Figure 4-7. Multi-point F-P Sensor System in the Combined FDM and WDM Setup.

As presented on Figure 4-7, the combined multi-point sensor system consists of 9 local sensors arranged in 3 distinct WDM channels, that is, 1550nm, 1555nm and 1560 nm respectively. Each wavelength channel consists of 3 local sensors configured in a FDM, whereby the 1st, 2nd and 3rd local sensor have a 1 cm, 2 cm and 3 cm cavity length respectively.

In the temperature monitoring experiment, the 2nd local sensor of each wavelength channel is affected by temperature changes, while the others are not. Each of the affected local sensors is placed on a thermal plate inside distinct plastic glass boxes. The purpose of this experiment is to investigate the performance of the 3 local sensors in different channels. All the local sensors are of 0.2% reflectivity and are identical in wavelength per channel. Due to having such weak-reflectivity mirrors, many local sensors can be printed on the same serial array of the SMF and furthermore, the effect of cross-talks is considerably minimized.

When light from the SLED is launched through the optical system each respective wavelength channel reflects a superimposed interference pattern centred to its respective designed Bragg wavelength. The total reflected spectrum captured on the OSA is a combination of all the respective superimposed interference patterns from the 3 wavelength channels.

During temperature monitoring, 3 distinct PSs are used to generate power to the thermal plates used and the other 3 PSs are used to control temperature on the 3 respective thermistors. $PS1_{1-2}$, is the PS that provides variable voltage on the thermal plate of the local sensor 2 (cavity length = 2 cm) in channel 1 (1550 nm). Its settings in voltage range from 7 V to 12 V. $PS1_{2-2}$, is the PS that provides variable voltage on the thermal plate of the local sensor 2 (cavity length = 2 cm) in channel 2 (1555 nm). Its settings in voltage range from 6 V to 11 V. $PS1_{3-2}$, is the PS that provides variable voltage on the thermal plate of the local sensor 2 (cavity length = 2 cm) in channel 3 (1560 nm). Its settings in voltage range from 5 V to 10 V. The voltage on the PSs are all incremented to 0.1 V respectively. The temperature difference ranges from 56 ℃ up to 95℃ in average from one affected sensor to the other with the same increment as in previous experiments. All the other power suppliers ($PS2_{j-i}$) are set to an identical and constant voltage of 5 V.

Following similar procedures as in the previous experiments, the system is calibrated and the data is acquired at every time interval, with an increment of 0.1 V corresponding to a temperature of almost 1℃. As the temperature increment continues, a shift is observed on the total reflected spectrum per wavelength channel. The spectrum of the combined sensor system is presented in Figure 4-8 while the calibrated spectrum is presented in Figure 5-4.

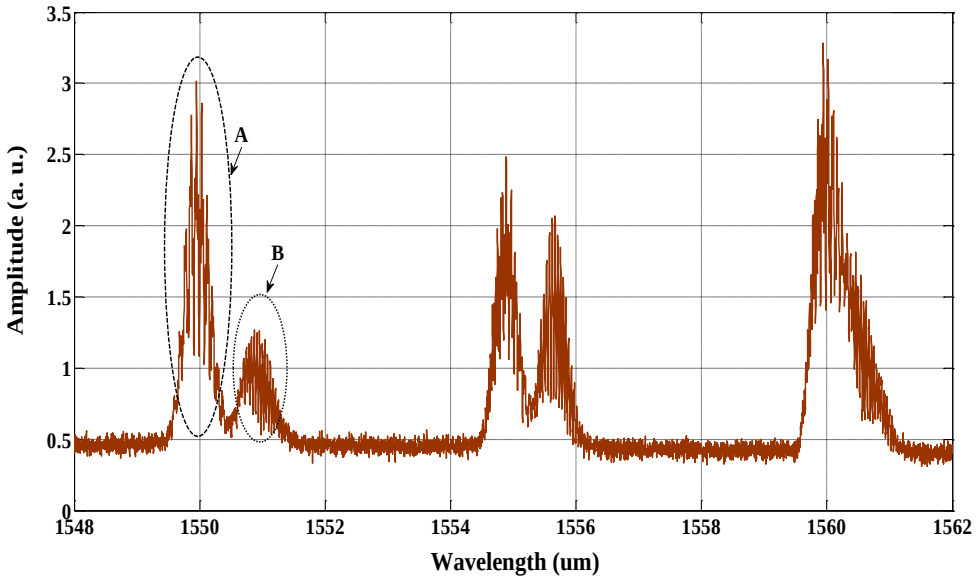

Figure 4-8. Multi-point F-P Sensor System Spectral Shift with Temperature.

Figure 4-8 is composed of all spectrum superimposed per channel. As it can be observed, the spectrum of all the interference generated by the 3 local sensors in channel 1 is centred at 1550

nm while the other spectrums superimposed from the other sensors are centred at 1555 and 1560 nm respectively. As provided in Figure 4-8, part (A) represents the spectrum of the two local sensors in channel 1 that are not affected by temperature changes, namely local sensor 1 and local sensor 3 with cavity length respectively 1 and 3 cm. The shape of this spectrum does not change considerably during the experiment, because changes in temperature are minimal inside the laboratory. In the same channel (1550 nm), part (B) represents the spectrum from local sensor 2. If no temperature changes were applied on this local sensor, the spectrum in part (A) and Part (B) would fuse. The split of the spectrum in part (A) and part (B) is only due to temperature. The shape of the spectrum in part (B) is expected. It is made of the spectrum of the Bragg grating as the envelope and that of the interference pattern. Because both the gratings and the cavity are exposed to the same temperature and are in the same fibre material, both the envelope and the interference shift as temperature changes (S. V. Miridonov *et al*., 1997).

When the variable voltages from the $PS1_{1-2}$ increase, so does the temperature on that thermal plate and as a consequence, the reflected spectrum in part (B) shifts in the positive direction while part (A) stays static as shown. During measurement, from calibration to the final measurement at 95 ℃, the data are acquired for demodulation per channel. Similar explanation and approach applies to the local sensors in channel 2 and channel 3 as their spectral shapes are observed in the other 2 channels (1555 nm and 1560 nm), as shown in Figure 4-8.

All the data acquired is demodulated in order to calculate temperature changes in each respective affected local sensor using the algorithm presented in Chapter 3. The respective results are presented in Chapter 5.

4.4.4. Resolution Test

A very important part of the sensor performance is the resolution test. Resolution is known as the smallest measurement a sensing device can perform. The purpose of this experiment is to evaluate the performance of the sensor by testing the smallest temperature changes that can be measured. The resolution of the sensor is a practical statistical process whereby the value obtained from the standard deviation is doubled. Standard deviation shows how spread out samples are. Standard deviation is used to calculate the sensor's resolution.

In this experiment, 3 local sensors in the multi-point sensor system presented in Figure 4-7 are tested where the voltages of the thermal plates are kept constant. The experimental procedure

as explained above is kept identical in terms of the settings of the OSA, the settling time for the testing to commence and the time interval to acquire the data. A set of 50 measurements (samples) is recorded in each respective channel. All the data acquired is demodulated. Infinitesimal temperature changes induce slight phase shifts, as calculated by the demodulation algorithm. These phase shifts in each local sensor are presented on a single plot in order to calculate their standard deviation. The measured standard deviation is then multiplied by two to obtain the resolution of the affected local sensor. The total resolution calculated is the average of the individual resolution from each respective affected local sensor. The results of this experiment are presented in Chapter 5.

4.4.5. The Test of 2 F-P Local Sensors Overlapping in Fourier Domain

In this experiment, 2 FDM local sensors are imprinted on the SMF using the printing station, as shown in the setup on Figure 4-2. The printing process is identical to the other grating previously printed along this project. The gratings are identical in their respective reflectivity (0.2%), Bragg wavelength (1550 nm) and physical lengths of about 3 mm. The cavity length of the 1st sensor is 1 cm and the cavity length of the 2nd sensor 1.3 cm. The 1st local sensor is placed inside an oven while the 2nd is placed inside a distinct plastic glass box and kept at constant temperature. The optical setup is presented in Figure 4-9.

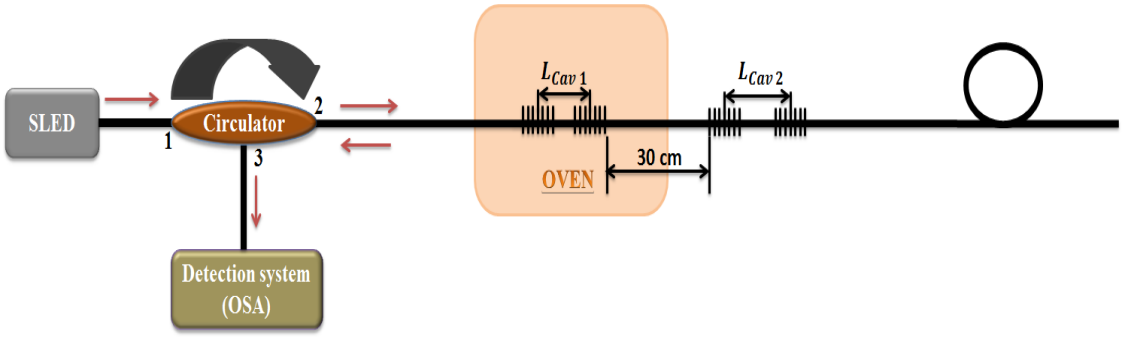

Figure 4-9. Optical Setup of 2 Local Sensors Closely Separated.

A set of 15 measurements, starting from 20°C to 35°C, are performed with an increment of 1°C at every time interval. The data acquired is demodulated thereafter. As expected, the demodulation algorithm shows that the 2 local sensors' triangle shapes overlap in their Fourier

domain, creating a region of loss of information as presented in Figure 4-10. This is completely similar to the schematic spectrums presented in the Figures 3-18, 3-21 and 3-24. The loss of information therefore yields incorrect measurements as shown in Figure 4-10.

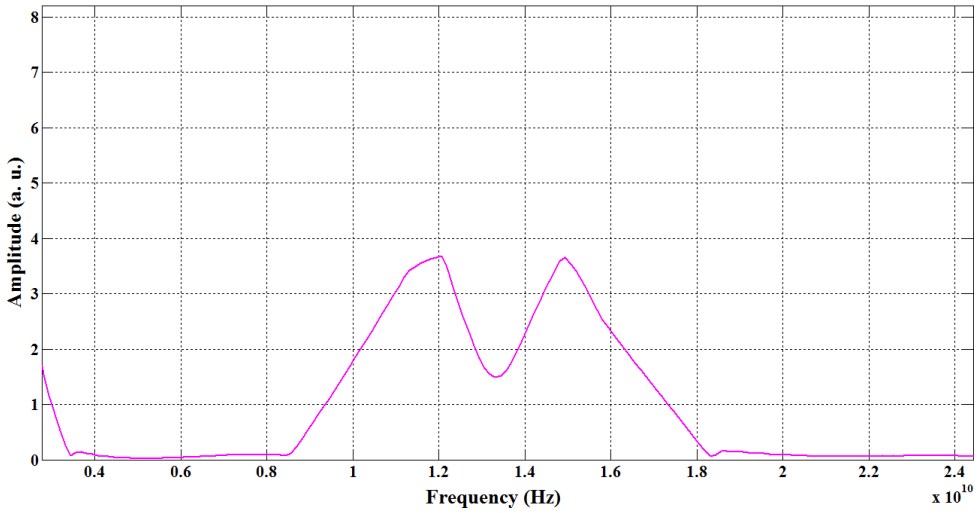

Figure 4-10. Overlapped local sensors spectrum.

From the data collected in this experiment, the results of the interrogation of the sensor under temperature changes are presented in chapter 5.

4.5. Summary

The experiments' setup leading to the experimental testing of the multi-point temperature fibre sensors based on a serial array of optical fibre interferometers, whereby local sensors are made of FBG based F-P interferometers, has been presented and discussed,. These experiments included printing of the F-P cavity, the multi-point sensor systems in FDM and the combined FDM and WDM and their respective temperature measurements. The experiment on the sensor system, whereby there is an overlap on of the triangle shapes in Fourier domain, clearly points out how far a multiplexed system can be configured depending on the specific application. All the results compiled in the present chapter are presented and discussed conclusively in Chapter 5.

5. Experimental Results

5.1. Introduction

In chapter 3, we presented the results of the sensor systems simulated in this project as well as the demodulation algorithm. The simulated sensor systems investigated include the F-P local sensor, the multiplexed systems implemented in the frequency division multiplexing (FDM) and wavelength multiplexing (WDM). The results of the simulated sensor systems whereby the triangle shapes come closer to each other in Fourier domain is also presented in chapter 3.

In this chapter, the results of all the sensor systems practically investigated are presented. These results include the multi-point sensor systems made of 5 local sensor implemented in a FDM and 9 local sensors implemented in a combined WDM and FDM. Further, the results of the experiment whereby the spectrum of two local sensors in Fourier domain come closer to each other is presented in this chapter. In the combined WDM and FDM sensor system, the investigated performance – including the sensitivity, resolution and signal to noise ratio (SNR) – are presented in this chapter.

All the sensor systems investigated in this project are imprinted on the single mode fibre.

5.2. The Thermal Plate Calibration

In order to test the performance of the multi-point sensor system, a device is importantly needed to induce temperature changes on the local sensors known as the thermal plates. Its calibration is considered as an important key element contributing to the multi-point sensor system performance. The experiment performed during the calibration is aimed at showing the temperature response of the thermal plate with respect to voltage increments. In this experiment, each voltage increment of 0.2 V corresponded to almost 2℃ after calculation using Equation 4-4. Temperature wise, the measurement ranged from almost 40℃ to 95℃, as shown on Figure 5-1 – which corresponds to a voltage ranging from 3 V to 8 V.

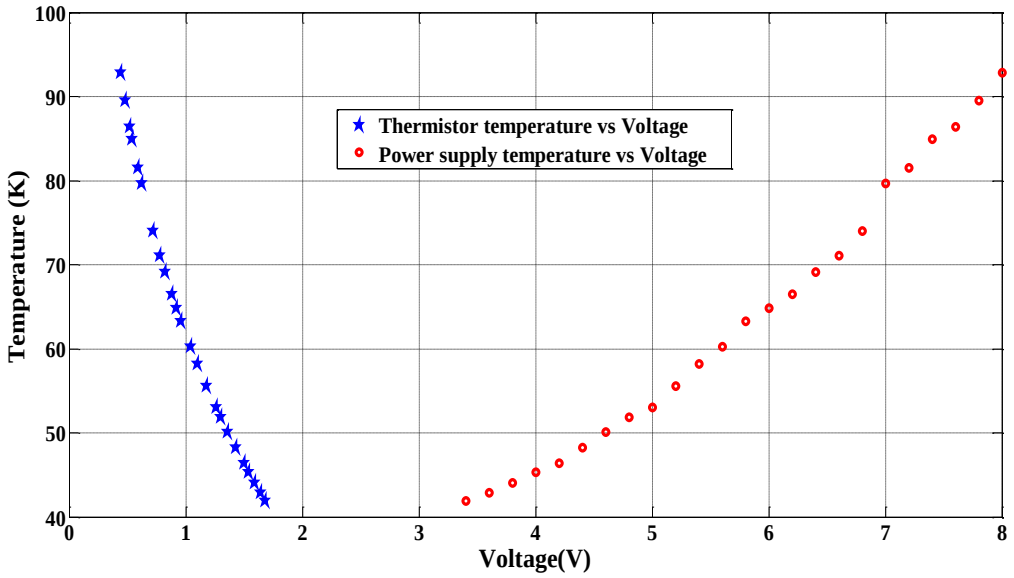

Figure 5-1. Thermistor Experimental Result.

The graph in blue represents the temperature response of the thermistor, while the graph in red represents the temperature response of the power supply (PS_1) variable voltage. The voltage at the thermistor is measured using a multi meter. The resistance of the thermistor is calculated at each voltage increment. The two graphs both present exponential responses, namely: The growth in red and the decay in blue, due to the temperature negative coefficient (TNC) characteristics of the TH10K. The thermistor response overlaps with the literatures.

If 3.2V is set on the PS_1 on the red graph, current as a result flows through the thermal plate, changing its initial voltage at the thermistor to 1.81 V (as presented in blue), therefore to 41℃ after calculation. This response is as expected per manufacturer spec sheet with respect to the specific thermal plate used.

5.3. The Reflectivity of the FBG

From the design prospective the reflectivity of the grating is practically measured to be 0.2 %. This reflectivity is also calculable using the equation presented in chapter 4 (Equation 4-6). Using a low power laser compared to a pulsing laser on the printing station as the optical source to print the gratings is clearly aimed to achieve this much reflectivity using a single mode fibre (SMF). One of the reasons of using weak reflectivity gratings is aimed at printing as many local

sensors as possible on a serial array on the SMF because of low-insertion losses. The results of 0.2 % reflectivity using such a printing system is achieved. This reflectivity is expected when using SMF.

5.4. Multi-point Fibre Sensor Systems Performance

5.4.1. Multi-point F-P Sensor System Implemented in Frequency Division Multiplexing of 5 Local Fibre Sensors Results

In this experiment, the multi-point sensor system is composed of 5 local sensors imprinted on a single array on the SMF fibre in a FDM configuration. In this configuration, each local fibre sensor has its own and specific cavity length (1, 2, 3, 4 and 5 cm respectively), different from one another. This enables each respective identical grating to have a specific interference frequency. The frequency of each respective local fibre sensor depends on the, refractive index of the fibre, the characteristics of the gratings and the separation between the identical gratings. Having a sensor system whereby each has its specific frequency, yields triangle shapes when FFT is applied. The triangles shapes are centred to the frequency of the interference of each local fibre sensors respectively in Fourier domain as presented in Figure 5-2.

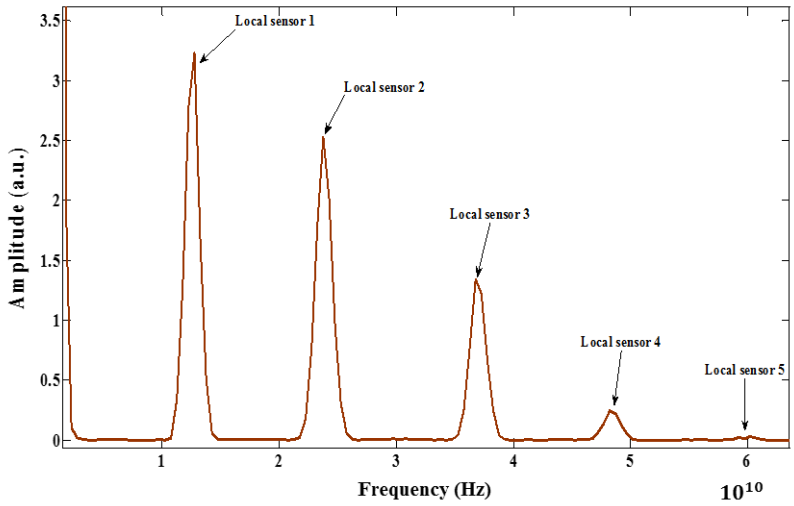

Figure 5-2. FFT Spectrum of the Multiplexed 5 Local Sensors in FDM.

As presented in Figure 5-2, the amplitude of the triangles shapes decreases with the increase in the cavity length of the local sensors. This is mainly due to the coherence length of the super

luminescent emitting diode (SLED) and the attenuation inside the SMF. Compared to a laser diode, the coherence length of the SLED is shorter. The visibility of the fringes in each local sensor changes with the coherence length. It can also be observed that the local sensor 5 with 5 cm cavity length is approaching the limit of the system coherence length. This clearly shows that the fringes from a cavity length of more than 5 cm could not be visible using this specific SLED.

In this experiment, the 1st local fibre sensor – having a cavity length of 1 cm – is affected by temperature changes using the thermal plate, while the other 4 local fibre sensors are kept unaffected. After applying our demodulation algorithm, the phase response of the 1st local fibre sensor in this multi-point FDM system presented in Figure 5-3.

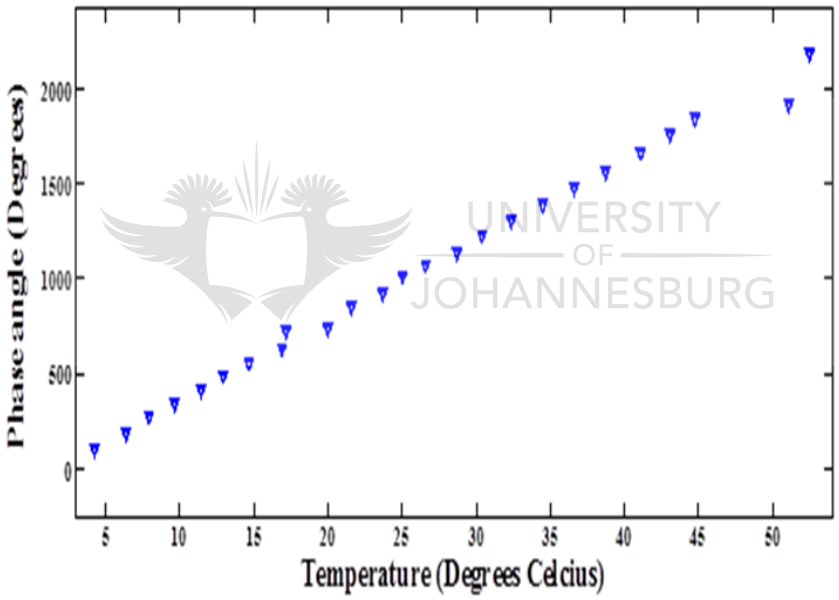

Figure 5-3. Multi-point FDM Sensor System interrogation of Local Sensor 1.

As presented in Figure 5-3, from design and the simulation results, the changes in phase (degree) are linearly proportional to changes in temperature. This is in accordance with the literature. The phase response of the simulated system and the experiment overlap; clearly showing the exactness of the demodulation algorithm used. The two blue dots out of the straight line in Figure 5-3 are sudden temperature fluctuations induced by the voltage fluctuation at the thermistor, due to lack of efficient control. The spectrum presented in Figure 5-3 is clearly as expected from design and simulation.

4.5.1. Multi-point Sensor System in Combined FDM and WDM Results

In this experiment, the multi-point sensor system is a combination of 9 local fibre sensors implemented in three sets of wavelength channels as WDM, each one made of three local fibre sensors arranged in an FDM configuration. They are all imprinted on a serial array of a 4 m long SMF fibre. As said earlier, all the local fibre sensors imprinted are of low-reflectivity. In this sensor system, the 2nd local sensor of each wavelength channel, having 2 cm cavity length, is affected by the heat from the thermal plates, while the others are not. The total reflected spectrum captured on the optical spectrum analyser (OSA) is presented in Figure 5-4.

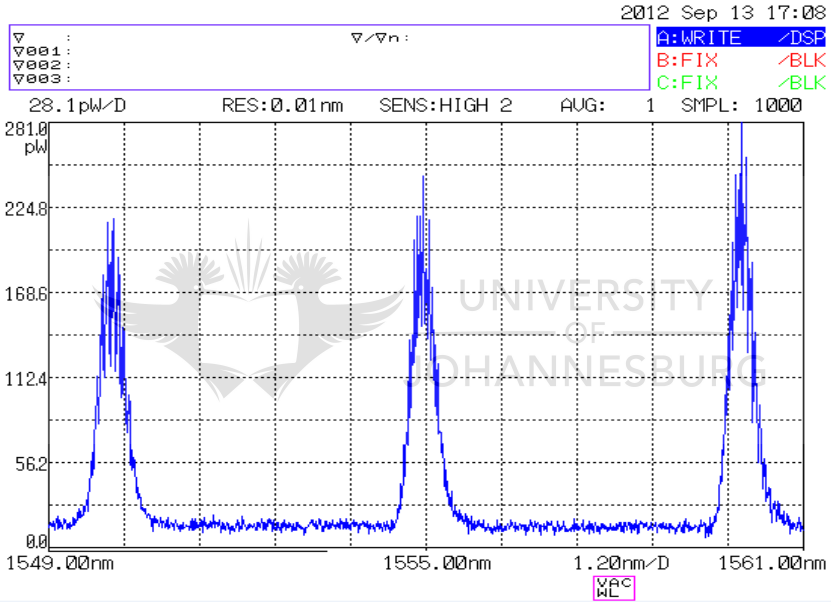

Figure 5-4. Spectrum of the Combined Quasi-distributed System of 9 Local Sensors.

As presented on Figure 5-4, the total reflected spectrum is made up of 3 superimposed interference patterns centred at each respective wavelength channel. The interference at each wavelength channel is a superposition of all the interference patterns generated by the respective local fibre sensors. The amplitude of the interference of the 3 wavelength channels is almost identical, which is as expected by design.

During the evaluation of the performance of the sensor system, the spectrum is individually acquired in each wavelength channel. These spectrums are thereafter demodulated individually, using the demodulation algorithm presented in this project. Applying the FFT,

the 2nd triangle shape representing the 2nd local fibre sensor at each wavelength channel is interrogated. The wavelength response of the respectively affected by temperature and interrogated local fibre sensors is presented on Figure 5-5.

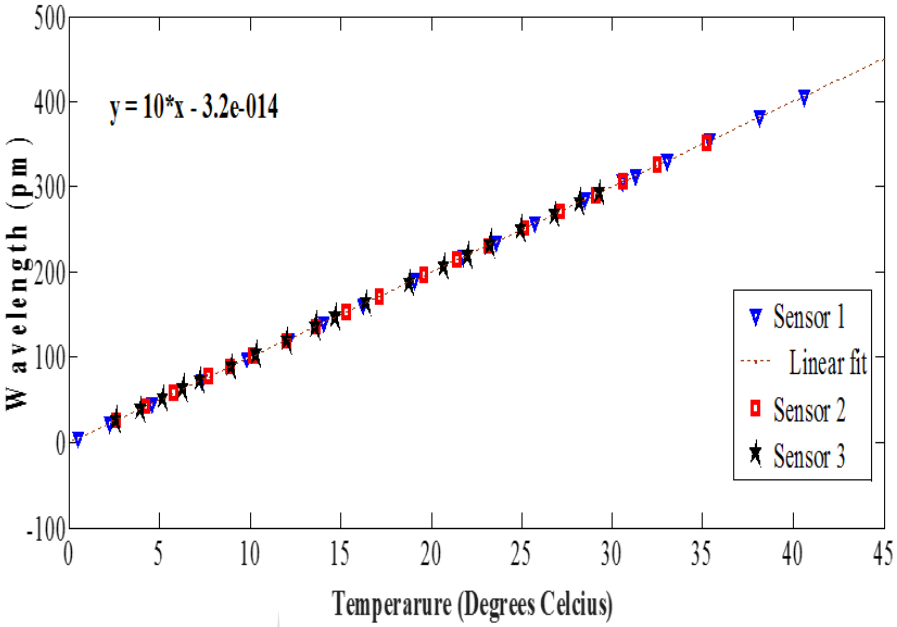

Figure 5-5. Response of the multi-point fibre sensor system made of 9 local sensors where 3 local sensors are affected by temperature changes.

The temperature response presented on Figure 5-5 is a combination of all the interrogated local fibre sensors on the same plot. The graph in blue represents the local fibre sensor affected in wavelength channel 1, while the graphs in red and black represent the local sensors affected in wavelength channel 2 and wavelength channel 3 respectively. Their respective responses to temperature changes overlap regardless of their wavelength channels. This is because all the affected local fibre sensors that have similar cavity lengths have been optimally imprinted. A linear fit is used to approximate the sensitivity of the system to 10 pm/℃. These results agree with the literature. This linear fit also overlaps with the combined temperature response as shown on Figure 5-5. The difference in temperature from different local sensors is due to their respective thermal plates' characteristics.

5.5. Resolution Test Results

An important experiment during the test of the multi-point fibre sensor system is the resolution test. This test is aimed at evaluating the smallest temperature changes that can be measured by the multi-point sensor system. In this experiment, the local sensors previously affected by temperature changes are still used. They are kept in their respective plastic boxes at constant temperature on their respective thermal plates (as explained in Chapter 4).

In this experiment, infinitesimal phase variations are calculated over static temperature changes using our demodulation algorithm. In this task, 50 data are taken from each individual local fibre sensor interrogated in each wavelength. The respective phase responses are all plotted on the same graph in order to reveal the standard deviation and therefore the resolution of the sensor as presented in Figure 5-6.

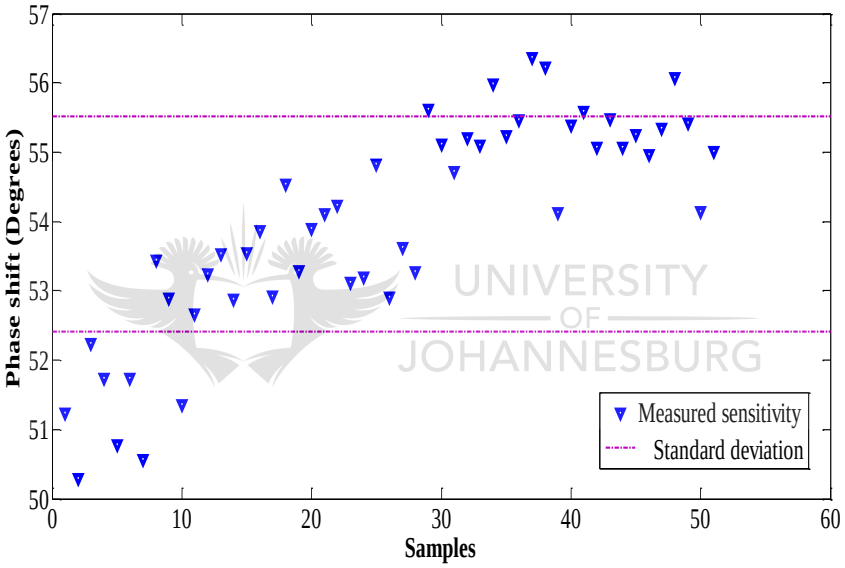

Figure 5-6. Resolution test phase response.

The standard deviation is the most common measure of variability, measuring the spread of the data set and the relationship of the mean to the rest of the data. If the data points are close to the mean, indicating that the responses are fairly uniform, then the standard deviation will be small. Conversely, if many data points are far from the mean, indicating that there is a wide variance in the responses, then the standard deviation will be large. If all the data values are equal, then the standard deviation will be zero.

The generated standard deviation in angular degree is 7.55° for the 1st local sensor tested, 7.65° for the 2nd and 7.60° for the 3rd local sensor. Using Equation 2-45, with a cavity length of 2 cm, the standard deviations of the tested local sensors in respect of temperature are $\sigma_1 =$

0.121℃, $\sigma_2 = 0.123$℃, and $\sigma_3 = 0.122$℃ respectively. Therefore, the total resolution of the sensor system is an average of that of the tested local sensors given by: to $res = 0.125$℃.

5.6. Test of 2 Local F-P Local Sensors Overlapping in Fourier Domain Results

The test of the 2 local fibre sensors whereby the triangle shapes in Fourier domain come closer to each other is aimed at experimentally investigating the accuracy of the multiplexed system with respect to the multiplexing capability in the serial array. This clearly depends on the application. In this experiment, the sensor system is made of 2 local sensors FDM multiplexed, where the cavity length of the 1st local sensor is 1 cm and that of the 2nd is 1.3 cm. The gratings are identical in their respective reflectivity (0.2%) and in Bragg wavelength (1550 nm). The affected local sensor is placed inside an oven. When the oven is on, temperature increment is applied from 20℃ to 45℃ with 1℃ increment for each time interval. From the design prospective, the spectrum generated by the sensor system is also an interference pattern. It is captured on the OSA, calibrated and then Fourier transformed (FT). The FT spectrum is an overlapped triangle shape as expected and approximated to a 35% overlap. Using the demodulation algorithm presented in this project, the results of the sensor systems are presented in Figure 5-7.

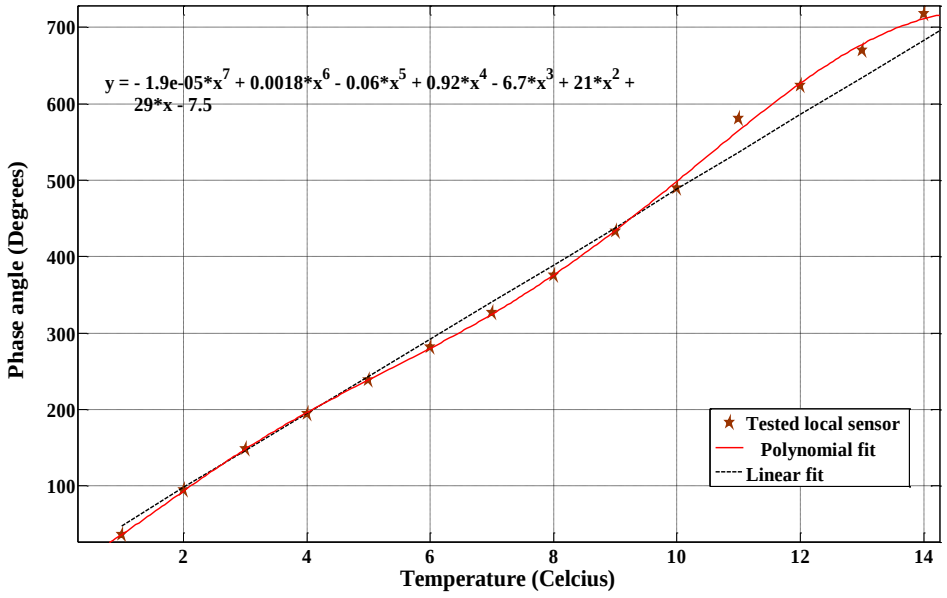

Figure 5-7. Overlap Test Combined Plot with the Normal-sized Cavity.

The spectrum in red on Figure 5-7 represents the phase response of the 1st local sensor in the sensor system composed of 2 local sensors where cavity lengths of local sensor 1 and 2 are respectively 1 cm and 1.3 cm. In this setup, local sensor 1 is exposed to temperature changes. This experiment is aimed at achieving the triangle shapes to come closer towards each other in Fourier domain.

The graph in grey clearly shows a linear fit of the affected fibre sensor to temperature changes. From the temperature response on the graph in red on Figure 5-7, the response of the 2 local sensors closely separated (overlapped) wiggles around the straight line. This clearly proves that the temperature response of the overlapped local sensor is not linear. Using statistical analysis, the system's error due to the overlap is calculated to 1.6℃ base on the system used.

The optimization of the sensor system aimed to increase the number of the local sensors on the serial array is addressed using the spectrum of the 5 FDM local sensors system. It is observed on Figure 5-2 that because all the gratings have identical characteristics, so is their bandwidth. Therefore, more local fibre sensors can be accommodated in-between. Even if in their respective Fourier domain they overlap, they can still work properly to a certain extent, depending on the specific application.

In this sense, 2 local sensors can be inserted in between the triangle shapes containing the sensor information presented in Figure 5-8.

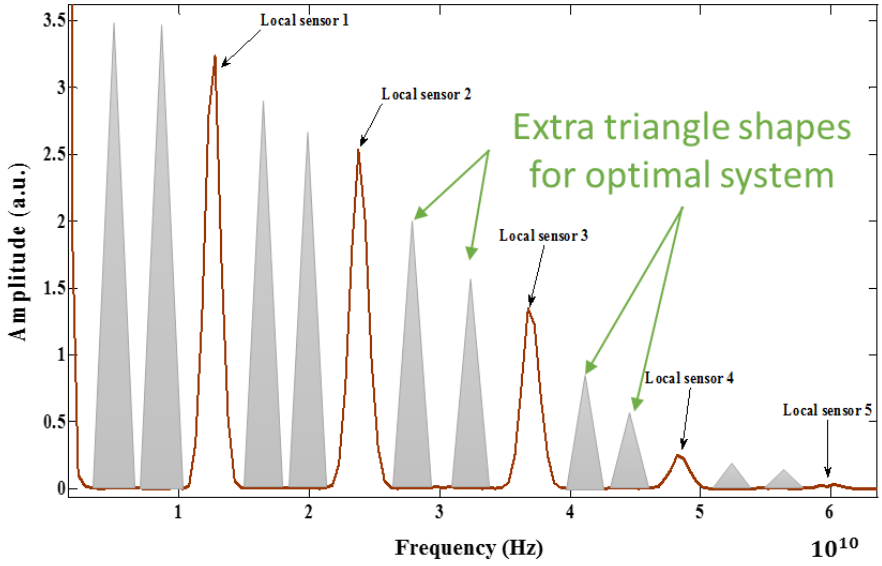

Figure 5-8. Optimal configuration of the FDM made of 5 local sensors.

This clearly confirms that, with the SLED in our laboratory, the optimal sensor system can accommodate 15 local sensors where the longest cavity length should not exceed 5 cm for fringes visibility. In such system, the difference in cavity length must be carefully designed to avoid the triangle shapes to move towards each other as presented in chapter 3 (Table 3-1).

A theoretic investigation is presented in chapter 3 whereby the triangle shapes of local sensor 2 moves towards that of local sensor 1 in the order of 25 %, 50% and 75%. Looking at the spectrum presented in Figure 5-8, the number of local sensors can be also optimized using a 50% overlap. In such situation, the spectrum of the sensor system is presented in Figure 5-9.

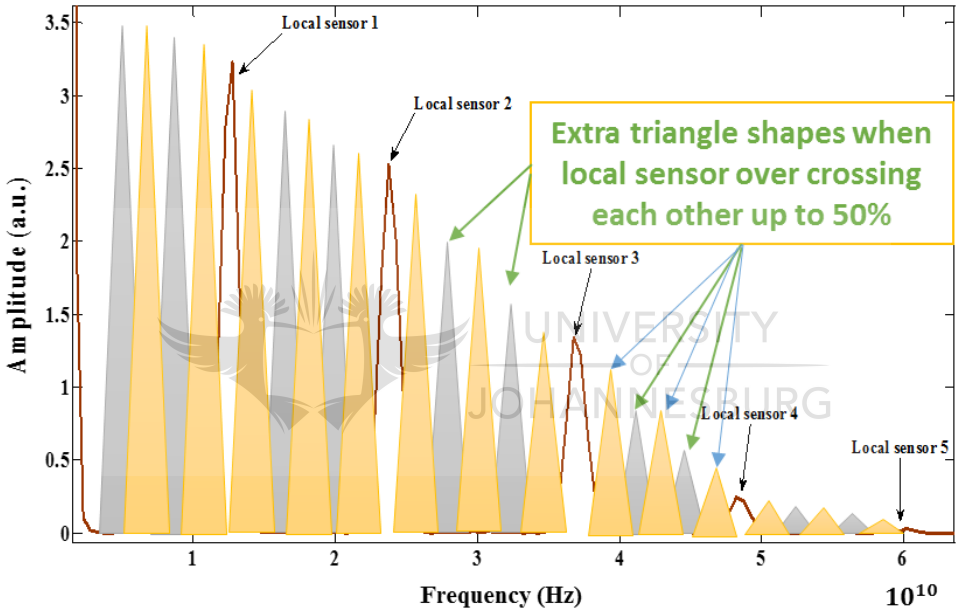

Figure 5 9. Optimal configuration of the FDM made of 5 local sensors implemented with a 50% overlap.

In this setup, the number of the local sensors using our laboratory SLED can be optimized to 25 local sensors. The challenges in this setup is the correct design of the cavity length and their efficient implementation on the serial array during the printing.

5.7. Results Discussion

The purpose of this project is to investigate theoretically and practically a multi-point temperature fibre sensor based on a serial array of optic fibre interferometer. The multi-point

optical fibre sensor system is designed and built in F-P configuration using identical fibre Bragg grating as mirrors that form the cavity. Using weak-reflectivity identical grating in this F-P configuration, the multi-reflectivity of light inside the cavity is considered to be a first order interference. Having identical-grating of weak-reflectivity, many cavities can be imprinted in series on a single fibre. In this regard, we imprinted 9 cavities on a serial array of about 4 m length of SMF fibre in a combined WDM and FDM configuration. This sensor system is designed to have 3 wavelength channels (1550 nm, 1555nm and 1560 nm respectively) in a WDM arrangement, where 3 cavities are imprinted and arranged in a FDM and whereby the cavity length of the 1st, 2nd and 3rd are 1 cm, 2 cm and 3 cm respectively in each wavelength channel. The reflectivity of all the twin-gratings in the sensor system is designed, measured and calculated at 0.2%. Using the demodulation algorithm presented by Miridonov *et al.*, 2001, the performance of the system is being tested and the respective results presented. We went beyond the physical separation boundaries between consecutive cavities to look for more insight into the sensor system's behaviour in a dense multiplexing system. The results are presented and commented.

The performance of the 3 local fibre sensors affected by temperature changes from the heating plates exhibits good linear behaviour as expected and as shown on Figure 5-5. The sensor sensitivity of ($\frac{10\ pm}{℃}$) is measured and this result is similar to the literatures. This sensitivity is typical to the SMF. Furthermore, the response to temperature changes of the affected local fibre sensor overlap as observed. This response is also expected as all 9 local sensors are imprinted on the same fibre material. Therefore, regardless to the wavelength channels, the sensor response to temperature is almost similar when the cavity length is kept identical for all the local sensors. A gross SNR of 3.65 dB as calculated is also expected due to the weak-reflectivity of the identical gratings.

In the resolution test, differential temperature changes are measured and their respective relative phases calculated. Even though the calculated resolution of 0.125℃ can still be improved; it can be seen as reasonable for this sensor type. One way of upgrading the sensor's resolution would be to increase the cavity length of the local sensors. One of the drawbacks of increasing the cavity length is the limitation of the resolution capacity of the OSA and the coherence length of the SLED.

In the simulation investigation of the two local fibre sensors closely separated, the task is aimed at observing the phase response of the affected local fibre sensor to temperature changes. Using

simulation, the results of the two local sensors whereby their spectrums come closer in Fourier domain such that their respective triangle shapes touch each other at about 25%, 50% and 75 % have been presented. From the simulation results, it is found that when the triangle shapes come closer and touch each other to about 25 %, the calculated error of $0.02\,rad$ does not affect the sensor sensitivity extensively. From the 2nd and the 3rd simulation results presented on the Figures 3-21 and 3-24 respectively, it is found that – if the difference in the cavity length between the two local fibre sensors is not at least twice the Bragg grating length – their respective responses to temperature changes are not more linear presenting errors of $0.06\,rad$ and $0.187\,rad$ respectively. This is because, as the two local fibre sensor overlap in Fourier domain, the unaffected local sensor impacts on the results of the affected system. These errors grow as the second local sensors are affected therefore impaction of the overall performance of the sensor system.

A further overlap test was experimentally conducted in order to observe the response of the two local sensors when their triangle shapes come closer to each other. The two local sensors came closer to about 35%. Achieving this much was not an easy task, which could be improved in further and future experiments. The results of this experimental investigation are presented in Figure 5-7. From the results, a system error of 1.6 ℃ is evaluated using the Cramer Rao approach and which clearly shows that such system can be used to monitor temperature changes where a temperature difference of 1.6 ℃ should not affect the performance of the system monitored. The advantage of such sensor system is the increase of the number of local sensors implemented on the serial array as an improvement while losing on the sensor accuracy. Such improvement is presented and commented in the Figure 5-8 and Figure 5-9. The increase of the number of local sensors on the system is therefore limited by the coherence length of the optical source. Using the SLED as optical source clearly aimed to reduce the cross-talks can be seen as an advantage of the system even though its optical power is low as compared to a tuneable fibre laser. Therefore, the impact of the errors in the situation where the local sensors come intentionally closer to each other depends on the sensors application.

During the course of this project, difficulties have been experienced. These difficulties have enabled to optimally print local sensors on the single mode fibre. When the SMF fibre is exposed to the heat energy from the laser source. The heat energy creates a thermal stress on the SMF fibre. The thermal stress builds up to a point whereby the fibre could not absorb UV

radiation. As the irradiation carries on, the reflectivity of the grating dips down until it is back at the initial starting point.

The power fluctuation of the laser source and the miss-alignment of the interferometric setup of the printing station has also been regarded as problems during experiments. To avoid miss-alignment, a minimum strain must be applied when placing the fibre on the groove. By applying minimal strain, all the local fibre sensors are expected to be printed in identical wavelength and can therefore keep their interference pattern perfectly overlapped. The minimal strain on the FBGs is perfected by practice.

5.8. Summary

The results of the experiments performed in this chapter have been presented and discussed whereby the performance of the multi-point sensor system and the situation where the triangle shapes of two local sensors move towards each other were tested. The results presented in this chapter clearly show an overlap with the literature. The conclusion of this project is presented in chapter 6.

6. Conclusion

This project presents a development of a multi-point temperature fibre sensor based on a serial array of optical fibre interferometers**.** The objective of this project is to investigate, design, simulate and build a fibre Bragg grating (FBG) base Fabry-Perot (F-P) fibre sensor system where a large number of local sensors could be implemented on the serial array and have high measurement accuracy.

The working principle of the FBG based local sensors and the sensors fabrication are discussed. The simulation of the local sensor and the multi-point sensor system have been assessed with relevant theory. In the multi-point sensor system, Frequency division multiplexing (FDM) and wavelength division multiplexing (WDM) have been thoroughly discussed in the simulations. Based on the theory, the multi-point sensor system is practically implemented in a FDM, WDM and in a combination of FDM and WDM aimed at increasing the number of local sensors to be imprinted on the single mode fibre (SMF). The combined FDM and WDM sensor system is composed of 9 local sensors. The sensor system is made of 3 wavelength channels (1550 nm, 1555nm and 1560 nm), where 3 local sensors are FDM implemented per channel. Further investigations (simulation and experimental) whereby the triangle shapes of two local sensors intentionally cross each other to about 25%, 50%, 75% and experimentally 35% are addressed.

In each of the experimental fabrication of the sensors, the ultra-violet (UV) induced FBG of weak reflectivity is imprinted on the fibre core by irradiating a single mode fibre to UV Argon laser beam. Each pair of the identical weak-reflectivity gratings forms a F-P interferometer that is used to monitor temperature changes. Numbers of identical weak-reflectivity gratings (local sensor) implemented on the single mode fibre is known as the serial array. The local sensors are placed at defined positions on the serial array.

The monitoring of temperature changes in local sensors is based on Fourier transform (FT) shift properties. The measurement system uses an optical spectrum analyser (OSA) as detection system whereby spectral shifts are captured. This is addressed using the demodulation algorithm presented by S. V. Miridonov *et al.*, 2001.

The performance of the multi-point temperature sensor system, including the sensor sensitivity, the sensor resolution, the multiplexing optimization, and the crosstalk between local sensors

are investigated. In this regard, a sensitivity of ($10\ \frac{pm}{℃}$) and high resolution ($0.125℃$) have been completed. A gross optical SNR of $3.65\ dB$ has been calculated. A multiplexing capacity of hundreds of local sensors is predicted in an optimal design using the optical setup presented in Figure 4-6.

A further experimental result whereby the spectrums of the triangles shapes over cross each other in Fourier domain revealed the trade-off between the accuracy of the system and it multiplexing capability as presented, depending of the application.

In conclusion, this project presents a promising technology for the quasi-distributed F-P fibre sensor for temperature monitoring applications by integrating a large number of optical fibre sensors into a serial array in a large area. Improving the signal power from the local sensors should lead the sensor system presented in this project to be used in vibration sensing. It has been shown that the objectives of the present research have been fulfilled. This sensor presents a high sensitivity and high resolution.

6.1. Future work

The multi-point temperature optical fibre sensor based on a serial array of optical interferometers should be more beneficial if it is applied to dynamic monitoring, such as vibration sensing. Difficulties in implementing the investigated sensor system for vibration sensing is due to the low-reflectivity of the identical gratings forming the local sensors. In such system, the optical spectrum analyser (OSA) is not fast enough to capture the dynamic changes. Using a tuneable diode laser as a fast scanning source with a photo detector works better, is expensive and has a problem of cross talks. This is due the coherence length of the laser that is greater than that of the broadband source. Using the super luminescent emitting diode (SLED) as the optical source helps with the cross talks but needs a scanning system. The scanning system is made of an optical filter and a photo detector. Due to the nature of the sensor system (weak-reflectivity gratings) presented in this project, the reflected signal cannot be detected due to the losses at the filter and the attenuation at the photo detector.

The following are suggested for future work:

- Implementation of the sensor system for real time monitoring, which would be an important step ahead.

- A further investigation and description of the present system, whereby the optical power of the reflected signal from the local sensor is increased. The proposed systems include:

    I. A system whereby the F-P linear cavity is made of an EDFA
    II. A system whereby the reflected optical signal from the local sensor is amplified using an EDFA.

Looking at the linear cavity configuration, the length of the Erbium doped fibre should be precisely designed in order to overcome the losses inside the doped fibre. In order to achieve higher gain with small cavities, the Erbium doped fibre concentration can be increased. But this increase presents drawbacks giving rise to un-bleachable losses that compromise the devise efficiency, as well as the ion clustering effects, (E. Delevaque *et al*., 1993; J. L. Wagener *et al*., 1993). The un-bleachable loss is attributed to ion-ion interactions inside the cluster giving rise to a co-operative up-conversion process between two neighbouring excited states. The nets results of this up-conversion process is one ion in the ground state level whilst the other quickly return to the metastable level via multi-phonon relaxation (J. L. Wagener *et al*., 1993). The other approach used to achieve a higher gain is to co-dope the Ytterbium ions with the Erbium ions in the fibre (T. Wang, 2009). This co-doped fibre presenting peak absorption cross section can achieve higher pump absorption efficiency (T. Wang, 2009). Therefore, the co-doped Erbium/Ytterbium doped fibre is the ideal gain medium for models using shorter length (J. Nilsson *et a*l., 1994). Using co-doped Erbium/Ytterbium fibre in shorter lengths, the reflected spectrum captured on the detection system should be more amplified, due to the higher gain obtained from the co-doped fibre. If the reflected amplified signal overcomes the F-P filter attenuation and the photo-detector noise, the application of the present project should be tremendous driving force for dynamic measurements. When applied to temperature sensing systems, the co-doped Erbium/Ytterbium should enable a higher gain and lead to an increase in SNR of the sensor system.

7. APPENDIX A

7.1. Conference Participations

Diethelm Schmieder, Rajatha Samaradiwakera, Michelin Della Tamin, "***Micro Machining of Fabry-Perot Interferometers in Optical Fibers to Manufacture Temperature Sensors***", Accepted for a Poster By South African Institute of Physics, September 29-31, 2010.

M. Della Tamin, R. Martínez Manuel, J. T. Guillen-Bonilla, "***Multipoint Fibre Sensor for Temperature Measurements***", Accepted Work in Progress for Talk Presentation by SATNAC, September 4-8, 2011.

M. Della Tamin, E. E. Okafor, R. Martínez Manuel, J.J.M. Kaboko, "***A Theoretical Model and Simulation of Low-Reflectivity Active Linear Cavity for temperature sensing***", SAIP 2013, accepted for a talk presentation.

8. Reference

[1] A. D. Kersey, M. J. Marrone, A. Dandridge, "*Experimental investigation of polarization induced fading in interferometric fibre sensor arrays*", Electron Lett., 27(7), pp.562-563, 1991

[2] A. D. Kersey, "*A review of Recent developments in fiber optic sensor technology",* Optical Fiber Technol., 1996. 2: p. 291-317

[3] A. N. Starodumov, L. A. Zenteno, D. Monzon, and E. De La Rosa , "*Fiber Sagnac interferometer temperature sensor*", Centro de Investigaciones en Optica, 37150 Leon, Gto, Mexico , Appl. Phys. Lett. 70, 19 (1997)

[4] A. Othonos, K. Kalli, "Fiber Bragg Gratings Fundamentals andApplications in Telecommunications and Sensing", Artech House London (1999).

[5] *A.* Selvarajan*, "Fibre Optic Sensors and their Applications",* Chairman Department of Electrical Communication Engineering, Indian Institute of Science, Bangalore - 560 012

[6] A. V. Brakel, P. L. Swart, "*Temperature-compensated optical fiber Michelson refractometer*", *Opt. Eng.* 2005, *44*, 1576-1580.

[7] A. Signorini, S. Faralli, M.A. Soto, G. Sacchi, F. Baronti, R. Barsacchi, A. Lazzeri, R. Roncella,G. Bolognini, F. Di Pasquale, "*40 km long-range Raman-based distributed temperature sensor with meter-scale spatial resolution*", ©2010 Optical Society of America, OCIS codes: (060. 2370) Fiber optics sensors, (190.5650) Scattering, Raman.

[8] B. Gholamzadeh, and H. Nabovati, "*Fiber Optic Sensors*", World Academy of Science, Engineering and Technology 42 2008

[9] B. H. Lee, Y. H. Kim, K. S. Park, J. B. Eom, M. J. Kim, B. S. Rho and H. Y. Choi; "*Interferometric Fibre Optic Sensors*", *Sensors* 2012, *12*, 2467-2486; doi: 10.3390/s 120302467

[10] B. D. Gupta, "Fibre optic sensors: Principles and applications", Textbook, Nipa, 2006, ISBN: 81-89422-11-1

[11] B. D. Gupta, "Fibre optic sensors: Principles and applications", Textbook, Nipa, 2006, ISBN: 81-89422-11-1

[12] C. S. Baldwin, "*Multi-parameter sensing using fiber Bragg grating sensors*", Proc. of SPIE Vol. 6004, 60040A, (2005)

[13] C. Crunelle, M. Wuilpart, C. Caucheteur and P. Mégret, *" Original interrogation system for quasi-distributed FBG-based temperature sensor with fast algorithm technique",* Sensors and Actuators A 150 (2009)-198

[14] C. Fabry, A. Perot, "*Theorie et applications d'une nouvelle methode de spectroscopie interferentielle*", Ann. Chim. Phys. 16, 115 (1899).

[15] C. R. Giles, "*Light-wave Applications of fiber Bragg Gratings"*, Journal of Light. Tech., 15, 1391-1404, 1997, pp. 1391-1404

[16] C. BreckHitz, James Ewing and Jeff Hecht, "Introduction to laser technology", December 31, 2003, ISBN-10: 0471667420, 3rd edition, online www.amazon.com

[17] D. K. W. Lam and B. K. Garside, "*Characterization of single mode optical fibre filters*", Applied Optics, 20, 440-5, 1981

[18] D. Kersey, M. A. Davis, and D. Bellemore. Development of fiber sensors for structural monitoring. Proceedings of SPIE, 2456:262–268, 1995. 11

[19] D. W. Kim, Y. Zhang, K. L. Cooper, A. Wang; "*In-fiber reflection mode interferometer based on a long-period grating for external refractive-index measurement*"; *Appl. Opt.* 2005, *44*, 5368-5373.

[20] D. Kersey, M. A. Davis, and D. Bellemore. Development of fiber sensors for structural monitoring. Proceedings of SPIE, 2456:262–268, 1995. 11

[21] E. Delevaque, t. Georges, M. Momerie, P. Lamouler and J. F. Bayyon, "*Modeling of pair-indiced quenchingin erbium doped silicate fibre*", IEEE photonic Technology Letter, 1993, 5(1): 73-75

[22] F. K. Coradin, G. R. C. Possetti, R. C. Kamikawachi, and M. Muller, J. L. Fabris, "Etched fiber Bragg gratings sensors for water-ethanol mixtures: A comparative study", J. Microw. Optoelectron. Electromagn. Appl. 2010; 9:131–143

[23] F. L. Pedrotti, L. M. Pedrotti, L. S. Pedrotti, "*Introduction to Optics*", Pearson International: Upper Saddle River, NJ, USA, 2007

[24] F. Shen, W. Peng, A. Wang, K. L. Cooper, G. R. Pickrell, "*UV-Induced Intrinsic Fabry-Perot Interferometric Fiber Sensors*," Proc. SPIE, Vol. 5590, pp. 47-56, 2004

[25] F. Shen, "*UV-Induced Intrinsic Fabry-Perot Interferometric Fibre Sensors and Their Multiplexing for Quasi-Distributed Temperature and Strain Sensing*", Dissertation

submitted to the Faculty of the Virginia Polytechnic Institute and State University in partial fulfillment of the requirements for the degree of Doctor of Philosophy in Electrical Engineering, copyrights, 1 june 2006.

[26] G. Meltz, W. W. Morey and W. H. Glen, *"Formation of Bragg gratings in optical fibers by a transverse holographic method"*, Opt. Lett., 14, 823-825, 1989

[27] G. W. Yoffe, P. A. Krug, f. Ouellette and D. A. Thorncraft, 'Passive temperature-compensating package of optical fiber gratings', Applied Optics 34, 6859-6861, 1995.

[28] G. Bolognini, J. Park, A. Chiuchiarelli, N. Park, and F. Di Pasquale, "Improved Performance in Raman-based Distributed Temperature Sensing with coded OTDR and Discrete Raman Amplification", © 2005 Optical Society of America, OCIS codes: 060.2370, 290.5860

[29] H. Bourdoucen and A. A Lawati, "Effect of Dispersion Compensation on FBG Sensing System Performance", ISSN 0020-4412, Instrument and Experimental Techniques, 2006, Vol 49, No. 3, pp 115-118

[30] H. Y. Choi, K. S. Park, S. J. Park, U. S. Pack and B. H. Lee, "*Fabry-Perot type high temperature fibre sensor implemented by cascading two fibre cavities*", 2008 OSA/AOE2008

[31] Hernandez, "*Fabry-Perot Interferometers*", Cambridge: Cambridge University Press, 1986

[32] H. Hartog. A distributed temperature sensor based on liquid-core optical fibers. Journal of Lightwave Technology, 1(3):498–509, 1983. 11

[33] H. Y. Fu, H.Y. Tam, L.Y. Shao, X. Dong, P. K. A. Wai, C. Lu, s. K. Khijwania, "*Pressure sensor realized with polarization-maintaining photonic crystal fiber-based Sagnac interferometer*", *Appl. Opt.* 2008, *47*, 2835-2839

[34] H. Y. Choi, K. S. Park, Y. H. Kim, and B. H. Lee, "*Dual-cavity fiber Fabry-Perot interferometric sensor*", 978-1-4244-4103-7/09/$25.0 © 2009 IEEE

[35] H. Hartog. A distributed temperature sensor based on liquid-core optical fibers. Journal of Lightwave Technology, 1(3):498–509, 1983. 11

[36] H. S. Ohn and R. M. Measures, "*A novel Bragg grating distributed-strain sensor based on phase measurements*", Proc, SPIE Smart Sensing. Processing and instrumentation, 1995, SPIE 2444, 158.

[37] J. Ran, Y. Rao, J. Zhang, Z. Liu, B. A. Xu, "*A miniature fiber-optic refractive-index sensor based on laser-machined Fabry-Perot interferometer tip*", J. Lightw. Techol. 2009, *27*, 5426-5429.

[38] J. R. Zhao, X. G. Huang, W. X. He, J. H. Chen, "*High-resolution and temperature-insensitive fiber optic refractive index sensor based on fresnel reflection modulated by Fabry-Perot interference", J. Lightw. Techol.* 2010, *28*, 2799-2803

[39] J. S. Sirkis, D. D. Brennan, M. A. Putman, T. A. Berkoff, A. D. Kersey, E. J. Friebele, "*In-line fiber etalon for strain measurement*", *Opt. Lett.* 1973, *18*, 1973-1975

[40] J. L. Wagener, P. F. Wysocki, M. J. F. Digonnet, H. J. Shaw and D. J. Digiovanni, "*Effects of concentration and cluster in erbium doped fiber laser*", Optics letters, 1993, 18(23): 2014-2016

[41] J. Nilsson, P. Scheer and B. Jaskorzynska, "*Modeling and optimization of short YB sensitized Er-doped fibre amplifiers*", IEEE Photonic Technology letters, 1994, 6(3): 383-385

[42] J. P. Dakin, D. J. Pratt, "Distributed optical fibre Raman temperature sensor using a semiconductor light source and detector", *Electron. Lett.* 1985, *21*, 569–570.

[43] J. K. Barnoski, S. M. Jensen, "Fibre waveguides: A novel technique for investigation attenuation characteristics", Appl. Opt., vol. 15, pp. 2112 - 2115, 1976

[44] J. P. Dakin, D. J. Pratt, "Distributed optical fibre Raman temperature sensor using a semiconductor light source and detector", *Electron. Lett.* 1985, *21*, 569–570.

[45] J. K. Barnoski, S. M. Jensen, "Fibre waveguides: A novel technique for investigation attenuation characteristics", Appl. Opt., vol. 15, pp. 2112 - 2115, 1976

[46] L. Bilro, N. Alberto, and R. Nogueira, "Optical Sensors Based on Plastic Fibers", Sensors (Basel)-2012; 12 (9): 12184-12207

[47] K. S. C. Kuang, S. T. Quek, C. G. Koh, W. J. Cantwell, and P. J. Scully, "Plastic Optical Fibre Sensors for Structural Health Monitoring", Volume 2009, Article ID 312053, 13 pages, doi:10.1155/2009/312053

[48] K. Fidanboylu, and H. S. Efendioglu,*" Fiber Optic Sensors and their Applications",* 5th International Advanced Technologies Symposium (IATS'09), May 13-15, 2009, Karabuk, Turkey

[49] K. T. V. Grattan and B. T. Meggitt, "*Optical Fiber Sensor Technology; Chapman & Hall*", Orange, CA, 1995. USA, 1995.

[50] L. Yuan, J. Yang, Z. A. Liu; "*Compact fiber-optic flow velocity sensor based on a twin-core fibre Michelson interferometer"*; *IEEE Sens. J.* 2008, *8*, 1114-1117

[51] L. Hoffmann, M. S. Müller, S. Krämer, M. Giebel, G. Schwotzer and T. Wieduwilt, "*Applications of fibre optic temperature Measurement"*,Proc. Estonian Acad. Sci. Eng., 2007, 13, 4, 363–378

[52] L. Savage, "Sensing Trouble Fiber-Optics in Civil", Optics & Photonics News March 2013, 1047-6938/13/03/26/8-$15.00 ©OSA

[53] M. E. Bosch, A. J. R. Sánchez, F. S. Rojas and C. B. Ojeda, "Recent Development in Optical Fiber Biosensors", *Sensors* 2007, *7*, 797-859, ISSN 1424-8220

[54] M. A. Ismail, N. Tamchek, M. R. A. Hassan, K. D. Dambul, J. Selvaraj, N. A. Rahim, S. R. Sandoghchi and F. R. M. Adikan, "A Fiber Bragg Grating Bimetal Temperature Sensor for Solar Panel Inverters", *Sensors* 2011, *11*, 8665-8673; doi:10.3390/s110908665, ISSN 1424-8220

[55] M. A. Soto, T. Nannipieri, A. Signorini, G. Bolognini, F. Di Pasquale, A. Lazzeri, F. Baronti, and R. Roncella, "Advanced Cyclic Coding Technique for Long-Range Raman DTS Systems with Meter-Scale Spatial Resolution over Standard SMF", 978-1-4244-9289-3/11/$26.00 ©2011 IEEE

[56] M. K. Barnoski and M Jensen, fiber waveguide: A novel technique of investigating attenuation characteristics, Appl Opt. Vol. 15, pp 2112-2115, 1976

[57] M. G. Xu, J. L. Archambault, L. Reekie and J. P. Dakin, 'Discrimination between strain and temperature effects using dual-wavelength fibre grating sensors', Elect. Lett, 30, 1085-1087, 1994.

[58] M. G. Xu, H. Geiger, J. L. Archambault, L. Reekie, and J. P. Dakin. Novel interrogating system for fibre Bragg grating sensors using an acousto-optic tunable filter. Electronics Letters, 29(17):1510–1511, 1993. 11

[59] M. A. Davis and A. D. Kersey. Matched-filter interrogation technique for fibre Bragg grating arrays. Electronics Letters, 31(10):822–823, 1995. 11

[60] M. G. Shlyagin, S. V. Miridonov, D. Tentori and J. Castillo, "*Twin-grating based interferometric fibre sensor*", 1997 OSA Technical Digest Series, Vol. 16, Washington

[61] M. Mahmoud, "*Modeling of all optical control systems based on fiber Bragg gratings technology"*, Proceedings of the American Control Conference. Denver, Colorado June 4-6, pp. 3353-3357, 2003

[62] M. G. Xu, "*Optical in-fibre grating high pressure sensor".* Electron. Lett., 1993. 29:p. 398.

[63] M. J. Marrone, A. D. Kersey, and A. Dandridge, "*Fiber optic Michelson array with passive elimination of polarization fading and source feed-back isolation*", in Proc. IEEE Optic Fiber Sensors, 8th, Monterey, CA, pp. 69-72, 1992

[64] M. L. Dennis, M. A. Putnam, J. U. Kang, T. E. Tsai, 1. N. Duling, E. J. Frieble, "*Grating sensor array demodulation by use of a passiveiy mode-locked fiber laser*," Opt. Lett., 22, 1362-1364, 1997.

[65] M. G. Shlyagin, S. V. Miridonov, I. M. Borbon and V. V. Spirin, "*Multiplexed twin-Bragg grating interferometric sensor*", 0-7803-7289-1/02/$17.00C2002 IEEE

[66] M. G. Shlyagin, S. V. Miridonov, D. Tentori and J. Castillo, "*Twin-grating based interferometric fibre sensor*", 1997 OSA Technical Digest Series, Vol. 16, Washington

[67] M. A. Davis, D. G. Bellemore, T. A. Berkoff, and A. D. Kersey. Design amd performance of a fiber Bragg grating distributed strain sensor system. Proceedings of SPIE, 2446:227–235, 1995. 11

[68] M. G. Xu, H. Geiger, J. L. Archambault, L. Reekie, and J. P. Dakin. Novel interrogating system for fibre Bragg grating sensors using an acousto-optic tunable filter. Electronics Letters, 29(17):1510–1511, 1993. 11

[69] M. A. Davis and A. D. Kersey. Matched-filter interrogation technique for fibre Bragg grating arrays. Electronics Letters, 31(10):822–823, 1995. 11

[70] M. G. Shlyagin, P. L. Swart, S. V. Miridonov, A. A. Chtcherbakov, I. M. Borbon, "*Static strain measurement with sub-micro-strain resolution and large dynamic range using a twin-Bragg grating Fabry-Perot sensor*", Opt. Eng. 41(8), 1809-1814 (August 2002), 0091-3286/2002/$15.00

[71] R. M. Measures, "*Fiber Optic Strain Sensing*" in Fiber Optic Smart Structures, Eric Udd ed., New York, N.Y., John Wiley & Sons, hc., 1995.

[72] P. S. Reddy, R. L. N. Sai Prasad, D. Sen Gupta, M. Sai Shankar, K. Srimannarayana, and P. Ravinder Reddy, "*Quasi-Distributed Fibre Bragg Grating Array Sensor for Furnace Applications*", Photonic Sensors,DOI: 10.1007/s13320-012-0046-7 (2012)

[73] P. Q. Bao and L. H. Son, "*Gain and Noise in Erbium Doped Fibre Amplifier-a rate equation approach*", communication in physics, Vol. 14, No. 1, 2004.

[74] P. Morris, A. Hurrell, A. Shaw, E. Zhang, P. Beard, "*A Fabry-Perot fibre-optic ultrasonic hydrophone for the simultaneous measurement of temperature and acoustic pressure*", J. Acoust. Soc. Am. 2009, 125, 3611-3622

[75] P. Prerana, R. K.Varshney, B. P. Pal, B. Nagaraju, "*High sensitivity fibre optic temperature sensor based on a side-polished single-mode fibre coupled to a tapered multimode overlay waveguide"*, J. Opt. Soc. Korea 2010, 14, 337-341

[76] P. D. Allen and N. J. Hargrave, "Optical Fibre Temperature Sensor Technology and Potential Application in Absorbed Dose Calorimetry", ISBN 0157-1400 September 1992.

[77] Q. Yu, Y. Zhang, Y. Dong, Y. P. Li, C. Wang and H. Chen, "*Study on Optical Fibre Bragg Grating Temperature Sensors for Human Body Temperature Monitoring*", 978-1-4577-0911-1/12/$31.00 ©2012 IEEE

[78] Q. Wang, Y. Zhao, Y. Zhang, Y. Zhang, B. Han, L. Bai and W. Hou, "Study on characteristics of EFPI pressure sensors for HT/HP oil-well", Optoelectronics and Advanced materials-Rapid communications Vol. 5, No. 9, September 2011, p. 1021 – 1025

[79] R. Paschotta, "*Encyclopedia of Laser Physics and Technology*", ISBN: 978-3-527-40828-3 vol: A-Z 2008

[80] S. V. Miridonov, M. G. Shlyagin and D. Tentori, "*Twin-grating optic fibre sensor demodulation*", Optics comm. 191 (2001) 253-262

[81] S. T. Vohra, *"Handbook of optical fiber sensing technology - optical fiber grating applications*", pp 475-504, 2002

[82] S. C. Kaddu, D. J. Booth, D. D. Garchev, S. F. Collins, *Intrinsic fibre Fabry-Perot sensors based on co-located Bragg gratings.* Optics Communications, 1997, **142**: p. 189-192

[83] S. A. Slattery and D. N. Nikogosyan, "Fiber Bragg grating inscription by high-intensity femtosecond UV laser light: comparison with other existing methods of fabrication", J. Opt. Soc. Am. B/Vol. 22, No. 2/February 2005

[84] S. Kurtaran · M. S. Kılıçkaya, "The modelling of Fiber Bragg Grating", Opt Quant Electron (2007) 39:643–650 DOI 10.1007/s11082-007-9117-1

[85] T. Wang, "*Single frequency fibre laser*", Fiber lasers: Research and technology and applications, 2009 p 113-144

[86] T. K. Gangopadhyay, "*Prospects for Fibre Bragg Gratings and Fabry-Perot Interferometers in fibre-optic vibration sensing*", Sensors and Actuators A 113 (2004) 20–38

[87] T. Wei, Y. Han, H. L. Tsai, H. Xiao, "*Miniaturized fibre inline Fabry-Perot interferometer fabricated with a femtosecond laser*", *Opt. Lett.* 2008, *33*, 536-538

[88] T. A. Berkoff, M. A. Davis, D. G. Bellemore, and A. D. Kersey, "*Hybrid time and wavelength division multiplexed fiber Bragg grating sensor array,*" froc. SPIE, 2444, pp. 288-294, 1995.

[89] V. R. Machavaram, R. A. Badcock, G. F. Fernando, "*Fabrication of intrinsic fibre Fabry-Perot sensors in silica fibre using hydrofluoric acid etching*", Sen. Actuat. *A* 2007, *138*, 248-260

[90] W. W. Morey, "*Distributed fiber grating sensors*", in: Proceedings of the 7th International Conference on Optical Fibre Sensors, IREE, Sydney, Australia, 1990, pp. 285–288.

[91] W. Hu Tsai and C.J. Lin, "*A novel structure for the intrinsic Fabry-Perot fibre temperature sensor*", Journal of light-wave, Vol: 19, No:5 May 2001

[92] Wu, Dong-Fang; Zhang, Tian-Zhao; Jia, Bo "Modified Sagnac interferometer for distributed disturbance detection", Microwave and Optical Technology Letters, Volume 50, Issue 6, 2008, Page(s): 1608 – 1610

[93] W. Li, Y. W. Li, X. D. Han and G. Q. Yu, "The study of enhancing temperature sensitivity for FBG temperature sensor", 978-1-4244-3703-0/09/$25.00 ©2009 IEEE

[94] W. G. Chen, J. Liu, Y. Y. Wang, L. M. Liang, J. B. Zhao and Y. F. Yue, "The Measuring Method for Internal Temperature of Power Transformer Based on FBG Sensors", 978-1-4244-2810-6/08/$25.00©2008 IEEE

[95] X. M. Zhang, Y. Liu, H. Bae, C. Pang and M. Yu, "Phase modulation with micro-machined resonant mirrors for low-coherence fiber-tip pressure sensors", @ 2009 OSA, Vol. 17, No. 26 / Optics Express 23965

[96] X. Wan, H. F. Taylor, "*Intrinsic fibre Fabry-Perot temperature sensor with fibre Bragg grating mirrors*", Opt. Lett. 2002, 27, 1388-1390

[97] X. Bao, D. J. Webb, and D. A. Jackson. 22-km distributed temperature sensor using Brillouin gain in an optical fiber. Optics Letters, 18(7):552–554, 1993. 11

[98] Y. J. Rao, "*In-fibre Bragg grating sensors*", Meas. Sci. Tech., 8, 355-375, 1997

[99] Y. Zhao and Y. B. Liao, "*Discrimination methods and demodulation techniques for fibre Bragg grating sensors*", Optics and Lasers in Engineering, vol. 41, no. 1, pp. 1–18, 2004

[100] Y. J. Rao, M. R. Cooper, D. A. Jackson, C. N. Pannell and L. Reekie, 'Simultaneous measurement of displacement and temperature using in fibre Bragg grating base extrinsic Fizeau sensor', Elect. Lett., 36, 1610-1611, 2000

[101] Y. H. Kim, M. J. Kim, B. S. Rho, M. S. Park, J. H. Jang, B. H. Lee, "*Ultra-sensitive fibre-optic hydrogen sensor based on high order cladding mode*". IEEE Sens. J. 2011, 11, 1423-1426.

[102] Z. Wang, F. Shen, L. Song, X. Wang, A. Wang, "*Multiplexed fiber Fabry-Pérot interferometer sensors based on ultra-short Bragg gratings*", IEEE Photon. Technol. Lett. 2007, 19, 622-624